

Journal of Mechanics of Materials and Structures

Special issue on
**Structural Analysis
of Real Historic Buildings** (part 1)

Volume 13, No. 5

December 2018



JOURNAL OF MECHANICS OF MATERIALS AND STRUCTURES

msp.org/jomms

Founded by Charles R. Steele and Marie-Louise Steele

EDITORIAL BOARD

ADAIR R. AGUIAR	University of São Paulo at São Carlos, Brazil
KATIA BERTOLDI	Harvard University, USA
DAVIDE BIGONI	University of Trento, Italy
MAENGHYO CHO	Seoul National University, Korea
HUILING DUAN	Beijing University
YIBIN FU	Keele University, UK
IWONA JASLUK	University of Illinois at Urbana-Champaign, USA
DENNIS KOCHMANN	ETH Zurich
MITSUTOSHI KURODA	Yamagata University, Japan
CHEE W. LIM	City University of Hong Kong
ZISHUN LIU	Xi'an Jiaotong University, China
THOMAS J. PENCE	Michigan State University, USA
GIANNI ROYER-CARFAGNI	Università degli studi di Parma, Italy
DAVID STEIGMANN	University of California at Berkeley, USA
PAUL STEINMANN	Friedrich-Alexander-Universität Erlangen-Nürnberg, Germany
KENJIRO TERADA	Tohoku University, Japan

ADVISORY BOARD

J. P. CARTER	University of Sydney, Australia
D. H. HODGES	Georgia Institute of Technology, USA
J. HUTCHINSON	Harvard University, USA
D. PAMPLONA	Universidade Católica do Rio de Janeiro, Brazil
M. B. RUBIN	Technion, Haifa, Israel

PRODUCTION production@msp.org

SILVIO LEVY Scientific Editor

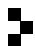
Cover photo: Wikimedia Commons

See msp.org/jomms for submission guidelines.

JoMMS (ISSN 1559-3959) at Mathematical Sciences Publishers, 798 Evans Hall #6840, c/o University of California, Berkeley, CA 94720-3840, is published in 10 issues a year. The subscription price for 2018 is US \$615/year for the electronic version, and \$775/year (+\$60, if shipping outside the US) for print and electronic. Subscriptions, requests for back issues, and changes of address should be sent to MSP.

JoMMS peer-review and production is managed by EditFLOW® from Mathematical Sciences Publishers.

PUBLISHED BY

 **mathematical sciences publishers**
nonprofit scientific publishing

<http://msp.org/>

© 2018 Mathematical Sciences Publishers

PREFACE

MAURIZIO ANGELILLO AND SANTIAGO HUERTA FERNÁNDEZ

The theory of arches and masonry vaults originated at the end of the seventeenth century: Robert Hooke had the brilliant intuition to analyse arches as inverted hanging chains and this allowed the analysis to be incorporated within the science of statics. In France, La Hire published at the beginning of the eighteenth century the first article on the collapse of arches, intending to calculate their thrust. Both the equilibrium and collapse approaches were developed further during the eighteenth century. Since the beginning of the nineteenth century, large masonry bridges have been calculated almost routinely using either of the two approaches. In the middle of that century, the diffusion of the concept of lines of thrust was a crucial step in advancing the analysis of arches and masonry vaults, as it allowed one to understand both collapse and equilibrium.

However, this coincided with a pronounced decline in the interest in the theory of masonry construction. The second half of the nineteenth century concentrated on the development of elastic theory, which is more suited to wrought iron and steel structures. The notion took hold that masonry arches, too, should be calculated as an elastic continuum, contradicting both common sense (masonry is essentially discrete at the macroscale) and the observed collapse of arches. This was a huge step backwards in the understanding of arches and vaults; however, from a practical point of view, engineers and architects continued to use equilibrium graphical methods.

By 1900 the theory of masonry structures had stagnated and articles on masonry structures practically disappeared from specialized journals. The so-called Modern Architecture of Bauhaus dramatically broke with the millenary tradition of vaulted construction: arches and vaults were considered old-fashioned and largely disappeared from architecture (though they were still being built; traditions do not die suddenly). Towards the 1930s the increase in the weight of road vehicles made it necessary to reconsider the safety of many old masonry bridges. Nineteenth-century tests on voussoir arches were repeated and it was noted that the appearance of cracks substantially modified the results of elastic analysis. In the 1960s photoelastic methods and, above all, the appearance of computers, which could handle linear elastic equations easily, revived interest in the use of elastic models of masonry structures, ignoring the evidence of century-old voussoir arch tests and the cracked state of actual masonry structures.

It was within this confusing framework that the figure of Professor Jacques Heyman of Cambridge emerged, almost miraculously. Having contributed decisively to the final development of the plastic calculation of steel frames within Baker's Cambridge team, he realised that the whole field of masonry structures could be included within the wider field of limit analysis if the material met certain conditions: high compressive strength, no tensile strength and a construction which precludes sliding. Precisely these conditions were the hypotheses used in the calculation of masonry arches throughout the nineteenth century. In his paper "The stone skeleton", published in 1966, Professor Heyman took this crucial step,

Publisher's note: For scheduling reasons this special issue on Structural Analysis of Real Historic Buildings is presented in two parts, appearing as issues 13:5 (2018) and 14:5 (2019). This is the first of the two.

rigorously explaining the theory and applying it to the Gothic structure. In the following five decades he has continued to improve the understanding of masonry construction, combining popularization with specialized articles on the most important structural types such as bridge arches, cross and fan vaults, domes, towers and spires, rose windows, and stairs, not only explaining their structural behaviour, but also giving, for the first time, a rational interpretation of their cracks and movements, inherent in this type of constructions.

It would be difficult to imagine the current field of masonry structures without Professor Heyman's seminal contributions. It was he who first realized that the main corollary of the Safe Theorem is the equilibrium approach. Indeed, far from having to make adventurous hypotheses about boundary conditions (essentially ephemeral), Professor Heyman has shown that masonry buildings can be analysed simply by looking for that equilibrium solution, among the infinitely many possible, that respects the compressive nature of the material — its yield condition.

Thus, after 100 years it turns out that the so-called old theory of vaults, used throughout the nineteenth century, was proved to be valid within the more general framework of modern limit analysis. This explains why the calculations made by nineteenth-century engineers on large masonry bridges were essentially correct. So too were equilibrium analyses on masonry vaulted buildings carried out by some architects and engineers in the late nineteenth and early twentieth centuries (Planat, Wittmann, Mohrmann). Finally, Gaudí's genius led him to use the equilibrium approach to generate his complex structures using funicular models.

The work by Professor Heyman over the last fifty years allows us not only to analyse masonry structures, but also to understand the complete framework of the evolution of these constructions that go back more than 6000 years in the Near East. Certainly, as he pointed out, limit analysis leads to geometric statements: the safety of a masonry structure depends essentially on its shape, regardless of size. The old structural rules that have come down to us are indeed geometric, and collect and synthesize the critical experience of the great master builders.

We want this issue of the *Journal of Mechanics of Materials and Structures* to stand in recognition and tribute to the work of Professor Jacques Heyman, which has helped and continues to help us understand masonry structures, illuminating this wide structural field that forms the core of our monumental heritage.

MAURIZIO ANGELILLO: mangelillo@unisa.it

Dipartimento di Ingegneria Civile, Università degli Studi di Salerno, Fisciano, Italy

SANTIAGO HUERTA FERNÁNDEZ: santiago.huerta@upm.es

Escuela Técnica Superior de Arquitectura de Madrid (ETSAM), and Instituto Juan de Herrera, Madrid, Spain

THE STRUCTURAL ENGINEER'S VIEW OF ANCIENT BUILDINGS

JACQUES HEYMAN

Engineers, called on to advise on the repair of an old building — a cathedral, say — will usually have learned their skills in the design of modern buildings using modern materials — steel and reinforced concrete. Care must be taken in transferring those skills to ancient structures. In particular, the engineer is used to provide precise answers (for example, values of stresses) in order to satisfy criteria imposed by accepted practice.

Such an engineer will not have had occasion to consider the fact that a precise description cannot be given for the behaviour of any structure, modern or ancient. The states of all structures are critically dependent on unknown, and unknowable, defects in construction, and, above all, on unknowable movements of the environment. The footing of a column in a steel skyscraper, and the foundation of a pier carrying a tower in a cathedral, will in reality not be in the precise locations assumed by the engineer, and even small “defects” of this sort can have a very large influence on the structural state of the buildings being analysed.

Although unequivocal and unique answers cannot be given to questions that arise in the analysis and repair of old buildings, it is at least possible to calculate states of equilibrium with which a structure is “comfortable”. Although such states will not be observed in practice, their existence satisfies one of the basic theorems of plastic theory — if any one such state can be found, then this gives assurance that the structure is in fact safe. Further, it may be possible to calculate minimum and maximum values for important structural quantities.

1. The engineer and the surveyor

In England, national legislation requires every cathedral to appoint an architect, whose duties include the preparation of a report, every five years, on the state of the fabric of the church. Such architects are often called surveyors — the first surveyor of Westminster Abbey was Christopher Wren. Similarly, the 16,000 English parish churches each have an architect who performs similar duties. Such men and women (there have so far been four women surveyors for English cathedrals, and the architect for Cologne was best addressed as *Dombaumeisterin*) normally have immense experience of such buildings, and they are fully competent to devise remedial and repair work. Occasionally, however, they feel a need for technical advice from an engineer. Wren, despite being a scientist, a mathematician and an astronomer, had a rather poor grasp of structural mechanics, but he had the good fortune to have as a “partner” Robert Hooke, whose grasp of such matters was profound. A present-day cathedral is required to appoint an archaeologist, but there is no mention of a structural engineer.

The present-day architect will engage in dialogue with a modern structural engineer — one who, unlike Robert Hooke, has been taught in an accredited university, and whose qualifications have been accepted

Keywords: ancient buildings, limit analysis, geometrical factor of safety, masonry equilibrium.

by a professional institution as conferring chartered status. The practical expertise of such an engineer has been gained in the design of structures using modern materials such as steel, reinforced concrete, and aluminium, and also with traditional design in wood. Whatever the material, the route to acceptance of a design lies in the satisfaction of a “Code of Practice”, established by some official body such as the British Standards Institution. These codes have clauses which have a common pattern. Calculations must be made, for example, of the values of stresses, which must not exceed some permissible value defined in the code, a value whose function might be to prevent the yield of a steel member, or to prevent the buckling of a column or the flange of a steel beam. Or again, deflections must not exceed certain specified limits, so that the function of the structure is not in some way impaired.

Traditional university courses equip the engineer with methods of calculation leading to numbers — values of stresses, for example — which will satisfy the clauses of the code. The calculations may sometimes be simple, and may occasionally involve some “advanced” mathematics. In either case it will not occur to the engineer that the calculations may not actually lead to a description of the state of the structure under examination. Similarly, the code does not acknowledge that such a description is not even possible.

A very simple example illustrates the difficulty. A table with four legs has a known weight placed on its top in a known position, and it will be supposed that the problem facing the structural engineer is the design of those four legs. To determine their size, it is evident that the engineer must calculate the forces in the legs. It turns out, technically, that this is a very difficult problem (and this is why the cathedral architect needs engineering advice). In simplistic terms, there are only three equations, and four leg forces must be determined. The matter is straightforward for a tripod; the addition of a fourth leg makes the table structurally redundant (hyperstatic). In order to solve the problem, further equations must be written which are no longer simple — they are indeed hideously complex. Much effort has been devoted, from the middle of the nineteenth century and through the twentieth century, to the solution of these equations, and ingenious and brilliant ways have been devised to obtain exact or remarkably accurate approximate solutions. It is this structural theory which forms the backbone of the university courses taught to the engineer.

The advent of the high speed computer has taken the drudgery out of the solution of the complex equations; apparently unequivocal values can now be obtained easily for the four leg forces. These values are indeed the correct solutions of the equations, but they are not in fact the values of the forces in the legs of the actual table. A nearly rigid table placed on the nearly rigid pavement outside a restaurant on a summer’s night will, annoyingly for the diners and for the structural analyst, rock — one leg will be clear of the ground. If the leg is clear by only a fraction of a millimetre then the force in that leg is known, pace the computer printout — it must be zero. Moreover, it is not known in practice which leg is off the ground: a slight shift of the table will reduce the force in some other leg to zero. A friendly wine waiter will slice a cork diagonally into two wedges; one of these, placed under a leg will make the table more comfortable (anthropomorphically for itself, and also for the diners).

This simple and seemingly abstract example is a paradigm for the structural engineer; how can some meaningful statement be made about the forces in the legs if any one of the four may be clear of the ground, be supported by a rigid floor, or may be resting on a flexible foundation of unknown properties? The reason that the computer has given wrong answers to the problem is that the program has assumed, or rather the analyst using the program has assumed, that all four legs are in contact with a rigid floor. The

modern engineer designing a steel frame has the same problem, although the problem is almost certainly unknown to him; how can a meaningful statement, that is a set of numbers (stresses, deflections and so on), be generated to satisfy the code, if the boundary conditions for the frame are unknown? None of the column footings, for example, will have been constructed exactly at the levels specified in the design, and, in any case, the footings will have suffered settlements of small, but unknown, extents. Even very small discrepancies between the design and the actual construction can lead to large variations in the force distribution in the frame.

It is the same sort of problem that faces the surveyor repairing a cathedral, and who wishes to make some more or less major intervention into the fabric. It may be necessary, for example, to take down and rebuild a flying buttress, in which case some temporary propping will be necessary — what loads will the temporary work have to bear? Or an external main buttress may be surmounted by a massive pinnacle: can this pinnacle be safely removed and then replaced? Or a high vault may need the replacement of several of its masonry components; what is the force distribution in the vault so that assurance can be given that a stone can be taken out and replaced? It is answers to such questions that the surveyor requires from the engineer.

Because the foundations of a cathedral have settled, since completion of construction, by unpredicted amounts, and since the masonry has distorted and cracked, then it is not possible, even if all these defects are surveyed and recorded, to calculate a unique structural state for the cathedral as a whole, or for individual elements such as flying buttresses. But it is of little help to say that exact and unequivocal answers cannot be given to the surveyor's questions. Some sort of answer must be found.

2. Plastic theory

Plastic theory has seemingly changed its objectives since it was formulated in the 1930s and 1940s. It was devised originally for the analysis and design of engineering structures constructed from ductile material, above all steel structures, but is in fact applicable to any “sensible” material (not cast iron or glass, for example). The original objectives are revealed in the early US term for the theory — limit design; the calculations referred to the evaluation of the greatest load a structure could carry. Thus the objective shifted from an examination of the way a structure might stand in comfort, to an examination of the way it might collapse, and different sorts of equations were involved.

Early emphasis was on the estimation of such collapse loads, and the calculations were assisted by the three basic theorems of the new theory. The unsafe theorem states that a calculated collapse load can, in general, never be achieved in practice. The safe theorem states that if a structure can achieve a “comfortable” state of equilibrium under a certain loading, then the structure can never collapse under that loading. The uniqueness theorem states that the largest safe loading is equal to the smallest unsafe loading.

The calculation of collapse loads (for steel frames, for example) is relatively straightforward, at least compared with conventional elastic analysis, and simple plastic designs were, and still are, made in this way, with a full awareness of their “unsafeness”. But the surveyor of a cathedral is not, at least in the first instance, interested in the possible ways a flying buttress might collapse; the interest is in the value of thrust in the buttress with which it is “comfortable”. Emphasis shifts to the use of the safe theorem, and in this context the term “plastic analysis” could well be replaced by the term “equilibrium analysis”.

3. Equilibrium analysis

It is of interest that Coulomb, in the section on masonry arches in his 1773 “Essai”, does not attempt to calculate the “actual” state of such an arch. (Coulomb tackles the four classic structural engineering problems of the eighteenth century — the strength of beams, the strength of columns, the thrust of arches and the thrust of soil. This last topic is commonly regarded as laying the foundations of the science of soil mechanics). The full title of the paper contains the words “the application of the rules of maximum and minimum to some problems in architecture”; Coulomb was among the first to use the century-old calculus to the solution of some problems in civil engineering.

In a very simplified summary of Coulomb’s findings, his fundamental conclusion for the stability of a masonry arch is that the “line of thrust” must lie within the boundaries of the masonry of the arch. This is a purely geometrical statement, with no references to values of stress, although Coulomb is well aware that, exceptionally, crushing may occur. If the line of thrust should touch the surface of the arch, then a “hinge” will form between two voussoirs, and equations of statics will enable the determination of the value of the horizontal thrust which must be exerted by the arch on its abutments. The positions of such hinges are to be determined, and different arrangements of their locations will lead to different values of the abutment thrust; consideration of all possible values will give upper and lower bounds on the thrust. These are the maxima and minima of Coulomb’s title.

Coulomb makes no numerical calculations, nor indeed does he consider arches of any defined shape; the principles he establishes are general. Couplet, some fifty years earlier, does not discuss bounds on the value of thrust; instead, he considers a particular problem, that of a semicircular arch of constant ring thickness subject to its own weight. He shows (with a trivial numerical error) that such an arch must have a certain minimum ring thickness (just over ten percent of its radius), and his calculations are based upon the supposition that hinges form simultaneously in both the extrados and the intrados. He does not anticipate Coulomb’s approach, but, effectively, Couplet establishes the position of a thrust line which gives, simultaneously, Coulomb’s maximum and minimum — that is, his solution gives a unique value of thrust for the semicircular arch of least thickness.

This geometrical idea of smallest dimensions of a masonry structure makes it possible for the engineer to give more helpful answers to the surveyor. For example, a semicircular arch of the type studied by Couplet, but with a ring thickness of twenty percent of the radius (rather than the minimum ten percent), may be said to have a “geometrical factor of safety” of 2, and the engineer may well consider this to be appropriate for a particular masonry element. Equally, the engineer can provide numerical values for the least and greatest values of abutment thrust necessary to maintain stability of the arch.

As an example, a Gothic flying buttress often has a linear upper surface and a curved lower surface, and may be treated as an inclined arch conveying the thrust from the high vault of the church to the main external buttress outside the aisles. Since a straight line which lies completely within the masonry can be drawn from end to end of this flying buttress, and since this implies that the corresponding straight line of thrust could maintain a very large (theoretically infinite) outward force exerted by the high vault, then the strength of the flier would be determined only by the crushing strength of the masonry.

By contrast, should the external buttress move outwards, away from the main body of the church, then the flying buttress will attempt conversion in the usual way to a three-pin arch, by the formation of hinges between the stones of the masonry. Such a three-pin arch is subject to a calculable value of thrust at its

ends, and this is the minimum value of thrust for stability of the flying buttress. The thrust exerted by the high vault must exceed this minimum.

Thus the engineer can in fact give some sort of answer to the surveyor as to the forces within a flying buttress — the buttress will be stable if the thrust from the high vault exceeds a calculable value, and will in fact be able to sustain much higher thrusts if the flier is of a standard Gothic type.

The same sort of calculation can be made for the high vault itself. Since the masonry of such vaults is, relatively speaking, fairly “thin”, and since the compressive forces necessary for stability of the vault must lie within the masonry, the lines of action of such forces, and their values, can be calculated with some certainty. The engineer can now be of more positive help to the surveyor — if a flying buttress has to be taken down and rebuilt, then the temporary propping to the high vault can be designed, also with some certainty.

4. The schooling of a structural engineer

This discussion of the actual behaviour of a structure, whether constructed from masonry, from steel, or from any other suitable material, has, by implication, exposed a severe pedagogic problem. How is the professor of structural engineering to teach a theory, any theory, which purports to describe the state of a structure under given loading, when it is known that that state is critically dependent on factors, notably boundary conditions, which are in practice unknown? Moreover those factors are not only unknown — they are, by their nature, unknowable. They depend, for example, on unknown errors of manufacture and assembly, on the variability of the construction materials, and, above all, on random movements of the environment from which the structure is supported.

The professor must somehow make clear to the students that, no matter how counter-intuitive this may seem, there is no calculable actual state of a structure, since there is in fact no unique such state. However, if it is possible to determine a state which satisfies every requirement of internal and external equilibrium, and with which the structure is comfortable (for example, stresses below specified limits), then this is a demonstration that the structure is safe. Thus although it is not possible to calculate the value of the force actually transmitted by a flying buttress, it is at least possible to determine limits between which that value must lie.

The newly qualified structural engineer, called upon to design a more or less conventional structure in steel or concrete, will be forced to provide calculations leading to numbers which satisfy some prescriptive code. As has been noted, such codes do not conceive the possibility that there is not a calculable actual state of a structure — on the contrary, they imply that calculations (normally by implication elastic calculations) can be made so that various clauses of the code can be shown to be satisfied. Until there is a complete revolution in the way in which such codes are assembled, the professor will fail the students if they are not equipped with a mastery of nineteenth and twentieth century elastic theory of structures. The best the professor can do, having ruined the students' faith in elastic calculations, is to reassure them that such calculations do in fact give numbers describing states with which the structure is comfortable.

References

Some of the background material to this paper may be found in the following publications by the author: “Reinforced concrete and masonry”, pp. 60–87 in *Plastic Design of Frames, II: Applications*, Cambridge University Press, 1971.

Coulomb's memoir on statics: an essay in the history of civil engineering, Imperial College Press, London, 1997.

Il saggio di Coulomb sulla statica, Hevelius Edizioni, Benevento, 1999.

The stone skeleton, Cambridge University Press, 1995.

El esqueleto de piedra, CEHOPU, Juan de Herrera, Madrid, 1999.

Basic structural theory, Cambridge University Press, 2008.

Teoría básica de estructuras, CEHOPU, Juan de Herrera, Madrid, 2011.

Guest editors' note

Jacques Heyman has been one of the main contributors to the development of structural theory in the 20th century. After graduating he joined the distinguished Cambridge Team directed by J. F. Baker that established the basis for plastic analysis of steel frame structures.

He soon took on great responsibilities in the team and in 1949 he obtained his doctoral degree. He then travelled to the United States to work with William Prager. Having spent a postdoctoral year at Brown University, from 1949 to 1950, he returned to that school for his first sabbatical year, from 1958 to 1959. Already early in his career he had acquired a fundamental theoretical base. In 1956 he coauthored with J. F. Baker and M. R. Horne the first book rigorously covering plastic theory for the analysis of steel frames: "The steel skeleton, II: Plastic behaviour and design". The book summarised all the work carried out by the Cambridge team over the previous decade and, for the first time in a book about analysis, the fundamental theorems of limit analysis are stated and applied for design purposes.

Plastic theory was developed for steel structures and, later, it was seen that it could be applied to reinforced concrete structures. Actually, plastic theory can be applied to any kind of structure that exhibits a ductile behaviour and does not have buckling problems. This fact that had been foreseen by some engineers since the beginning of the 20th century, was clearly and rigorously stated by Jacques Heyman. He is the first one to notice that the fundamental theorems meant a new paradigm that could be applied to all structures built with conventional materials. Jacques Heyman realised that the theorems could, also, be translated even for more heterogeneous materials such as stone or brick.

In 1966 he published his celebrated paper "The stone skeleton", which constituted a milestone in the development of the modern theory of masonry structures. This highly original and lucid article explains how plastic theory is adapted to the field of masonry architecture. Following a hint from Prager, he realised that, if certain properties are given to the material masonry, the fundamental theorems can be translated to suit this case of seemingly different structures. In the field of masonry, over 30 other articles and various books have followed his first article of 1966. In these publications he has applied the modern theory to the study of basic structural elements in masonry buildings (vaults, domes, flying buttresses, towers, spires, etc.).

In fact, his interpretations of Gothic theory close the debates about the structural behaviour of gothic vaults and cathedrals, ongoing since the mid-19th century, occupying the minds of academics such as Viollet-le-Duc, Ungewitter, Mohrmann, Abraham, etc. The deep meaning and the practical consequences of Jacques Heyman's discovery has not been yet really understood by many architects and engineers, and the present paper, which opens this special issue of JoMMS on the application of structural analysis to real historic masonry constructions, is addressed precisely to explain why.

For the reader's convenience, we add a selection of papers by Jacques Heyman that can help put the present paper into a larger perspective.

"The stone skeleton", *Int. J. Solids Structures* **2**:2 (1966), 249–279.

"Reinforced concrete and masonry", pp. 60–87 in *Plastic design of frames, II: Applications*, Cambridge University Press, 1971.

"The Gothic structure", *Interdisciplinary Science Reviews* **2**:2 (1977), 151–164.

"The restoration of masonry: structural principles", *Architectural Science Review* **20**:2 (1977), 35–37.

"The estimation of the strength of masonry arches", *Proc. Instn. Civ. Engrs.* **69**:4 (1980), 921–937.

"The high endurance of the masonry structure", pp. 59–65 in *Durability and design life of buildings*, The Institution of Civil Engineers, 1984.

"The maintenance of masonry: papering over the cracks", pp. 190–193 in *Proc. Symp. Building Appraisal: maintenance and preservation* (Bath, England, July 1985), The Institution of Structural Engineers, 1985.

"The structural analysis of Gothic architecture", *Proceedings of the Royal Institution* **59** (1987), 215–226.

"The care of masonry buildings: the engineer's contribution", pp. 3–12 in *Structural repair and maintenance of historical buildings*, edited by C. A. Brebbia, Computational Mechanics Publications, 1989.

"The collapse of stone vaulting", pp. 327–338 in *Structural repair and maintenance of historical buildings III*, edited by C. A. Brebbia and R. J. B. Frewer, Computational Mechanics Publications, 1993.

"Hambly's paradox", *Proc. Instn Civ. Engrs. Civ. Engng* **114**:4 (1996), 161–166.

"Navier's straitjacket", *Architectural Science Review* **42**:2 (1999), 91–96.

"Why ancient cathedrals stand up: the structural design of masonry", *Ingenia* **10** (2001), 19–23.

"Theoretical analysis and real-world design", *The Structural Engineer* **83** (2005), 14–17.

"A peculiar tale", *Construction History Society Newsletter* **72** (2005), 1–8.

"Masonry", pp. 39–48 in *Basic structural theory*, Cambridge University Press, 2008.

"La coupe des pierres", pp. 807–812 in *Proceedings of the Third International Congress on Construction History*, Brandenburg University of Technology, Cottbus, Germany, 2009.

"Mathematics and structural engineering", pp. 3–12 in *Mechanics and architecture: between epistème and téchne*, edited by A. Sinopoli, Edizioni di Storia e Letteratura, Rome, 2010.

"The architect and the engineer", pp. 255–261 in *Geometry and proportion in structural design: essays in Ricardo Aroca's honour*, Lampreave, Madrid, 2010.

"The crossing space and the emergence of the modern professional architect and engineer", *Construction History* **31** (2016), 25–60.

Received 18 Apr 2018. Revised 3 Dec 2018. Accepted 9 Dec 2018.

JACQUES HEYMAN: jh10002@eng.cam.ac.uk

Department of Engineering, University of Cambridge, Cambridge, United Kingdom

MECHANICS OF FLYING BUTTRESSES: THE CASE OF THE CATHEDRAL OF MALLORCA

PAULA FUENTES

The function of the flying buttress is to take the thrust from a central vault and carry it over the lateral aisle to the external buttresses. Flying buttresses also resist lateral loads such as wind and seismic loads. When there is an additional upper tier, its main function is to carry these lateral loads. The structural behavior of flying buttresses has been studied by several authors since the 19th century with different approaches. An accurate survey of the cathedral of Mallorca has been used to study these elements. The flying buttresses in the cathedral of Mallorca, with ca. 9 m span and around 30 tons weight, are probably the biggest in Gothic architecture. Their position approximately 30 m above ground makes them very sensitive to the leaning of the buttresses. First, an overview of the structural behavior of flying buttresses will be provided, within the theoretical framework of limit analysis. Then, the general equilibrium, deformations and crack patterns of the flying buttresses in the cathedral of Mallorca will be analyzed. The local problems, such as the sliding of the head of the flyers, and the different solutions that have been adopted through history will be studied.

1. Structural behavior of flying buttresses

Several authors have studied flying buttresses from the point of view of their structural behavior by employing different approaches. Viollet-le-Duc in his *Dictionnaire* [1854] dedicates an article to this element, making some qualitative notes about its structural behavior.

The first complete static analysis was carried out by Mohrmann for the third edition of Ungewitter [1890], applying graphic analysis to the study of Gothic buildings, including flying buttresses (Figure 1). He differentiated between the function of lower and upper flyers, assigning the upper ones the function of taking the wind load. The contributions of Mohrmann were known in the United Kingdom through the work of Rosenberg [1936]. Fitchen [1955] further discussed the function of the upper flying buttresses.

The most complete study of the structural role of flying buttresses was made by Heyman [1966; 1967], who is also responsible for the application and development of limit analysis theory to masonry structures [Heyman 1995; 2008]. Applying limit analysis theory to a masonry arch, it is possible to say that if we find a thrust line contained inside the arch, the arch will not collapse. As the arch is not a statically determinate structure, it is not possible to know the “actual” thrust line. However, it is possible to establish the boundaries within which the thrust will be. The thrust line with the largest rise and the smallest span that fits inside the arch corresponds to the minimum thrust (Figure 2, left top), while the one with the smallest rise and largest span corresponds to the maximum thrust (Figure 2, left bottom). In these two cases, three hinges will form at the points where the thrust line touches the border of the arch, turning it into a statically determinate structure. Minimum thrust will occur when the abutments spread

Keywords: Flying buttresses, cathedral of Mallorca, limit analysis of masonry structures.

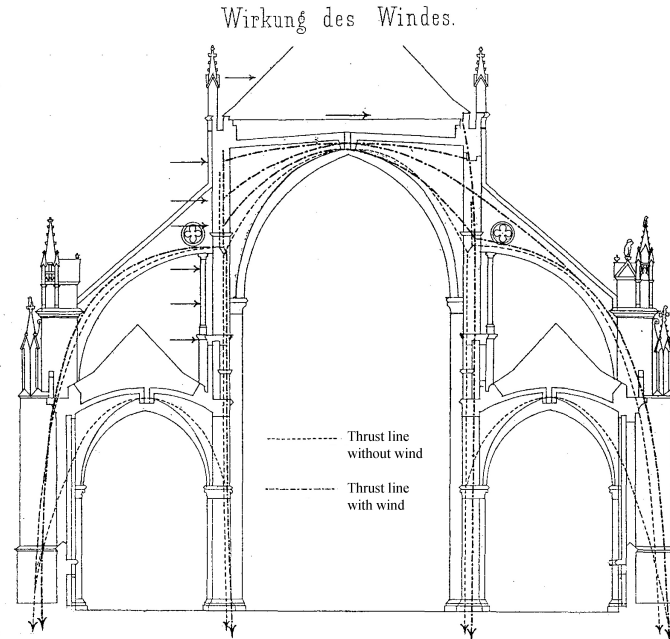


Figure 1. Cross section of the cathedral of Strasbourg showing the thrust line with and without wind [Ungewitter 1890]. Dotted line: thrust line without wind. Dotted-dashed line: thrust line with wind. Note that, with wind, the thrust line goes through the wall over the transverse arches.

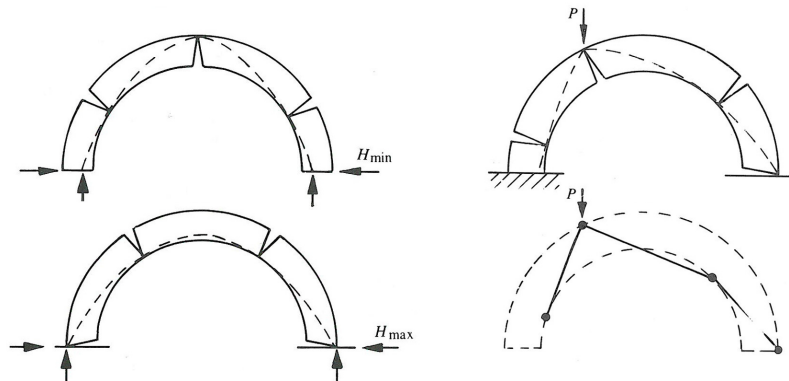


Figure 2. Semicircular arch: line of minimum thrust and line of maximum thrust (left column) and collapse mechanism (right column) [Heyman 1995].

and the arch has to accommodate to the new span with the formation of the three hinges shown in Figure 2 (left top). If a fourth hinge is formed, the structure will turn into a mechanism (Figure 2, right column).

In the case of flying buttresses, the line of minimum thrust is shown in Figure 3 (left) for the long flyer of Nôtre-Dame, Paris. The mechanism of three hinges formed by the spreading of the abutments is shown in Figure 3 (center).

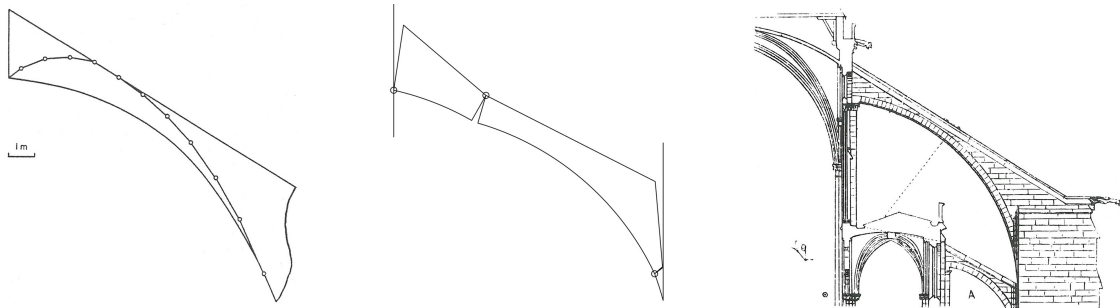


Figure 3. Left: passive line of thrust in the flying buttress of Nôtre-Dame, Paris [Heyman 1966]. Center: flying buttress of Nôtre-Dame with a spreading of the abutments. Right: partial cross-section of Nôtre-Dame [Viollet-le-Duc 1854].

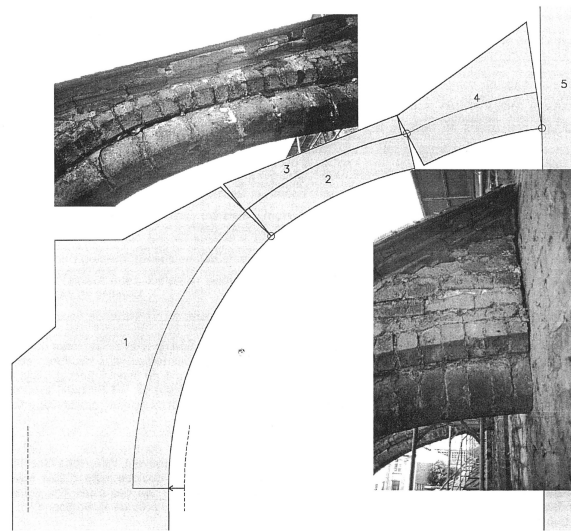


Figure 4. Cracking forming three hinges in a flying buttress at the Dominican church of Louvain [Smars 2000].

Flying buttresses are usually formed of three parts, that is, the arch on the bottom, a vertical wall above the arch, and a coping running along the top of this wall, where a gutter may be present to conduct rainwater (Figures 3 and 4). In some cases, because of the construction of the flyer, these parts may deform separately, as shown in Figure 4 [Smars 2000, pp. 167–169]. The wall between the arch and the coping is sometimes lightened by means of an openwork tracery, resulting in a lower and an upper ribs that can be considered to act independently from a structural behavior point of view. Fitchen noted that, in this case, the upper straight strut does not create inward pressure, stabilizing at the same time the lower arch because of its weight [Fitchen 1961, p. 78]. Ungewitter considered that the upper rib acts as a shore that can take any variable forces from zero to the crushing limit of the material [Ungewitter 1890, pp. 160–161].

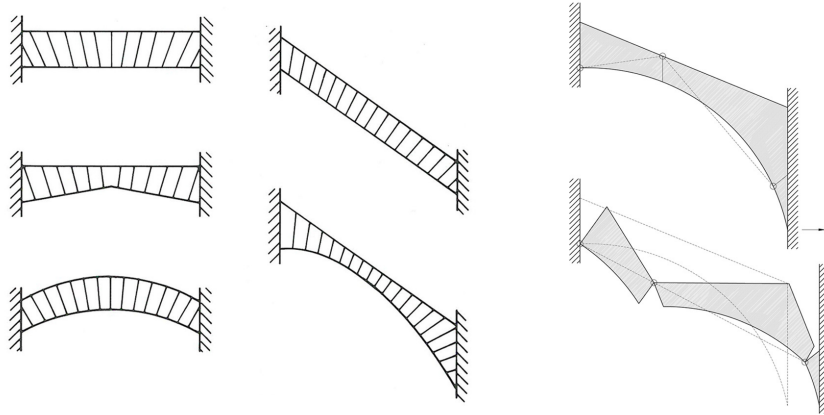


Figure 5. First and second column: arches that cannot collapse by the formation of a four hinge mechanism [Heyman 1995]. Third column: snap-through mechanism for a flying buttress.

As Heyman pointed out, for some arch geometries it is not possible to find a mechanism of collapse. This is the case of flat arches, and most flying buttresses, which are a development on the flat arch (Figure 5, first and second column) [Heyman 1995, p. 20]. Considering infinite compressive strength, these arches will only collapse if the abutments spread enough to form a *snap-through* mechanism that requires very large displacements (Figure 5, third column).

Limit analysis of masonry structures assumes that the sliding between two stones is impossible; however, there is a common problem in flying buttresses regarding the sliding at their head. Considering the line of minimum thrust and depending on the form of the flyer, the thrust may be very inclined in the upper part, and it may be outside the cone of friction (Figure 3, left). In this situation, the first voussoirs may slide along the wall of the main nave. The construction details of the flyer, which is not usually connected to the wall, permits this sliding. The absence of connection between the flying buttress and the wall has been discussed by Viollet-le-Duc [1854, p. 64] and Ungewitter [1890, p. 396]. Both stated that a connection with the wall could cause damages, as the flying arch would not be able to move freely.¹

Master masons were aware of the sliding problem and they took measures to avoid it. The common solution in French Gothic was placing a column or a pilaster under the head of the buttress (Figure 3, right). In the case of Mallorca, as will be seen, master masons used a solution unique in Gothic construction, placing stone bracings under the head to avoid this sliding. It is also possible to avoid the sliding by varying the form of the flyer, as remarked by Heyman [1966, p. 264] in the case of Lichfield cathedral (Figure 6), where the thinness and slope of the flyer causes an almost horizontal thrust at its head.

More recently Nikolinakou et al. [2005] have studied the structural behavior of early French flying buttresses, analyzing the significance of their forms and the possible failure modes. They demonstrated that shorter and less sloped flying buttresses have more tendency to sliding failure [Nikolinakou et al. 2005, pp. 1201–1203, Figure 6a].

¹An example of this sliding can be seen in [Nikolinakou et al. 2005, p. 1202, Figure 7]. The independent construction of the flyer and the wall is visible in the cathedral of Mallorca.

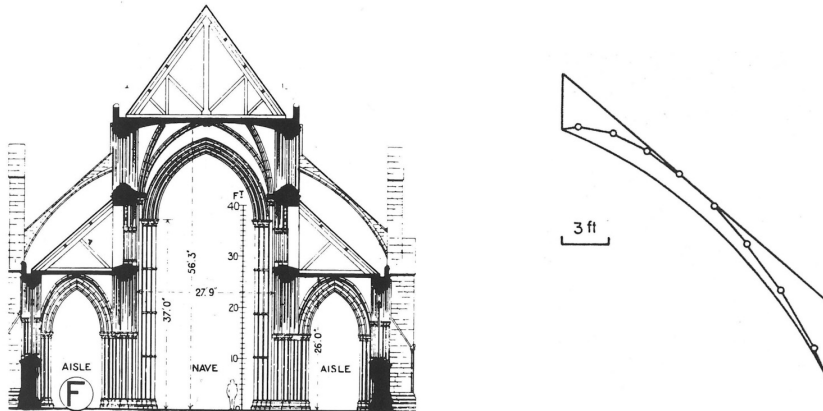


Figure 6. Left: Lichfield cathedral. Right: line of minimum thrust in the flying buttress at Lichfield cathedral; note the almost horizontal thrust at the head [Heyman 1966].

2. The flying buttresses in Mallorca

The construction of the cathedral of Mallorca was begun in the 14th century. The last bay was finished in the 17th century. In the 19th, the west façade was replaced by a neo-Gothic one. Despite the long construction, the original design was kept with only small variations.²

The cathedral has the highest central nave in Spanish Gothic architecture, reaching 44 m. The span, approximately 18 m, is one of the longest and the pillars are some of the most slender found in a Gothic building (Figure 7). The construction of a building with these dimensions was for sure a structural challenge for the master builders.³ Flying buttresses are a fundamental element in the equilibrium of the building and their study is an important topic, since they have a considerable size (around 9 m span), and it is possible to observe deformations, sliding and original solutions responding to these problems.

It is worth discussing the presence of transverse walls over the transverse arches of the nave, connecting the upper flying buttresses found on either side (Figures 7 and 8). As Ungewitter [1890, p. 388] mentioned, the upper flyers do not benefit from the thrust of the vault to counteract their own thrust, and the construction of a transverse wall over the transverse arch between the both sides of the building increases their stability.⁴ Besides some construction differences, the shape of the flying buttresses is mainly the same in all different bays. The survey of the cathedral of Mallorca provided the possibility of studying the actual deformation of the flying buttresses and relate it to the leaning of the buttresses.⁵

²A complete work about the cathedral has been done in Fuentes and Wunderwald [\geq 2018]. The variations on the design regarding the flying buttresses and other elements are explained here.

³The stability of the cathedral has been analyzed with different approaches throughout history. A summary of these studies can be found in Fuentes and Wunderwald [2017].

⁴Besides a possible function to counteract the thrust of the flyers, these walls have a fundamental role in the general stability of the building [Rubió i Bellver 1912, p. 100] and [Huerta Fernández 2017, p. 15].

⁵The survey of the cathedral has been done with the collaboration of the “Raumbezogene Informationssysteme” of the BTU Cottbus-Senftenberg.



Figure 7. Cross-section of the cathedral of Mallorca: through the center of the fifth bay (left) and through the fifth pillars (right) [Fuentes and Guerra 2015].

Based on the survey, the original shape of the flyers has been supposed as shown in Figure 9. This ideal geometry is based on the fourth flying buttress of the north side, where the presence of the tower has prevented large deformations. A radius of 8.8 m fits very well with the survey.

2.1. Static behavior of the flying buttresses in Mallorca. In his structural analysis of the cathedral of Mallorca, Rubió [Rubió i Bellver 1912, pp. 120–121] concluded that the cathedral may have been better without the upper tier of flying buttresses, since these are very large and consequently exert a large thrust.

More recently, Huerta [2017, p. 45] performed a structural analysis of the cathedral of Mallorca and he confirmed that the flying buttresses are well designed and that their deformations are typical in this type of element.

For the present analysis of the flying buttresses, a specific weight of 18 kN/m^3 has been assumed.⁶ The lower flyer has been calculated to have a weight of 408 kN. The passive thrust is 80 kN. The upper flying buttress has a smaller passive thrust of 75 kN and a weight of 330 kN (Figure 10).

The matter of the minimum thrust has been considered, but there is also an upper limit of the thrust that is given by the least inclined line that can fit in the flyer. However, as explained above, thanks to their shape, a straight line can be fitted inside the flyer without touching the edges and it is therefore possible to say that the maximum thrust is infinite, being only limited by the crushing strength of the material. That is, considering a crushing strength of 20 N/mm^2 , a maximum thrust of 29,000 kN would be required for the lower flyers to fail,⁷ while the upper flying buttresses would fail by crushing with a thrust of 18,800 kN. As can be seen, the flying buttresses are far away from their crushing failure.

⁶In the report made by the Universitat Politècnica de Catalunya, various tests were carried out on the stones of the flying buttresses, obtaining different specific weights. An average value has been deduced from these tests [UPC 2006–2008, Documento 3, §1.4].

⁷Some tests have been performed on the stones of the flying buttresses. The results vary considerably, yielding a minimum strength of 42 N/mm^2 and a maximum of 152 N/mm^2 [UPC 2006–2008, Documento 3, §1.4].

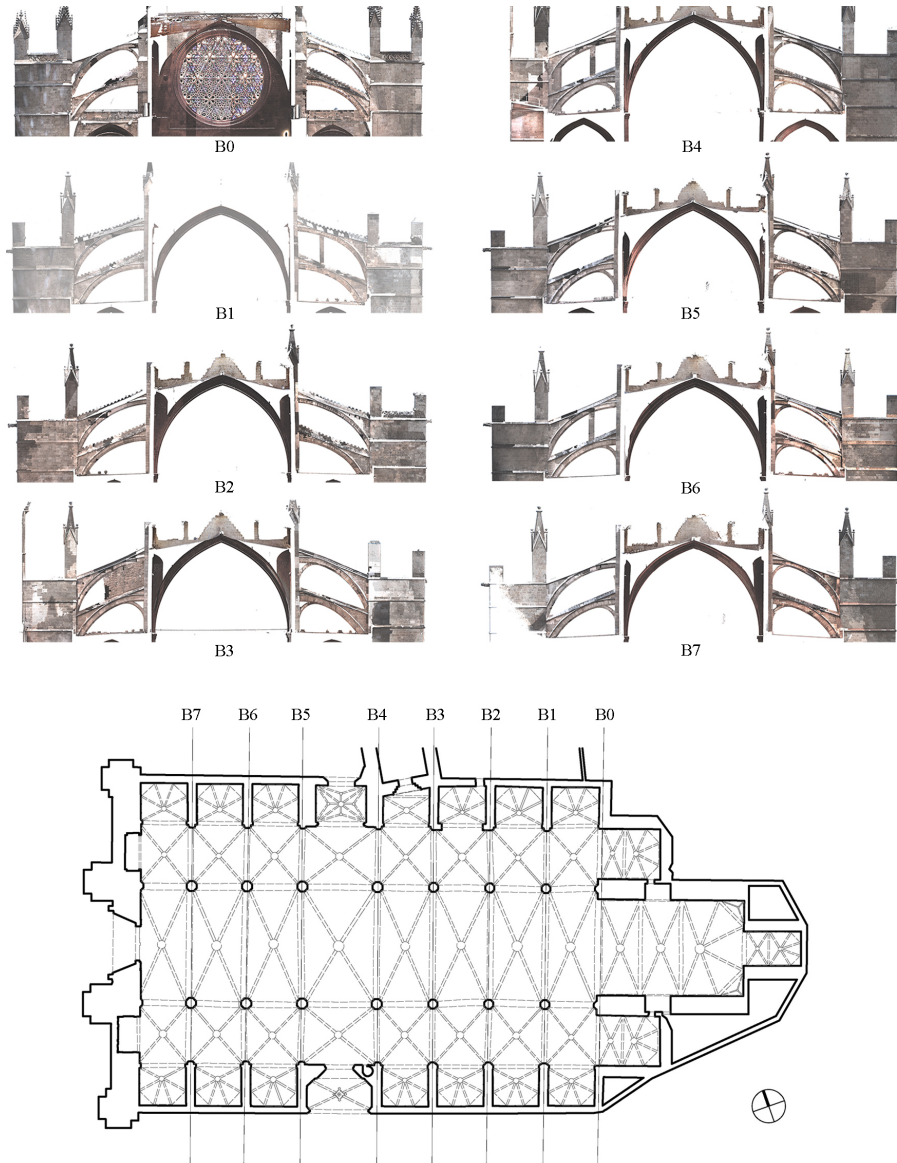


Figure 8. Elevations of all the flying buttresses (with the exception of the ones on the façade) and plan view of the cathedral of Mallorca (based on the cloud of points by Rex Haberland).

2.2. Cracks and distortions. As explained earlier, the line of minimum thrust is the one that occurs when there is spreading of the supports. The existing leaning of the buttresses, published by Fuentes and Guerra [2016], has been used in this study. As shown in Table 1, the leaning is greater in the south side (towards the sea). These movements appear to be quite large. However, they are around 1% of the height of the buttress, which is not a big movement (see Figure 7, where the distortions have been drawn, but are barely noticeable).

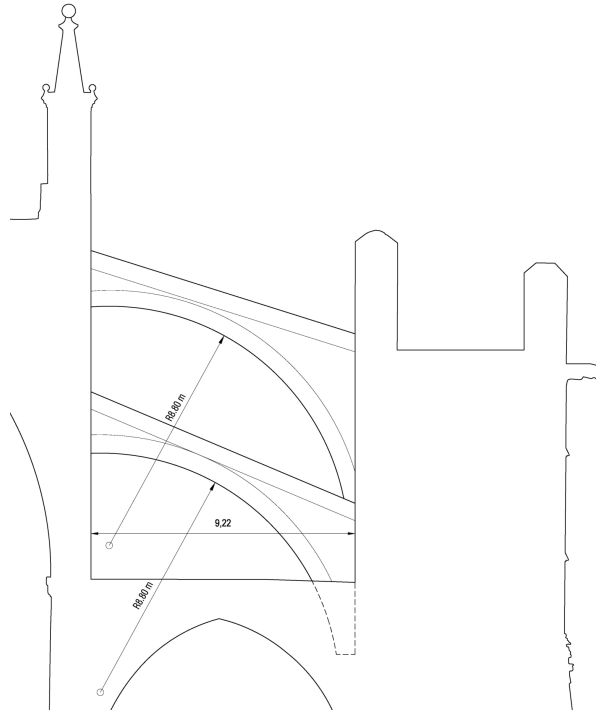


Figure 9. Ideal geometry considered for the structural analysis.

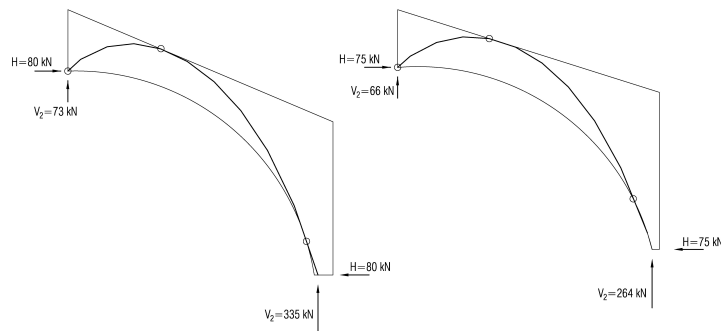


Figure 10. Line of minimum thrust: lower flying buttress (left) and upper flying buttress (right).

The leaning of the buttresses causes a drop in the central part of the flyers, which can be seen most clearly in the upper flyers. There is an additional movement to be considered. The wall of the central nave leans inwards towards the upper part, at the height of the upper flyer, resulting in an additional increase of the span of this flyer.⁸ Figure 11 shows the deformation of the ideal flying buttresses, considering the leaning of the second southern buttress B1 (from Table 1: 26.5 cm in the upper flyers and 20.5 cm in

⁸This leaning inwards of the upper part of the lateral wall of the main nave can be caused because the crack opened due to the increasing of the span of the main vault (wall's crack), can be closed again when the upper flying buttress thrust inwards.

portico height (m)	out of plumb (m)							
	B0		B1		B2		B3	
	N	S	N	S	N	S	N	S
34.7	0.395	0.270	0.470	0.265	0.130	0.330	tower	0.360
27.3	0.310	0.215	0.395	0.205	0.115	0.305	tower	0.305
	B4		B5		B6		B7	
	N	S	N	S	N	S	N	S
	34.7	tower	0.445	0.145	0.400	0.105	0.340	0.205
27.3	tower	0.350	0.085	0.310	0.080	0.245	0.150	0.230

Table 1. Out of plumb of the external buttresses of the different porticos, on the north and south elevations (see plan in Figure 8). The buttresses lean always outwards from the nave, leading to an increased span for the flying buttresses. The table gives the out of plumb at two heights: 27.3 m and 34.7 m above the floor (table made after [Fuentes and Guerra 2016]).

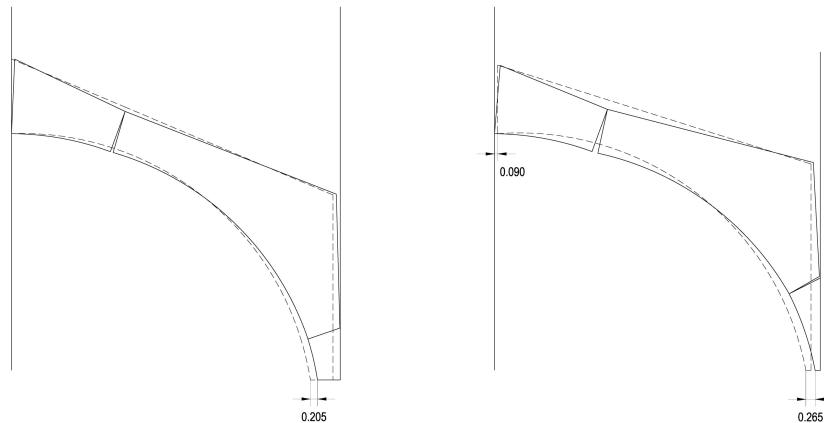


Figure 11. Theoretical deformation of the ideal flying buttress for the leaning of the south buttress B1 and the leaning of the nave wall. Geometry previous the deformation in dashed line: lower flying buttress (left) and upper flying buttress (right).

the lower flyers) and the inwards leaning of the nave wall (9 cm). For these deformations, the maximum drop is 18 cm in the lower flyer and 27 cm in the upper flyer (Figure 11).

Comparing the theoretical deformation with the survey, the maximum deviation measured in the lower flying buttress is 6 cm in the lower part and around 8 cm in the upper flyer, at the point of the upper crack. Despite these differences, the general form of the theoretical deformation agrees with the survey (Figure 12). Despite the deformations being visible, cracks have probably been filled in restoration works along the centuries and are not evident.

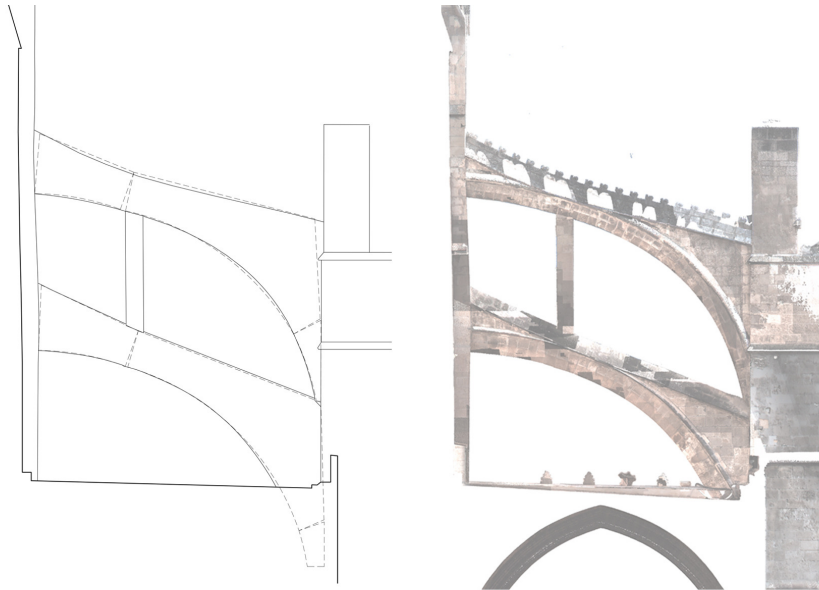


Figure 12. Comparison of the theoretical deformation (dashed line) with the real deformation (continuous line) (left) and orthophoto of the south flying buttresses B1 (right) (based on the point cloud by Rex Haberland).

The spreading that would cause the collapse of the flying buttresses shown in Figure 5 (right column), would be 1.38 m in the upper flyer and 1.81 m in the lower flyer. These movements are far from the actual movement of the flyers, which show a maximum opening of 44.5 cm in the south flying buttress B4 (Table 1).

The noticeable deformations have been a concern for the architects of the cathedral along history. The introduction of stone struts and even a wall between lower and upper flying buttresses is a proof of the fear of some of these master builders.⁹ Nonetheless, the flying buttresses are well designed as demonstrated by the fact that an equilibrium solution has been found and the deformations coincide with the expected. Therefore, there is no need for struts or walls between the two tiers of flying buttresses.

Pillars between the two flying buttresses are currently present in 4 of the 16 pairs. However, looking at historical photographs it is possible to verify that at least three more pillars were found in the first two pairs of flyers, close to the apse, with two under the lower flying buttress and another one between the lower and the upper flying buttresses (Figure 13). At some point, these pillars were removed, probably because they were the only three visible from the ground.¹⁰

2.3. Prevention of sliding. As discussed in Section 1, the flying buttresses of Mallorca are not connected to the nave wall. Therefore, sliding may occur for the line of minimum thrust. Note that the thrust against the wall in the lower flyers forms an angle of 42.4° , while in the upper flyers it is of 41.4° (Figure 10).

⁹In 1677 and 1739 experts recommended building stone “feet” (*peus de pedra*, in the original mallorquin) in the flying buttresses. These stone “feet” were probably these pillars [Domenge and Conejo 2003, p. 12]. About those concerns and historical expertise on the stability of the flying buttresses, see [Domenge 2017].

¹⁰As Rubió’s work is dated in 1912, presumably these pillars were removed after this date.

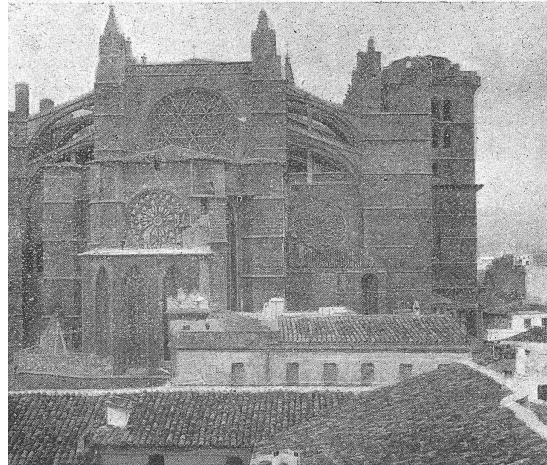


Figure 13. Exterior view of the cathedral of Mallorca from the east. Note the two pillars in the north flying buttresses and another one under the lower south flying buttress [Rubió i Bellver 1912].

For a common conservative friction coefficient of 0.75^{11} and for the minimum thrust, the first stone would slide down the wall in both cases. In Mallorca it is possible to observe some sliding, but only in a number of the upper flyers. In Figure 14 it is possible to notice the sliding of the second voussoir. It is important to remark that some interventions have been carried out to place the upper part of the flyer in its original position and to disguise the movement that would be very evident in the moldings. The fact that there is no sliding in the lower flying buttresses is probably because the actual thrust is larger than the minimum. This is expected, as it has to counteract the thrust of the main vault. This horizontal thrust of the main vault has been calculated by Huerta [2017, p. 28], obtaining a value of 340 kN.

As in the upper flying buttresses there is no thrust to counteract, their state is that of minimum thrust or close to it, and since they are in the limit of possible sliding, some of them present this problem while others do not. This difference most likely depends on small variations of the thrust or on the contact surface, as small irregularities on the surface can increase the friction coefficient.

Probably aware of the sliding problem, experts in the 17th and 18th centuries recommended the construction of bracing in the flyers [Domenge and Conejo 2003, p. 12]. It is a completely original solution that has not been found in other Gothic buildings (Figure 8 and Figure 16). The bracing solved the problem, but resulted in unexpected distortions. The effect is shown in Figure 15. When the span increases, three hinges appear in the flyer, one on the intrados at the springing, another one on the extrados close to the midpoint, and the third one in the bracing. When the bracing rotates, the space for the voussoirs between the bracing and the wall increases. As a result, the voussoirs slide and descend. However, further movements are constrained by the bracing itself. This causes a particular shape with double curvature in the upper part of the flying buttress, visible in some of them (Figure 16).

The master mason probably noticed this effect and tried to correct it with a small stone strut between the flying buttress and the bracing, as can be seen in Figure 17.

¹¹The friction angle in stone is usually between 30° and 40° .



Figure 14. Sliding in the upper flying buttress B6N. Note that the sliding is not between the wall and the first voussoir, but between first and second voussoirs [Photo: Roland Wiczorek, BTU Cottbus-Senftenberg].

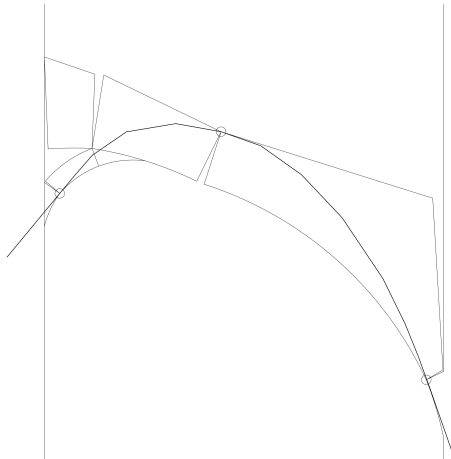


Figure 15. Line of minimum thrust for the flying buttress with the insertion of bracing.



Figure 16. Orthophoto of south flying buttresses B1 (based on the cloud of points by Rex Haberland).

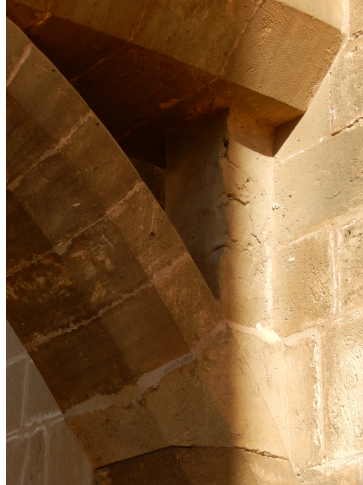


Figure 17. Small stud between the lower flying buttress and the support in B6S (photo: Huerta 2016).

3. Conclusions

The theoretical framework of limit analysis has been used to explain the behavior of flying buttresses. This theory can explain the characteristic movements of these elements, such as the distortions and some cases of sliding. A particular study of these effects has been carried out for the flying buttresses of the cathedral of Mallorca, which are some of the largest in Gothic architecture. These flying buttresses have a fundamental role in the stability of the cathedral. They are stable and admit an infinite range of lines of thrust in equilibrium with the loads, permitting the thrust to adapt to different combination of loads that may be experienced throughout the building's life. The visible distortions, that have been the origin of various interventions along history, are the normal movements expected in response to the leaning of the external buttresses, and this leaning is far from the one that would cause the collapse of the flyers. The struts and walls between the lower and upper flying buttresses are, therefore, not necessary and demonstrate the fear caused by the perceptible distortions. Some sliding problems can be observed, as well as the original solution of introducing stone bracings to prevent them. The use of these bracings led to a further problem of deformations and subsequent introduction of an additional element, that is, the studs between the head of the flying buttresses and the bracing.

Acknowledgements

I would like to thank Santiago Huerta for the very helpful comments and suggestions on this paper and the Cabildo of the Cathedral of Mallorca for facilitating the work in the building. This paper has been written within the post-doc research project: "The Art of Vaulting. Design and Construction of Large Vaults in the Mediterranean Gothic", in the DFG-Graduiertenkolleg 1913 "Cultural and Technological Significance of Historic Buildings" at the BTU Cottbus-Senftenberg. The project is conducted by Dr. phil. Anke Wunderwald and the author.

References

- [Domenge 2017] J. Domenge Mesquida, “La catedral de Mallorca: visures pro rimedio fabricae (1581–1668)”, in *Visurar l’arquitectura gòtica: inspeccions, consells i reunions de mestres d’obra (s. XIV–XVIII)*, edited by J. Domenge Mesquida and J. Vidal Franquet, Edizioni Caracol, Palermo, 2017.
- [Domenge and Conejo 2003] J. Domenge and A. Conejo, “Establecimiento y datación de las diferentes reparaciones y reformas constructivas de la catedral a lo largo de su historia (1575–1775)”, art. 3 in *Estudio, diagnóstico, peritación y en su caso planteamiento de actuaciones sobre el comportamiento constructivo estructural de la catedral de Santa María, en la ciudad de Palma, Isla de Mallorca (Balears)*, Polytechnic Univ. Catalunya, Barcelona, 2003.
- [Fitchen 1955] J. Fitchen, “A comment on the function of the upper flying buttress in French Gothic architecture”, *Gaz. Beaux-Arts* (6) **45** (1955), 69–90.
- [Fitchen 1961] J. Fitchen, *The construction of Gothic cathedrals: a study of Medieval vault erection*, Univ. Chicago Press, 1961.
- [Fuentes and Guerra 2015] P. Fuentes and R. Guerra, “Levantamiento para el análisis de estabilidad de la catedral de Mallorca”, technical report, Cabildo Catedral de Mallorca, 2015, <https://tinyurl.com/fuentguer>.
- [Fuentes and Guerra 2016] P. Fuentes and R. Guerra, “Ampliación del levantamiento para el análisis de estabilidad de la catedral de Mallorca”, technical report, Cabildo Catedral de Mallorca, 2016.
- [Fuentes and Wunderwald 2017] P. Fuentes and A. Wunderwald, “La construcción de las bóvedas de la catedral de Mallorca: una revisión bibliográfica”, pp. 611–623 in *Actas del Décimo Congreso Nacional y Segundo Congreso Internacional Hispanoamericano de Historia de la Construcción, II* (San Sebastián, 2017), edited by S. Huerta et al., Inst. Juan de Herrera, Madrid, 2017.
- [Fuentes and Wunderwald \geq 2018] P. Fuentes and A. Wunderwald, “The vaults of Mallorca Cathedral: rising to a technical challenge”, to appear in *The art of vaulting: design and construction of large vaults in the Mediterranean Gothic*, Kulturelle und technische Werte historischer Bauten **2**.
- [Heyman 1966] J. Heyman, “The stone skeleton”, *Int. J. Solids Struct.* **2:2** (1966), 249–279.
- [Heyman 1967] J. Heyman, “Beauvais Cathedral”, *Trans. Newcomen Soc.* **40:1** (1967), 15–35.
- [Heyman 1995] J. Heyman, *The stone skeleton: structural engineering of masonry architecture*, Cambridge Univ. Press, 1995.
- [Heyman 2008] J. Heyman, *Basic structural theory*, Cambridge Univ. Press, 2008.
- [Huerta Fernández 2017] S. Huerta Fernández, “Informe sobre la estabilidad de las bóvedas de la nave y el sistema de contrarresto de la catedral de Palma de Mallorca”, technical report, Cabildo Catedral de Mallorca, 2017, <http://oa.upm.es/45328>.
- [Nikolinakou et al. 2005] M. A. Nikolinakou, A. J. Tallon, and J. A. Ochsendorf, “Structure and form of early Gothic flying buttresses”, *Eur. J. Environ. Civ. Eng.* **9:9-10** (2005), 1191–1217.
- [Rosenberg 1936] G. Rosenberg, “The functional aspect of the Gothic style”, *J. R. Inst. Br. Archit.* **43:6** (1936), 273–290, 364–371.
- [Rubió i Bellver 1912] J. Rubió i Bellver, “Conferencia acerca de los conceptos orgánicos, mecánicos y constructivos de la Catedral de Mallorca”, *Anuario Asoc. Arquitectos Cataluña* **1912** (1912), 87–140.
- [Smars 2000] P. Smars, *Etudes sur la stabilité des arcs et voûtes: confrontation des méthodes de l’analyse limite aux voûtes gothiques en Brabant*, Ph.D. thesis, Katholieke Universiteit Leuven, 2000, <https://tinyurl.com/smarsphd>.
- [Ungewitter 1890] G. Ungewitter, *Lehrbuch der Gotischen Konstruktionen*, 3rd ed., Weigel, Leipzig, 1890.
- [UPC 2006–2008] “Estudio, diagnóstico, peritación y en su caso planteamiento de actuaciones sobre el comportamiento constructivo estructural de la catedral de Santa María, en la ciudad de Palma, Isla de Mallorca (Balears). Fase Segunda”, Polytechnic Univ. Catalunya, Barcelona, 2006–2008.
- [Viollet-le-Duc 1854] E.-E. Viollet-le-Duc, *Dictionnaire raisonné de l’architecture française du XIe au XVIe siècle, I*, Chapter “Arc-boutant”, pp. 60–83, A. Morel, Paris, 1854, <https://tinyurl.com/arcboutantJomms>.

Received 28 Apr 2018. Accepted 30 May 2018.

PAULA FUENTES: paula.fuentes@gmail.com
 Brandenburgische Technische Universität Cottbus-Senftenberg, Germany

ANALYSIS OF 3D NO-TENSION MASONRY-LIKE WALLS

DEBORAH BRICCOLA, MATTEO BRUGGI AND ALBERTO TALIERCIO

Modeling masonry as a linear elastic no-tension material, an original approach is implemented to analyze 3D structural elements, with special attention to walls. Masonry is replaced by a suitable equivalent orthotropic material with spatially varying elastic properties and negligible stiffness in case of tensile strain. An energy-based minimization problem is implemented to define the distribution and the orientation of the equivalent material for a given compatible load, so as to obtain a compressive state of stress throughout the structural element. A regular mesh of hexahedrons is used to speed up the sensitivity analysis. The capabilities of the approach in predicting no-tension stress solutions in masonry walls is shown, considering dead loads and both in-plane and out-of-plane live loads.

1. Introduction

Masonry, either of stone or brick, is well known to be a composite material with negligible tensile strength, at least orthogonally to the orientation of the mortar joints [Como 2016]. Indeed, most of the models available in the literature to cope with masonry structural elements either incorporate damage laws to describe the progressive microcracking and loss in strength due to tensile stresses (see in particular [Lourenço et al. 1997; Berto et al. 2002; Pelà et al. 2011]), or neglect tensile strength completely [Del Piero 1989; Cuomo and Ventura 2000; Angelillo et al. 2010]. The former family of models provides an effective prediction of the real mechanical response of masonry elements beyond the elastic range. Unfortunately, the determination of the several parameters that define these models is generally a difficult task [Lourenço 2001].

The use of a no-tension material model is apparently very appealing, mainly because it avoids uncertainties related to the estimation of the material tensile strength. Additionally, it is based on a conservative assumption. The no-tension model allows the structural behavior to be evaluated assuming the stress tensor to be negative semidefinite and to depend linearly upon the elastic part of the strain; see e.g., [Benvenuto 1991]. Notwithstanding the apparent simplicity of the no-tension model, the expected discontinuities in the stress and displacement fields give rise to several numerical issues. An overview of the numerical difficulties related to the inherent nonlinearity of the problem can be found, e.g., in [Cuomo and Ventura 2000; Alfano et al. 2000; Marfia and Sacco 2005], where procedures to overcome these issues are investigated as well.

Alternatively, the no-tension assumption can be robustly handled through the minimization of a suitable form of the elastic strain energy. A numerical method was originally proposed in [Angelillo et al. 2010] that seeks the equilibrium of two-dimensional no-tension bodies through the minimization of

The authors gratefully acknowledge the financial support of Fondazione Cariplo through grant number 2017-0317 and Italian Ministry of Education University and Research through grant number 2015JW9NJT.

Keywords: no-tension materials, masonry walls, pushover analysis.

the potential energy. Following this approach, an equivalent optimization problem was formulated in [Bruggi 2014] and implemented in [Bruggi and Taliercio 2015] to investigate the in-plane and out-of-plane behavior of masonry walls through simplified 2D models.

Limit analysis can also be applied to evaluate the collapse load and the relevant failure mechanism(s) of no-tension masonry walls. According to Heyman [1966],

- (i) the tensile strength is assumed to vanish,
- (ii) the “tensile strains” are assumed to be unbounded, and
- (iii) the compressive strength of masonry is assumed to be unlimited.

The above assumptions match the behavior of a standard ductile material for which classical limit analysis applies. Limit analysis focuses on the incipient collapse (strains in compression are completely neglected in favor of the additional assumption of rigid-block mechanisms), whereas the linear elastic no-tension model can handle both serviceability and incipient collapse.

This contribution extends the formulation originally presented in [Bruggi 2014] for two-dimensional problems to three-dimensional ones, with special attention to masonry walls. The real no-tension material is replaced by an equivalent orthotropic material, exhibiting negligible stiffness in any direction along which a tensile strain arises. The elastic constants of the equivalent material along its symmetry axes are reduced with respect to those of the real material using a smooth penalization law. For any given load that is compatible with the no-tension assumption, the equilibrium of the body is sought by minimizing the strain energy with respect to the distribution of the equivalent orthotropic material. The proposed algorithm is implemented using displacement-based finite elements and methods of sequential convex programming. A regular mesh of eight node displacement-based finite elements is used to speed up the sensitivity analysis required by the minimization algorithm.

The capabilities of the approach in predicting no-tension stress solutions in masonry walls is shown by addressing both in-plane and out-of-plane loads. The collapse load of walls subject to horizontal actions is predicted by running a sequence of independent analyses on the same discrete model.

The layout of the paper is as follows. The mathematical formulation of the problem governing the analysis of no-tension bodies is described in Section 2: the properties of the equivalent orthotropic material are defined in Section 2A, whereas the energy-based approach employed to distribute and determine the directions of the equivalent orthotropic material is outlined in Section 2B. To assess the capabilities of the proposed approach in the simulation of the structural response of three-dimensional no-tension structures, four case studies are presented in Section 3. Finally, the main results of the work are summarized and ongoing developments of the research are outlined in Section 4.

2. Problem formulation

2A. Equivalent orthotropic material. A 3D solid made of an isotropic linear elastic masonry-like material occupies a domain Ω . A triplet of orthogonal Cartesian (global) coordinates, z_1, z_2, z_3 , defines the position of any point $\chi \in \Omega$. The material does not support tension, meaning that the stress tensor σ is negative semidefinite. The infinitesimal strain tensor ϵ is assumed to be the sum of an elastic part ϵ^e , related to the stress σ through a linear constitutive tensor, and a “latent” part ϵ^c , a positive semidefinite strain that is orthogonal to σ and accounts for cracks. The above material model differs from the Heyman

assumptions outlined in the introduction in that it takes into account a finite stiffness in compression. Reference is made to [Fortunato et al. 2016; 2018] for recent developments on the application of the unilateral material model to the structural analysis of masonry structures.

Let σ_α ($\alpha = I, II, III$) be the eigenvalues of the stress tensor $\boldsymbol{\sigma}$ at $\boldsymbol{\chi}$, being $\sigma_I \leq \sigma_{II} \leq \sigma_{III}$. The material behavior at $\boldsymbol{\chi}$ depends on the sign of the principal stresses. If $\sigma_{III} < 0$, it behaves like an isotropic material. If one or two of the principal stresses are equal to zero, it turns into an orthotropic material: the material behaves elastically along the direction(s) of the principal compressive stress(es), whereas “cracking strains” $\boldsymbol{\epsilon}_c \geq 0$ arise perpendicularly to the compressive isostatic line(s). If $\sigma_I = 0$, the material behaves like a “void phase”, meaning that any positive semidefinite cracking strain is allowed.

A suitable equivalent orthotropic material can be defined to match the outlined behavior. Let \tilde{z}_i ($i = 1, 2, 3$) be the symmetry axes of the equivalent material, which locally coincide with the principal stress directions z_α ($\alpha = I, II, III$) at any point in Ω . Using the notation proposed in [Mehrabadi and Cowin 1990], the constitutive law for the orthotropic material can be written, in its inverse form, as $\tilde{\boldsymbol{\epsilon}} = \tilde{\mathbf{C}}\tilde{\boldsymbol{\sigma}}$, where

$$\tilde{\boldsymbol{\epsilon}} = \begin{Bmatrix} \tilde{\epsilon}_{11} \\ \tilde{\epsilon}_{22} \\ \tilde{\epsilon}_{33} \\ \sqrt{2}\tilde{\epsilon}_{12} \\ \sqrt{2}\tilde{\epsilon}_{23} \\ \sqrt{2}\tilde{\epsilon}_{31} \end{Bmatrix}, \quad \tilde{\boldsymbol{\sigma}} = \begin{Bmatrix} \tilde{\sigma}_{11} \\ \tilde{\sigma}_{22} \\ \tilde{\sigma}_{33} \\ \sqrt{2}\tilde{\sigma}_{12} \\ \sqrt{2}\tilde{\sigma}_{23} \\ \sqrt{2}\tilde{\sigma}_{31} \end{Bmatrix} \quad (2-1)$$

and the compliance tensor reads

$$\tilde{\mathbf{C}} = \begin{bmatrix} 1/\tilde{E}_1 & -\tilde{\nu}_{21}/\tilde{E}_2 & -\tilde{\nu}_{31}/\tilde{E}_3 & 0 & 0 & 0 \\ -\tilde{\nu}_{12}/\tilde{E}_1 & 1/\tilde{E}_2 & -\tilde{\nu}_{32}/\tilde{E}_3 & 0 & 0 & 0 \\ -\tilde{\nu}_{13}/\tilde{E}_1 & -\tilde{\nu}_{23}/\tilde{E}_2 & 1/\tilde{E}_3 & 0 & 0 & 0 \\ 0 & 0 & 0 & 1/\tilde{G}_{12} & 0 & 0 \\ 0 & 0 & 0 & 0 & 1/\tilde{G}_{23} & 0 \\ 0 & 0 & 0 & 0 & 0 & 1/\tilde{G}_{31} \end{bmatrix}. \quad (2-2)$$

In (2-2), \tilde{E}_i ($i = 1, 2, 3$) is the Young’s modulus of the equivalent material along the symmetry axis \tilde{z}_i , \tilde{G}_{ij} ($i, j = 1, 2, 3$) is the shear modulus in the symmetry plane $(\tilde{z}_i, \tilde{z}_j)$ and $\tilde{\nu}_{ij}$ ($i, j = 1, 2, 3$) is the Poisson’s ratio along \tilde{z}_j under uniaxial tension along \tilde{z}_i . The equalities $\tilde{\nu}_{12}/\tilde{E}_1 = \tilde{\nu}_{21}/\tilde{E}_2$, $\tilde{\nu}_{13}/\tilde{E}_1 = \tilde{\nu}_{31}/\tilde{E}_3$, and $\tilde{\nu}_{23}/\tilde{E}_2 = \tilde{\nu}_{32}/\tilde{E}_3$ hold.

The elastic properties of the equivalent orthotropic material along its symmetry axes are assumed to be governed by three nondimensional fields ρ_i ($i = 1, 2, 3$) whose values range between $\rho_{\min} (> 0)$ and 1, as

$$\tilde{E}_i = \rho_i^p E, \quad \tilde{\nu}_{ij} = \sqrt{\rho_i^p / \rho_j^p} \nu, \quad \tilde{G}_{ij} = \sqrt{\rho_i^p \rho_j^p} G \quad (i, j = 1, 2, 3), \quad (2-3)$$

where E , ν , and $G = E/(2(1 + \nu))$ are the Young’s modulus, the Poisson’s ratio and the shear modulus of the isotropic material, respectively, and p is a penalization parameter (taken equal to 3; see, e.g., [Bendsøe and Sigmund 1999]). ρ_i ($i = 1, 2, 3$) can be seen as “normalized material densities” along \tilde{z}_i . The interpolation in (2-3) is conceived so as to provide vanishing stiffness in any direction along which a variable attains its minimum value, while full stiffness is preserved in any direction along which a variable

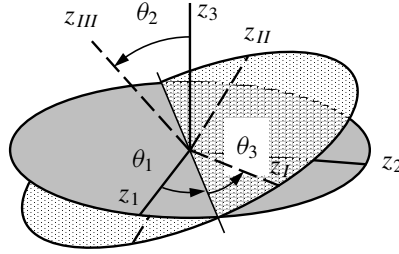


Figure 1. Euler's angles defining the orientation of the symmetry axes of the equivalent orthotropic material to the global reference system.

attains its maximum value. This allows the stress-dependent elastic properties of the isotropic no-tension material to be matched; see also the anisotropic damage law proposed in [Papa and Taliercio 2005]. A strictly positive lower bound, ρ_{\min} , is needed to avoid any singularity of the compliance tensor $\tilde{\mathbf{C}}$. This is needed in order to ensure that the stiffness matrix of the body \mathbf{K} is positive definite when using a finite element discretization to solve the elasticity equations for any set of normalized material densities. In view of the adoption of optimization methods, normalized material densities are formulated as continuous variables, instead of discrete ones, to exploit efficient methods of mathematical programming for large scale problems; see Section 2B.

Finally, denoting by $\boldsymbol{\sigma}$ and $\boldsymbol{\epsilon}$ the arrays of the stress and strain components in the global Cartesian reference system $Oz_1z_2z_3$, the direct form of the stress-strain law in this system can be written as

$$\boldsymbol{\sigma} = \mathbf{D}(\rho_1, \rho_2, \rho_3; \theta_1, \theta_2, \theta_3)\boldsymbol{\epsilon}, \quad (2-4)$$

where θ_i ($i = 1, 2, 3$) are the Euler's angles that provide the orientation of the symmetry axes of the equivalent orthotropic material with respect to the global Cartesian reference system as represented in Figure 1 (see, e.g., [Rovati and Taliercio 2003]) and

$$\mathbf{D} = \mathbf{q}\tilde{\mathbf{D}}\mathbf{q}^T. \quad (2-5)$$

In (2-5) the stiffness tensor $\tilde{\mathbf{D}} = \tilde{\mathbf{C}}^{-1}$ and $\mathbf{q} = \mathbf{q}(\theta_1, \theta_2, \theta_3)$ is a transformation matrix which can be split into four submatrices:

$$\mathbf{q} = \begin{bmatrix} \mathbf{q}_{AA} & \mathbf{q}_{AB} \\ \mathbf{q}_{BA} & \mathbf{q}_{BB} \end{bmatrix}; \quad (2-6)$$

the entries of the submatrices are given by

$$\begin{aligned} (\mathbf{q}_{AA})_{ij} &= Q_{i\alpha}^2, & (\mathbf{q}_{AB})_{ij} &= \sqrt{2} \epsilon_{\alpha\beta\gamma} Q_{i\beta} Q_{j\gamma}, \\ (\mathbf{q}_{BA})_{ij} &= \sqrt{2} \epsilon_{ihk} Q_{h\alpha} Q_{k\alpha}, & (\mathbf{q}_{BB})_{ij} &= \epsilon_{ihk} \epsilon_{\alpha\beta\gamma} (Q_{h\beta} Q_{k\gamma} + Q_{h\gamma} Q_{k\beta}). \end{aligned} \quad (2-7)$$

In (2-7), $Q_{i\alpha}$, etc., are the director cosines of the principal stress directions (i.e., the material symmetry axes of the equivalent orthotropic material) to the global reference system: $Q_{i\alpha} = \cos(z_i, z_\alpha)$ ($i = 1, 2, 3$; $\alpha = I, II, III$). Summation is implied over any repeated index, and $\alpha = I$ if $j = 1$, $\alpha = II$ if $j = 2$, $\alpha = III$ if $j = 3$. Unlike the classical alternating symbol, ϵ_{ihk} and $\epsilon_{\alpha\beta\gamma}$ are equal to 1 if (i, h, k) or (α, β, γ) are even permutations of $(1, 2, 3)$ or (I, II, III) , respectively, and vanish in any other case (see, e.g., [Cowin and Mehrabadi 1995]).

2B. Energy-based analysis of no-tension 3D solids. In Section 2A an elastic orthotropic material has been defined, which matches the behavior of the no-tension solid through suitable stiffness relaxations provided by the set of normalized material densities. Cracking strains arise along the axes of negligible stiffness (for minimum values of these normalized densities) mainly to restore strain compatibility; see in particular [Angelillo et al. 2010]. This allows the behavior of the no-tension solid to be modeled for any multiaxial stress state using a single material model, with point-wise varying elastic constants. Stress and/or strain discontinuities are matched by abrupt changes in the normalized material density fields.

The equilibrium of any linear elastic no-tension solid can be solved through an energy-based approach as a problem of optimal distribution of material; see [Bruggi 2014] for the 2D rationale. The equivalent orthotropic material defined in Section 2A is distributed over the body to minimize the overall strain energy while enforcing nonpositive principal stresses everywhere.

Adopting a displacement-based numerical approach, the continuous formulation of this minimization problem can be stated as follows:

$$\begin{aligned} \min_{\rho_1, \rho_2, \rho_3} \mathcal{E} &= \frac{1}{2} \int_{\Omega} \boldsymbol{\epsilon}^T(\mathbf{u}) \mathbf{D}(\rho_1, \rho_2, \rho_3; \theta_1, \theta_2, \theta_3) \boldsymbol{\epsilon}(\mathbf{u}) d\Omega \\ \text{such that } \int_{\Omega} \boldsymbol{\epsilon}^T(\mathbf{u}) \mathbf{D} \boldsymbol{\epsilon}(\mathbf{v}) d\Omega &= \int_{\Gamma_t} \mathbf{t}_0^T \mathbf{v} d\Gamma \quad \forall \mathbf{v} \in H^1, \quad \mathbf{u}|_{\Gamma_u} = \mathbf{u}_0, \\ \theta_1, \theta_2, \theta_3 \mid \tilde{z}_1 = z_I, \tilde{z}_2 = z_{II}, \tilde{z}_3 = z_{III}, \\ \rho_1, \rho_2, \rho_3 \mid \sigma_I \leq 0, \sigma_{II} \leq 0, \sigma_{III} \leq 0, \\ \rho_{\min} \leq \rho_1, \rho_2, \rho_3 \leq 1. \end{aligned} \quad (2-8)$$

In the above statement, the minimization unknowns are the fields of the “densities” ρ_i ($i = 1, 2, 3$) whereas the objective function is the elastic strain energy computed through the displacements \mathbf{u} over the 3D domain Ω . Γ_u stands for the part of the boundary that is subjected to the given traction \mathbf{t}_0 , whereas Γ_t undergoes prescribed displacements \mathbf{u}_0 , being $\Gamma = \Gamma_t \cup \Gamma_u$. Equation (2-8).2 enforces elastic equilibrium in Ω and along Γ_t for any set of normalized densities, being the gradients of \mathbf{u} and \mathbf{v} square integrable; Equation (2-8).3 prescribes alignment of the symmetry axes of the equivalent orthotropic material to the principal stress directions of the no-tension solid; Equation (2-8).4 requires the normalized densities to define a compression-only stress state all over the domain.

A regular mesh of 8-node hexahedrons is adopted in the simulations to speed up the numerical procedure. Being N the number of discrete solid elements, the proposed formulation reads as follows:

$$\begin{aligned} \min_{x_{1e}, x_{2e}, x_{3e}} \mathcal{E} &= \frac{1}{2} \sum_{e=1}^N \mathbf{U}_e^T \mathbf{K}_e(x_{1e}, x_{2e}, x_{3e}; t_{1e}, t_{2e}, t_{3e}) \mathbf{U}_e, \\ \sum_{e=1}^N \mathbf{K}_e(x_{1e}, x_{2e}, x_{3e}; t_{1e}, t_{2e}, t_{3e}) \mathbf{U}_e &= \mathbf{f}, \\ t_{1e}, t_{2e}, t_{3e} \mid \tilde{z}_1 = z_I, \tilde{z}_2 = z_{II}, \tilde{z}_3 = z_{III}, \\ x_{1e}, x_{2e}, x_{3e} \mid \sigma_{Ie}, \sigma_{IIe}, \sigma_{IIIe} &\leq 0, \\ 0 < x_{\min} \leq x_{1e}, x_{2e}, x_{3e} &\leq 1, \\ e &= 1 \dots N. \end{aligned} \quad (2-9)$$

The objective function is computed over the N hexahedrons using the same element stiffness matrix, \mathbf{K}_e , and the array of the nodal displacements of each element of the regular mesh \mathbf{U}_e ; \mathbf{f} denotes the array gathering the equivalent nodal loads; t_{1e}, t_{2e}, t_{3e} are the Euler's angles defining the orientation of the equivalent material, i.e., the principal stress directions in the no-tension body in the e -th element. The three sets of element-wise unknowns x_{1e}, x_{2e}, x_{3e} correspond to the “normalized material densities” along the symmetry axes of the equivalent orthotropic material in any finite element e .

Details on the numerical implementation of the problem in (2-9) can be found in [Bruggi 2014]. The extension of the minimization algorithm from two to three dimensions is straightforward. The method of moving asymptotes [Svanberg 1987] is used to handle the minimization. At each iteration, the current value of the objective function \mathcal{E} and its sensitivities with respect to the densities are needed. This simply reads

$$\frac{\partial \mathcal{E}}{\partial x_{ie}} = -\frac{1}{2} \mathbf{U}_e^T \frac{\partial \mathbf{K}_e}{\partial x_{ie}} \mathbf{U}_e. \quad (2-10)$$

Instead of implementing demanding stress constraints, following [Ananiev 2005] an efficient procedure that penalizes the energy contributions (and the relevant sensitivities) related to any tensile strain is implemented, thus enforcing a compression-only stress regime. The adoption of a regular mesh of finite elements speeds up remarkably the computation of the quantities in (2-10).

By repeatedly calling the minimization algorithm for different values of the live loads, the collapse load of the structural wall can also be estimated as the value beyond which convergence is lost.

As already mentioned in Section 1, an energy-based approach to the analysis of linear elastic masonry-like materials was presented in [Angelillo et al. 2010] using displacements as unknowns and the total potential energy as the objective function. The elastic problem with unilateral stress constraints was successfully solved through descent methods, by formulating an efficient unconstrained minimization of a convex function.

Alternatively, the energy-based approach proposed in [Bruggi 2014], here extended to three-dimensional bodies, relies on most common methods and techniques used in structural optimization. Normalized material densities govern the stiffness of the equivalent orthotropic material, i.e., the strain energy in the no-tension material, depending on the stress state; see Equation (2-8).4. This allows the equilibrium of linear elastic no-tension bodies to be solved by means of algorithms that were originally conceived to solve large scale problems in structural optimization. The computational cost of the proposed approach is investigated in Section 3 with reference to Example 3.4.

3. Numerical applications

In the last decades, finite element approaches for no-tension materials have been extensively adopted to predict collapse multipliers of structural elements as an alternative to limit analysis [Fortunato et al. 2016; 2018; Angelillo et al. 2010; Bruggi and Taliercio 2015]. Four preliminary examples are considered to assess the numerical method presented above, considering vertical dead loads and horizontal live forces. The first one addresses the in-plane collapse mechanism of a reference wall that was previously investigated, among others, in [Maier and Nappi 1990; Bruggi 2014]; the second one focuses on a typical out-of-plane mechanism of a portion of a wall between contiguous stories, which was already investigated in [Bruggi and Taliercio 2015] using a 2D model and the rigid no-tension assumption. The third example

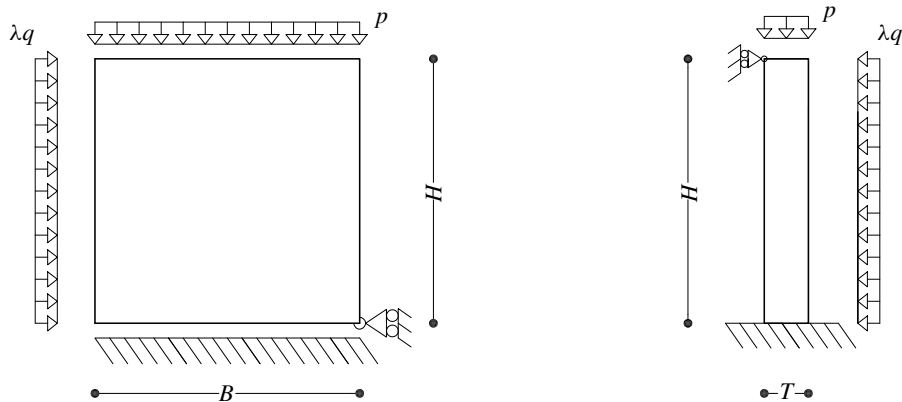


Figure 2. Geometry and boundary conditions for the Examples 3.1 (left) and 3.2 (right).

is a variation of the latter one, which fully exploits the capabilities of the proposed approach to solve the no-tension equilibrium of a three-dimensional solid with any boundary conditions. Finally, the fourth example analyzes the effect of a ground settlement below two intersecting walls.

To enforce consistent loads, i.e., loads for which a no-tension solution is feasible, in all the examples hereafter a compressive prestress equal to 0.01 MPa is applied all over the vertical sides of the walls.

Walls made of no-tension material are taken into account. Referring to Example 3.2, the results given by a conventional linear elastic material model, with symmetric behavior in tension and compression, are also shown to highlight the dramatic difference with respect to those given by the no-tension model.

Plots showing the principal stress directions at the center of each finite element are reported in this section. In these figures, blue stands for compression, whereas red stands for tension. The length of the lines is proportional to the value of the relevant principal stress, and is scaled by the maximum stress represented in each plot.

Example 3.1. A square panel similar to that dealt with in [Maier and Nappi 1990] and investigated, among others, in [Fuschi et al. 1995; Bruggi 2014], is considered. The width and height of the panel are $B = H = 1$ m, and the thickness $T = 0.25$ m. A side view (longitudinal) is depicted in Figure 2 (left). The panel is simply supported at the bottom, and is horizontally constrained along the right edge of the base. The Young's modulus is assumed equal to 1000 MPa, while the Poisson ratio $\nu = 0.2$. A uniform vertical dead load p of 72 kN/m² is applied along the top side. A horizontal live load λq acts on the left side along the longitudinal direction, being $q = 40$ kN/m² and λ the load multiplier.

The behavior of the panel for increasing horizontal loads can be captured effectively by a curve representing the displacement of a control point (herein the top right corner) versus the load multiplier. In Figure 3, the solid line represents the outcome of the numerical simulations originally performed in [Maier and Nappi 1990] adopting an incremental approach over a mesh of $8 \times 8 = 64$ square elements, whereas dots stand for results achieved by the proposed energy-based procedure using a discretization of $8 \times 8 \times 2 = 128$ cubic elements. It must be remarked that, for each prescribed value of the load multiplier, the formulation in (2-9) allows the relevant displacement of the control point to be evaluated independently of the previous history. Indeed, simulations were performed for a limited set of multipliers, i.e., 0, 0.5, 1, 1.5, 1.7, 1.8, 1.85, 1.9, 1.95, 2. The last converged simulation was at $\lambda = 1.95$.

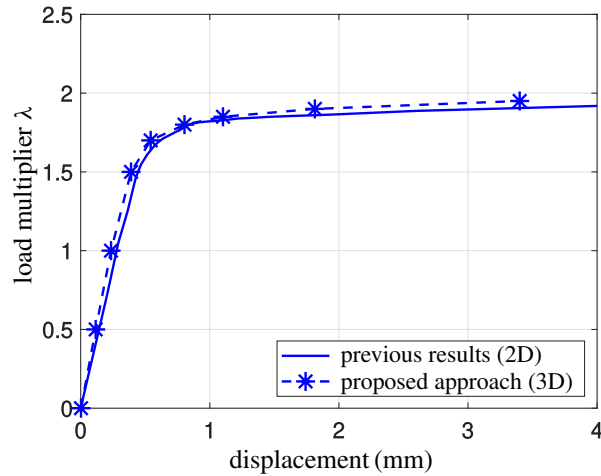


Figure 3. Example 3.1. Top right horizontal displacement of the panel vs. load multiplier λ . Previous results are from [Maier and Nappi 1990].

Referring to $\lambda = 1$, Figure 4 (left) shows the computed distribution of linear isotropic material and nonlinear orthotropic material in the panel. White stands for zones in compression where no inelastic strain is expected ($x_{1e} = x_{2e} = x_{3e} = 1$) and the panel has full stiffness. Black stands for regions where some inelastic strain arises (at least one of the three unknowns is equal to x_{\min}) and cracks weaken the panel. Figure 5 (top) shows two views of the relevant map of the principal compressive stresses (blue lines). Vertical compressive reactions are allowed along the base, except for the very first two elements where cracking strains arise. The effect on the overall deformability of the structural element is negligible; see the relevant displacement in Figure 3.

Figure 4 (right) shows the computed distribution of linear isotropic material and nonlinear orthotropic

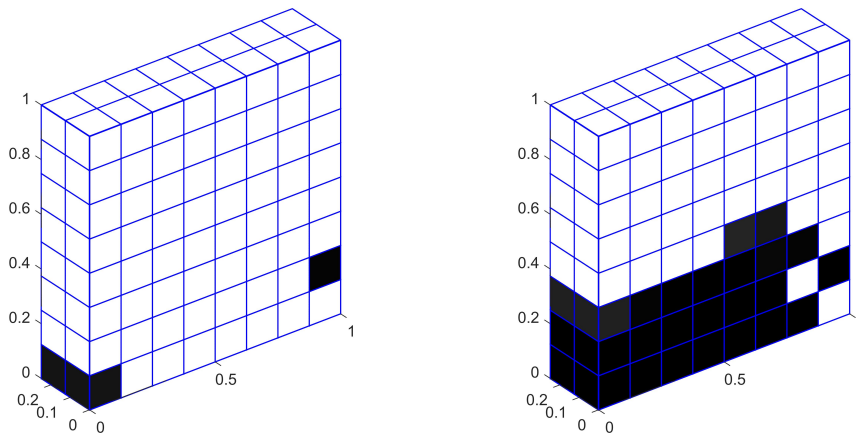


Figure 4. Example 3.1. Distribution of linear isotropic material (white) and nonlinear orthotropic material (black) at $\lambda = 1$ (left) and $\lambda = 1.95$ (right).

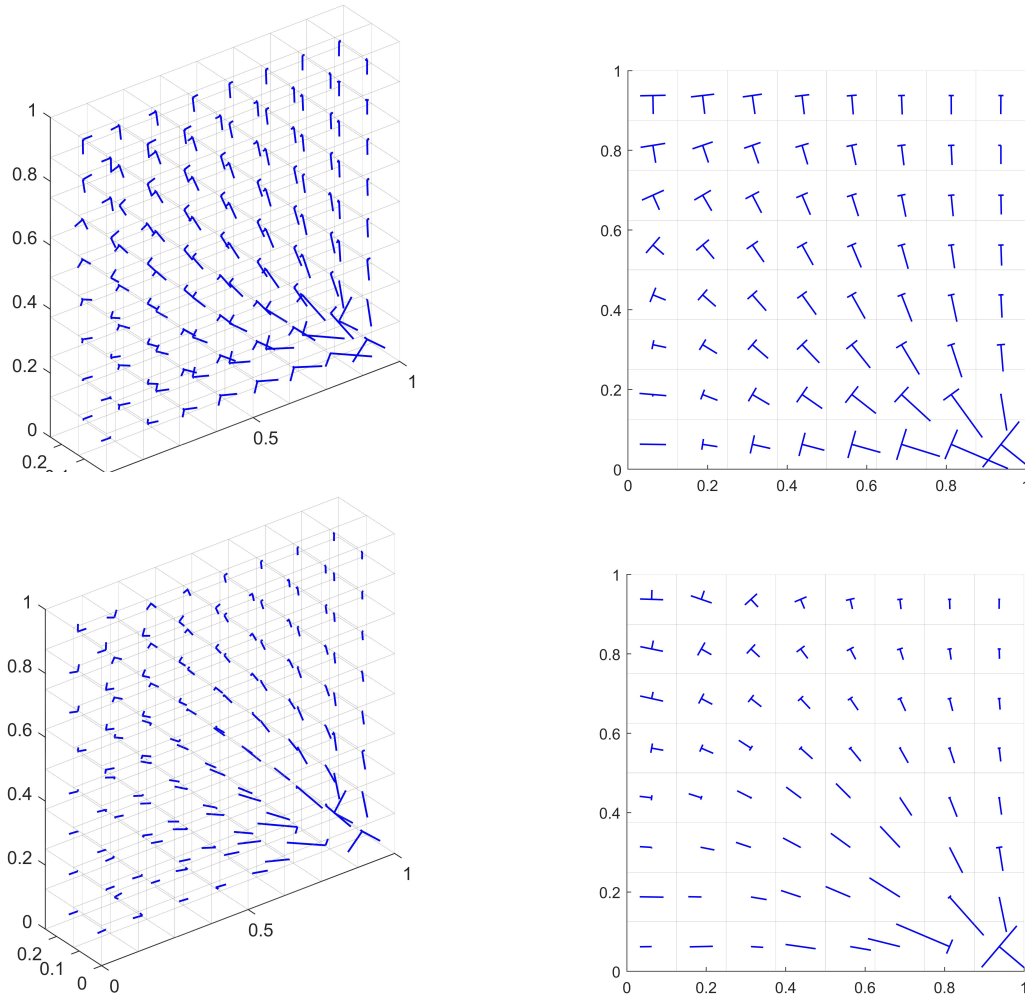


Figure 5. Example 3.1. Principal compressive stresses at $\lambda = 1$ (top) and $\lambda = 1.95$ (bottom).

material at $\lambda = 1.95$, whereas Figure 5 (bottom) shows two views of the relevant map of the principal compressive stresses. Apart from the region in the vicinity of the ground hinge, compressive stresses at the base of the panel are mainly horizontal, whereas an extended cracked zone has a remarkable effect in terms of deformability of the structural element. The global collapse of the structure is incipient. Indeed, no convergence of the proposed minimization procedure can be found at higher values of the load multiplier.

Example 3.2. The second example deals with a rectangular panel of width $B = 0.5$ m, height $H = 1$ m, and thickness $T = 0.25$ m. A side view (lateral) is depicted in Figure 2 (right). The panel is made of a no-tension material having the same mechanical properties used in the previous example. A uniform vertical dead load $p = 120$ kN/m² is applied at the top. A horizontal live load λq acts on the left side

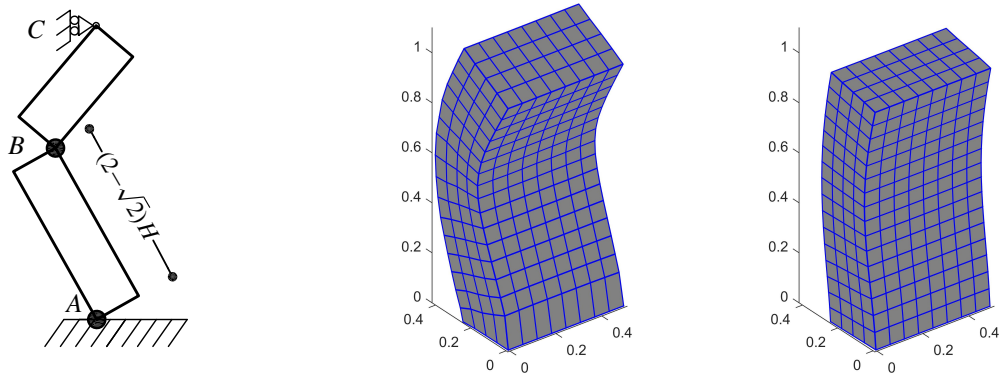


Figure 6. Example 3.2. Theoretical collapse mechanism (left) and magnified displacements at $\lambda = 2.1$ for no-tension material (middle) and conventional material (right).

along the transversal direction, being $q = 20 \text{ kN/m}^2$ and λ the load multiplier. The panel is pinned at the base. Transversal displacements are constrained also at the top of the wall.

A similar geometry has been used in [Bruggi 2014] to investigate the out-of-plane behavior of a reference section of a masonry wall under seismic actions, relying on a two-dimensional modeling. Assuming a three-hinge mechanism (see Figure 6 (left)) limit analysis can be straightforwardly applied to compute both the location of the central hinge in the collapse mode, $y_h = (2 - \sqrt{2})H$, and the relevant multiplier

$$\lambda_c = \frac{pT^2}{qH^2}(2\sqrt{2} + 3). \quad (3-1)$$

With the values of the geometrical parameters detailed above, one gets $y_h = 0.59 \text{ m}$ and $\lambda_c = 2.18$.

A limited set of simulations was performed with the proposed approach at $\lambda = 1.9, 2, 2.1$, and 2.2 . The last converged simulation was at $\lambda = 2.1$. Pictures presented next refer to this value of the load multiplier, i.e., to the wall on the verge of collapse.

A plot of the magnified displacements at incipient collapse is represented in Figure 6 (middle). Strains are localized at the base of the wall and, approximately, at 0.6 m from the ground, in good agreement with the position of hinges A and B in Figure 6 (left). At the same load and the same magnification factor, Figure 6 (right) shows the displacement map in case of a conventional linear elastic material with symmetric behavior in tension and compression.

Figure 7 (left) shows the principal stresses computed at the estimated collapse multiplier in the no-tension panel. Two views are shown; the second is a side view of the stress map in a vertical section of the wall.

The flux of compressive stresses found in the lower and in the central region of the panel is confined in a very limited part of the section. Indeed, hinges A and B are expected to activate for any additional infinitesimal increase in the live load.

Stress maps are remarkably different if a conventional material with symmetric behavior in tension and compression is considered in the simulations; see Figure 7 (right). At the same load, compressive regions are much more extended than in the case of a no-tension material. Additionally, it must be

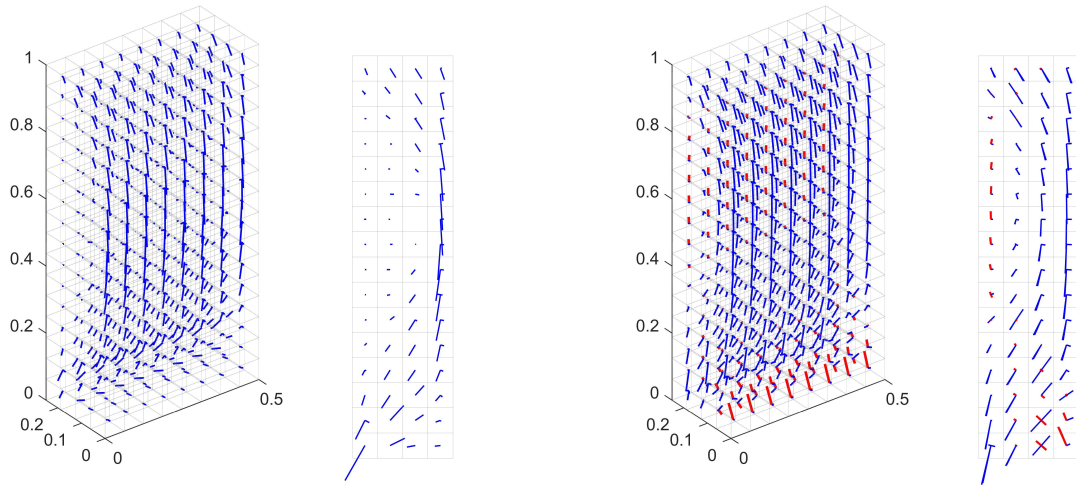


Figure 7. Example 3.2. Principal stresses at $\lambda = 2.1$: no-tension material (left) vs. conventional material (right). For each material two views are shown, the second one corresponding to a vertical section of the wall.

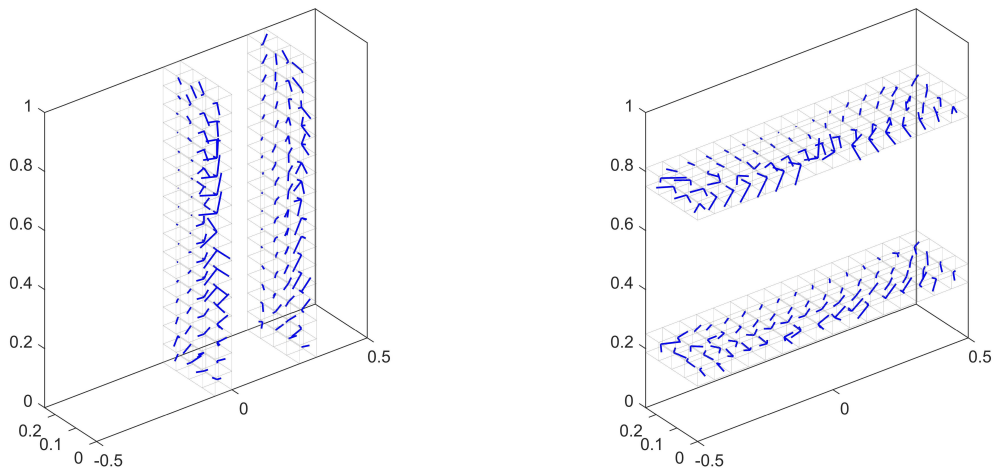


Figure 8. Example 3.3. Principal compressive stresses at $\lambda = 4.2$ along representative vertical and horizontal sections.

remarked that the maximum compressive stress computed at the base of the wall for the conventional material is approximately 30% lower than that found for the no-tension material.

These crucial differences show that the conventional material model should not be used to capture the behavior of masonry structures. The negligible tensile strength and the occurrence of cracks remarkably affect the stress field within the wall.

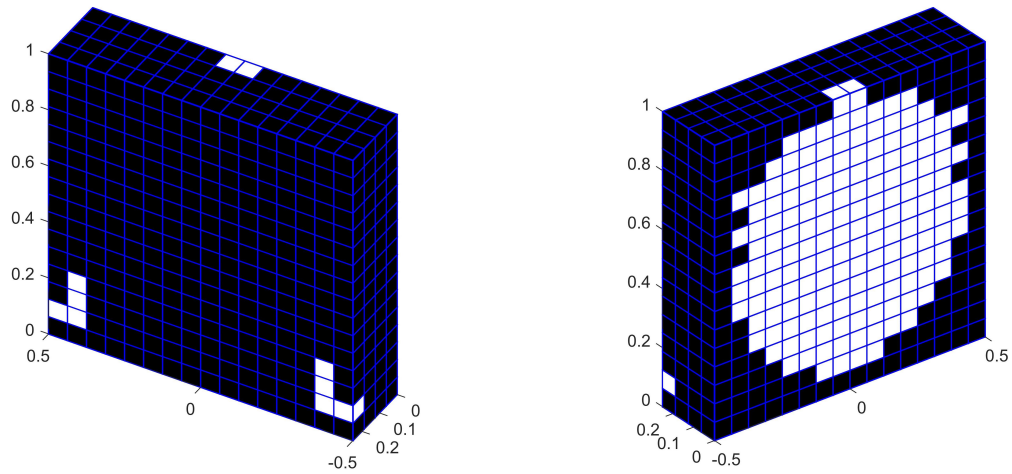


Figure 9. Example 3.3. Distribution of linear isotropic (white) and nonlinear orthotropic (black) material at $\lambda = 4.2$.

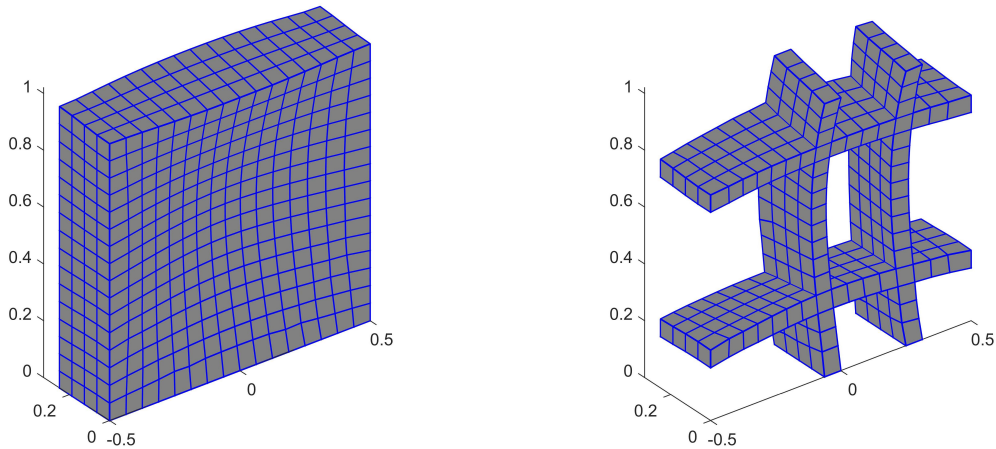


Figure 10. Example 3.3. Magnified displacements at $\lambda = 4.2$.

Example 3.3. This example is a variation of the previous one. The material and geometry are the same, apart from the width of the panel that is doubled, i.e., $B = 1$ m. Indeed, $p = 60$ kN/m² and $q = 10$ kN/m². Boundary conditions at the bottom and the top are unchanged. Additionally, horizontal displacements are restrained in both the longitudinal and transverse direction all over the shortest vertical sides.

The proposed numerical approach is used to investigate the three-dimensional stress state that arises in the panel made of no-tension material. The case $\lambda = 4.2$ is considered.

At each point of the panel, the horizontal load is essentially transferred to the ground by two static schemes that work together. A map of the principal stress directions is shown in Figure 8 addressing two vertical sections and two horizontal sections that are representative of the main load paths. In the

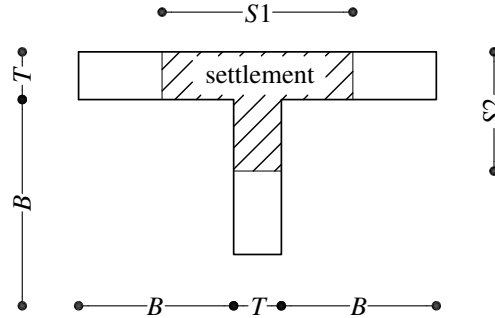


Figure 11. Geometry for Example 3.4.

vertical sections, stresses flow to the top side and the bottom side of the panel in a way similar to Figure 7 (left). In the horizontal sections, stresses flow towards the sides of the panel following effective arch-like patterns. Due to the assumption of perfect constraints, an ideal scheme like this one does not give rise to a mechanism; see, e.g., [Como 2016]. Trusts at the lateral springers and allowable compressive stresses can be alternatively controlled to discuss the feasibility of the applied load. Both quantities can be evaluated through the proposed numerical approach.

Figure 9 shows a map of the computed distribution of linear isotropic material and nonlinear orthotropic material in the panel. Cracking strains are expected to weaken the panel in the extended regions marked in black. Figure 10 shows the magnified deformed geometry of the panel (left) and the two sets of representative sections above referred (right). In the loaded side, inelastic strains are mostly located around the constrained boundaries.

Example 3.4. We now consider a T-shaped wall, whose plan view is shown in Figure 11. The wall (of width $B = 0.8$ m, thickness $T = 0.25$ m, and height $H = 1$ m) is subject to vertical loads of arbitrary intensity at the top. To simulate the effect of a vertical settlement affecting the connection, the base of the

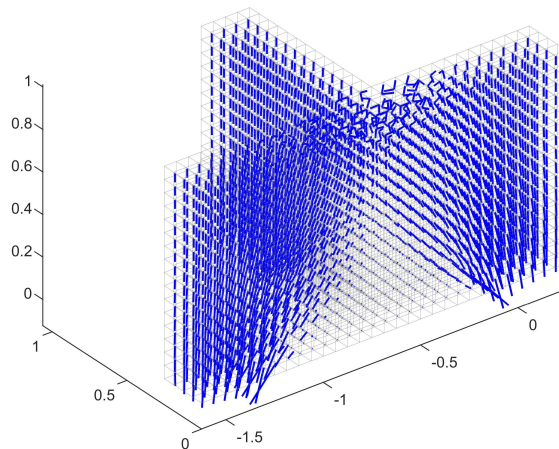


Figure 12. Example 3.4. Principal compressive stresses in case of a vertical settlement: 3D view.

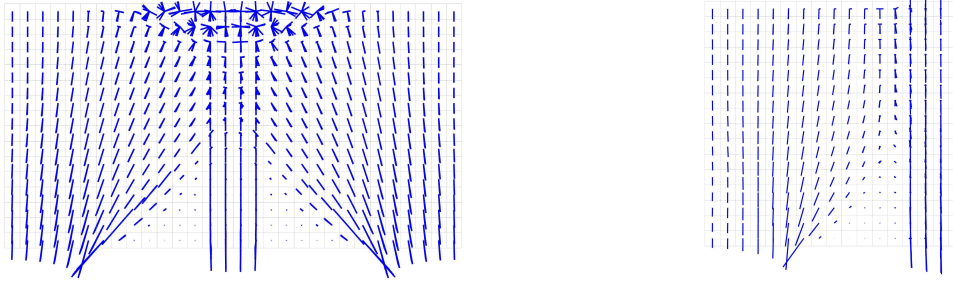


Figure 13. Example 3.4. Principal compressive stresses in case of a vertical settlement: external wall (left) and spine wall (right).

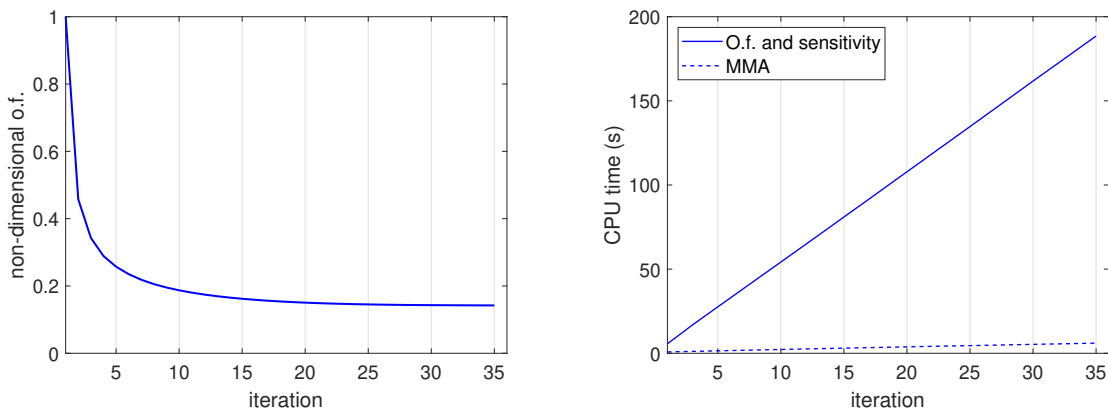


Figure 14. Example 3.4. History plot of the objective function (left) and computational cost (right). Note that o.f. stands for “objective function”.

panel is constrained except for the central region with dimension $S1 = 1$ m and $S2 = 0.625$ m, in agreement with the analytical and numerical investigations reported in [Mastrodicasa 1943]. A regular mesh of 2752 elements is used for the simulation, along with 8256 minimization unknowns. Figures 12 and 13 show a map of the principal stresses. An arch-like mechanism arises both in the external wall and in the spine wall transferring the vertical load to the safe external regions; see also Figure 13. The proposed algorithm captures a discontinuity in the stress field that allows a possible detachment in the lower part of the connection to be detected, as shown in [Mastrodicasa 1943]. The nonhomogeneous stress distribution at the base of the external wall suggests that a torsional effect, induced by the vertical settlement, arises.

Figure 14 reports the history plot of the objective function, i.e., the overall strain energy scaled by its value at the first iteration at $x_{1e} = x_{2e} = x_{3e} = 0.5$ (left), and the cumulative cost of the proposed algorithm (right), both in terms of time spent in the computation of the objective function and its derivative, and in updating the minimization unknowns through the MMA. Thirty five iterations and approximately 200 seconds are needed on a standard laptop to solve the equilibrium. Most of the time is spent in the finite element analysis (assembly and Cholesky factorization of the stiffness matrix) performed for the current set of minimization unknowns, whereas, as expected, the large scale optimizer is quite efficient.

4. Concluding remarks and future perspectives

An efficient numerical method has been presented to analyze no-tension 3D structural elements subjected to given loads, according to an energy-based nonincremental algorithm that extends a proposal formulated for 2D bodies [Bruggi 2014]. The occurrence of tensile stresses is prevented by replacing the real material by an equivalent orthotropic material that has negligible stiffness along the direction(s) of the principal tensile strain(s) in the solid. The distribution of material that minimizes the elastic strain energy stored in the body provides the solution of the no-tension equilibrium.

To speed up the computations, the preliminary implementation of the method is based on the adoption of regular meshes of 8-node hexahedral finite elements. When addressing collapse, the relevant mechanism and the load multiplier can be estimated without any a-priori hypothesis regarding the position of the “plastic hinges”. For any assigned compatible load and set of boundary conditions, the proposed approach allows the behavior of no-tension solids experiencing triaxial stress states to be investigated.

In the continuation of the work, the simplification adopted so far, according to which only regular meshes of hexahedrons are allowed, will be removed to handle structural elements of general shape, e.g., walls with openings, vaults, and domes.

When acted upon by dynamic loads, masonry constructions are characterized by a lack of energy dissipation with respect to ductile structures. As outlined in [Di Carlo et al. 2017], rocking mechanisms in piers involve only limited regions of the panels, mainly because of diagonal cracking. In principle, the energy-based approach herein proposed could be adopted to solve the steps of a transient dynamic analysis, thus detecting regions that remain ineffective during the development of the mechanism.

Finally, the possibility of defining optimal reinforcing layouts will be dealt with: the proposed formulation can be readily extended to define the distribution of optimal tension-only strengthening layers over the walls, similarly to the approach followed in [Bruggi and Taliercio 2017] for 2D bodies.

References

- [Alfano et al. 2000] G. Alfano, L. Rosati, and N. Valoroso, “A numerical strategy for finite element analysis of no-tension materials”, *Int. J. Numer. Methods Eng.* **48**:3 (2000), 317–350.
- [Ananiev 2005] S. Ananiev, “On equivalence between optimality criteria and projected gradient methods with application to topology optimization problem”, *Multibody Syst. Dyn.* **13**:1 (2005), 25–38.
- [Angelillo et al. 2010] M. Angelillo, L. Cardamone, and A. Fortunato, “A numerical model for masonry-like structures”, *J. Mech. Mater. Struct.* **5**:4 (2010), 583–615.
- [Bendsøe and Sigmund 1999] M. P. Bendsøe and O. Sigmund, “Material interpolation schemes in topology optimization”, *Arch. Appl. Mech.* **69**:9-10 (1999), 635–654.
- [Benvenuto 1991] E. Benvenuto, *An introduction to the history of structural mechanics, II: Vaulted structures and elastic systems*, Springer, 1991.
- [Berto et al. 2002] L. Berto, A. Saetta, R. Scotta, and R. Vitaliani, “An orthotropic damage model for masonry structures”, *Int. J. Numer. Methods Eng.* **2** (2002), 127–157.
- [Bruggi 2014] M. Bruggi, “Finite element analysis of no-tension structures as a topology optimization problem”, *Struct. Multidiscip. Optim.* **50**:6 (2014), 957–973.
- [Bruggi and Taliercio 2015] M. Bruggi and A. Taliercio, “Analysis of no-tension structures under monotonic loading through an energy-based method”, *Comput. Struct.* **159** (2015), 14–25.
- [Bruggi and Taliercio 2017] M. Bruggi and A. Taliercio, “Optimal strengthening of no-tension structures with externally bonded reinforcing layers or ties”, *Struct. Multidiscip. Optim.* **55**:5 (2017), 1831–1846.

- [Como 2016] M. Como, *Statics of historic masonry constructions*, Springer Series Solid Struct. Mech. **5**, Springer, 2016.
- [Cowin and Mehrabadi 1995] S. C. Cowin and M. M. Mehrabadi, “Anisotropic symmetries of linear elasticity”, *Appl. Mech. Rev. (ASME)* **48:5** (1995), 247–285.
- [Cuomo and Ventura 2000] M. Cuomo and G. Ventura, “A complementary energy formulation of no tension masonry-like solids”, *Comput. Methods Appl. Mech. Eng.* **189:1** (2000), 313–339.
- [Del Piero 1989] G. Del Piero, “Constitutive equation and compatibility of the external loads for linear elastic masonry-like materials”, *Meccanica (Milano)* **24:3** (1989), 150–162.
- [Di Carlo et al. 2017] F. Di Carlo, S. Coccia, and M. Como, “Rocking in presence of cracking of masonry wall piers”, *Key Eng. Mater.* **747** (2017), 678–685.
- [Fortunato et al. 2016] A. Fortunato, E. Babilio, M. Lippiello, A. Gesualdo, and M. Angelillo, “Limit analysis for unilateral masonry-like structures”, *Open Const. Build. Tech. J.* **10:suppl. 2:M12** (2016), 346–362.
- [Fortunato et al. 2018] A. Fortunato, F. Fabbrocino, M. Angelillo, and F. Fraternali, “Limit analysis of masonry structures with free discontinuities”, *Meccanica (Milano)* **53:7** (2018), 1793–1802.
- [Fuschi et al. 1995] P. Fuschi, G. Giambanco, and S. Rizzo, “Nonlinear finite element analysis of no-tension masonry structures”, *Meccanica (Milano)* **30:3** (1995), 233–249.
- [Heyman 1966] J. Heyman, “The stone skeleton”, *Int. J. Solids Struct.* **2:2** (1966), 249–279.
- [Lourenço 2001] P. B. Lourenço, “Analysis of historical constructions: from thrust-lines to advanced simulations”, pp. 91–116 in *Historical constructions* (Guimarães, 2001), edited by P. B. Lourenço and P. Roca, Univ. Minho, Guimarães, 2001.
- [Lourenço et al. 1997] P. B. Lourenço, R. de Borst, and J. G. Rots, “A plane stress softening plasticity model for orthotropic materials”, *Int. J. Numer. Methods Eng.* **40:21** (1997), 4033–4057.
- [Maier and Nappi 1990] G. Maier and A. Nappi, “A theory of no-tension discretized structural systems”, *Eng. Struct.* **12:4** (1990), 227–234.
- [Marfia and Sacco 2005] S. Marfia and E. Sacco, “Numerical procedure for elasto-plastic no-tension model”, *Int. J. Comput. Methods Eng. Sci. Mech.* **6:3** (2005), 187–199.
- [Mastrodicasa 1943] S. Mastrodicasa, *Dissesti statici delle strutture edilizie*, Hoepli, Milano, 1943.
- [Mehrabadi and Cowin 1990] M. M. Mehrabadi and S. C. Cowin, “Eigensensors of linear anisotropic elastic materials”, *Quart. J. Mech. Appl. Math.* **43:1** (1990), 15–41.
- [Papa and Taliercio 2005] E. Papa and A. Taliercio, “A visco-damage model for brittle materials under monotonic and sustained stresses”, *Int. J. Numer. Anal. Methods Geomech.* **29:3** (2005), 287–310.
- [Pelà et al. 2011] L. Pelà, M. Cervera, and P. Roca, “Continuum damage model for orthotropic materials: application to masonry”, *Comput. Methods Appl. Mech. Eng.* **200:9-12** (2011), 917–930.
- [Rovati and Taliercio 2003] M. Rovati and A. Taliercio, “Stationarity of the strain energy density for some classes of anisotropic solids”, *Int. J. Solids Struct.* **40:22** (2003), 6043–6075.
- [Svanberg 1987] K. Svanberg, “The method of moving asymptotes: a new method for structural optimization”, *Int. J. Numer. Methods Eng.* **24:2** (1987), 359–373.

Received 29 Apr 2018. Revised 25 Jul 2018. Accepted 3 Dec 2018.

DEBORAH BRICCOLA: deborah.briccola@polimi.it
Department of Civil and Environmental Engineering, Politecnico di Milano, Milano, Italy

MATTEO BRUGGI: matteo.bruggi@polimi.it
Department of Civil and Environmental Engineering, Politecnico di Milano, Milano, Italy

ALBERTO TALIERCIO: alberto.taliercio@polimi.it
Department of Civil and Environmental Engineering, Politecnico di Milano, Milano, Italy

CRACKING OF MASONRY ARCHES WITH GREAT DEFORMATIONS: A NEW EQUILIBRIUM APPROACH

JOSÉ IGNACIO HERNANDO GARCÍA,
FERNANDO MAGDALENA LAYOS AND ANTONIO AZNAR LÓPEZ

Masonry arches crack inexorably after decentering. This phenomenon is well known to any master builder. For small deformations these cracks do not affect the safety of the arch. Indeed, the arch with time may show different patterns of cracking, which lead to different sets of internal forces. Within the frame of modern limit analysis, developed for masonry structures, mainly by Professor Heyman since the 1960s, we know that cracking is irrelevant to safety: indeed, it is the capacity of forming cracks which gives “plasticity” to masonry. Small deformations do not distort the overall form of the arch. A direct corollary of the safe theorem states that if it is possible to draw a line of thrust within the arch, the arch will not collapse, and it is safe. This is independent of the “actual” state of the arch, manifested by a certain pattern of cracks. This pattern will change with very small (unpredictable) variations in the boundary conditions; a tiny spreading of the abutments will produce a complete change.

However, when the deformations are large, the geometry of the arch is severely distorted and we cannot study the stability with the original geometry: it is necessary to proceed step by step, considering the deformed geometry. This phenomenon has been rarely studied. However, even these studies consider, as a simplification, that the crack patterns do not vary and the movement is studied under this assumption. That this is not the case can be seen with tests with small models of arches: the position of cracks can be altered, and this may influence the validity of the study. The present contribution proposes a method of analysis which permits us to study the history of cracking until collapse. This has not only theoretical interest; it may be used in the analysis of some critical cases which occur in practice.

1. Maximum and minimum thrust of a masonry arch: linear analysis

This work is based on three hypotheses (see [Heyman 1966; 1995; 2007]) that are assumed as valid. The discussion, as well as the validation, of them is out of the scope of the present article. These assumptions are

- (1) the elements can be considered as solid rigid voussoirs because the stresses of the elements are low, despite the contact between the elements being located in a single point,
- (2) sliding failure cannot occur, and
- (3) masonry has no tensile strength.

The second assumption is based on the idea that arches are formed by a line sequence of voussoirs. Recent studies of systems that have a geometry with more complex topology are considered in [Fortunato et al.

Keywords: masonry arches, cracking, large deformations.

2018; Portioli and Cascini 2017] and with a more theoretical approach in [Fortunato et al. 2016]. The last study focuses on a single arch, while the present work has no such limitation.

The stress in the joints of the arch (contact between voussoirs) has been described as proposed by Livesley [1978]: a shear force and two axial forces are considered at each joint.

Already Méry [1840] showed the relationship between thrust lines (equilibrium solutions) and patterns of cracking, crucially identifying the typical cracks giving the maximum and minimum thrust.

With all these premises, the calculation of the minimum horizontal thrust (h) is determined by either of the two dual problems of linear programming (LP):

$$\begin{aligned} \min h &= \mathbf{c}^t \cdot \mathbf{s} \quad \text{such that } [\mathbf{H}_N \ \mathbf{H}_V] \cdot \begin{bmatrix} s_N \\ s_V \end{bmatrix} = \mathbf{f}, \quad s_N \leq 0, \quad (s_V); \\ \max W_{\text{ext}} &= \mathbf{f}^t \cdot \mathbf{u} \quad \text{such that } (\mathbf{u}), \quad \mathbf{H}_N^t \cdot \mathbf{u} \geq \mathbf{c}_N, \quad \mathbf{H}_V^t \cdot \mathbf{u} = \mathbf{c}_V. \end{aligned} \quad (1-1)$$

Here, as is usual, \mathbf{f} represents the system forces vector, \mathbf{H} is the equilibrium matrix, and \mathbf{s} is the internal forces vector. In the dual kinematic formulation, \mathbf{H}^t is the compatibility matrix and \mathbf{u} is the movement vector. The unrestricted variables are shown in brackets for the sole purpose of underlining the symmetry between the primary static problem and the dual kinematics. Indices N and V refer to the axial and shear forces, respectively. The internal force vector \mathbf{s} has been reordered as $\mathbf{s}^t = [s_N \ s_V]$ to clarify the constraints placed on each variable. The equilibrium matrix \mathbf{H} and the \mathbf{c} vector were reordered in the same way. Although it is unnecessary for the purposes of this paper, a more detailed version of the problem restrictions may be consulted in [Magdalena Layos 2013; Fishwick 1996]. An analysis of the effect of settlements in general plane masonry structures can be found in [Iannuzzo et al. 2018].

When the dummy variables are incorporated into $\mathbf{e} = \mathbf{H}^t \cdot \mathbf{u}$, one can write

$$\begin{bmatrix} \mathbf{H}_N^t \\ \mathbf{H}_V^t \end{bmatrix} \mathbf{u} = \begin{bmatrix} \mathbf{e}_N \\ \mathbf{e}_V \end{bmatrix}; \quad \mathbf{e}_N \geq \mathbf{c}_N, \quad \mathbf{e}_V = \mathbf{c}_V. \quad (1-2)$$

In order to obtain the minimum (maximum) horizontal force of the arch, the objective function of the problem is

$$h = \pm(N_i + N_j) \cos \alpha \pm V_{i,j} \sin \alpha. \quad (1-3)$$

Here the subscripts i, j refer to the vertices defining the first and last contact points of the joint of the arch, α corresponds to the angle between the plane of the joint and the horizontal line, the sign \pm depends on the support — left or right — of the arch and on the criterion of the sign that has been adopted. The constraint of the kinematic equations $c_{N,i} \geq \cos \alpha$; $c_{N,j} \geq \cos \alpha$; $c_{V,ij} = \sin \alpha$ has a clear physical interpretation: the movement (horizontal) of the support of the arch has a parallel component $u_V = \cos(\alpha)$ and a perpendicular one $u_N = \sin(\alpha)$, both of them referenced to the local axis of the joint. If sliding failure cannot occur, the first component corresponds to the deformation e_V and the second one must be lower or equal to each strain e_N . Note that moreover the virtual mechanism is normalized in the kinematic formulation so that horizontal arch end movement is 1. To this end, it is supposed that the movements are sufficiently small to make this approximation possible (rigorously, the initial velocities instead of the movements should be considered, thus several references show the notation $\dot{\mathbf{u}}$).

For the recommended normalization of the vector \mathbf{u} and using the virtual work principle (VWP), it is clear that the objective function of the kinematic problem $W_{\text{ext}} = \mathbf{f}^t \cdot \mathbf{u}$ coincides with minimum thrust, as the work of the internal forces will be reduced to $W_{\text{int}} = 1 \cdot h$.

It is also clear that if vector \mathbf{c} is multiplied by a factor γ_u , the $\mathbf{u}_\gamma = \gamma_u \mathbf{u}$ vector is the solution to the new kinematic problem and the value of the target function will be $W_{\text{ext},\gamma} = \gamma_u W_{\text{ext}}$. Using the VWP again the conclusion is that

$$W_{\text{int},\gamma} = W_{\text{ext},\gamma} \rightarrow \gamma_u (1 \cdot h) = \gamma_u W_{\text{ext}} \rightarrow h = W_{\text{ext}}, \quad (1-4)$$

i.e., that the thrust value of the arch does not vary.

Regarding the static problem scale, it is only necessary to modify the objective function $h_\gamma = \gamma_u \mathbf{c}^t \cdot \mathbf{s}$. If \mathbf{s} is the solution of the first problem, the solution of the scaled problem corresponds to this same solution multiplied by the γ_u factor.

2. Maximum and minimum thrust of a masonry arch: nonlinear analysis

Restricting to small displacements, in the limit infinitesimal, the angle of aperture of the joints θ is small too. When two voussoirs open, a hinge is formed. Therefore we can approximate the value of $\sin \theta$ to θ and $\cos \theta$ to 1. In this way, the previous formulation reduces to the linear formulation:

$$\begin{aligned} \text{(linear)} \quad \max W_{\text{ext}} &= \mathbf{f}^t \cdot \mathbf{u} \quad \text{such that } \mathbf{H}_N^t \cdot \mathbf{u} \geq \mathbf{c}_N, \quad \mathbf{H}_V^t \cdot \mathbf{u} = \mathbf{c}_V \\ \text{(nonlinear)} \quad \max W_{\text{ext}} &= \mathbf{f}^t \cdot \mathbf{u} \quad \text{such that } \mathbf{H}(\mathbf{u})_N^t \geq \mathbf{c}_N, \quad \mathbf{H}(\mathbf{u})_V^t = \mathbf{c}_V. \end{aligned} \quad (2-1)$$

If the study is focused on noninfinitesimal movements, the change of variable $s = \sin \theta$, $c = \cos \theta$ can be applied and the function $\mathbf{H}(\mathbf{u})$ remains a linear function of c and s . However, the quadratic constraints $c^2 + s^2 = 1$ must be added as a condition to (2-1), introducing the first nonlinearity into the problem.

On the other hand, the progression of the initial small movement may produce the opening and closing of different joints of the arch. Due to this effect, the objective function experiences abrupt and instantaneous jumps. These jumps of the objective functions are due to the fact that both surfaces of each joint may continue to be in contact or not, as well as whether stress can be transmitted or not. This mechanical behavior can be characterized as a disjunctive (nonsmooth) behavior, and can be mathematically formulated through complementary constraints using bilinear functions or other equations having an equivalent complexity [Hu et al. 2012].

When both types of constrains are applied, the problem becomes NP-hard, with high computational complexity. Problems of this type may have multiple solutions, and this hinders their resolution by deterministic methods. In this case, the multiple possible solutions correspond to the different combinations of positions of the open joints that fulfill the restrictions. This occurs even if the simplification concerning the elimination of the dynamic stress is incorporated.

3. Incremental algorithm

In spite of the difficulties due to the nonlinearity of the problem, there exist different options for a possible solution (see [Gilbert and Melbourne 1994; Huerta and López 1997; Portioli and Cascini 2017]). The problem can be incrementally solved by superimposing a sequence of linear problems. At each step, when the initial problem is solved, the geometry of the arch is modified according to the solution obtained and

the process is repeated again. If γ_u , that is, the step amplitude of the displacement, is small enough then the accumulated errors remain small too. These errors, due to the linear approximation at each step, accumulate, and produce a aberration of the elements of the arch, elements that were initially considered as rigid blocks. The amplitude of such an aberration depends obviously on the value of γ_u that is used during the iteration.

These algorithms have two important disadvantages:

- (1) They give only a single solution among all the possible solutions.
- (2) Small variations of the initial geometry of the arch at each step can lead to important variations in the final solution.

These effects are a direct consequence of the circumstances described at the end of the Section 2, and they can be observed in some of the results shown below.

When the linear approximation is used it is assumed that $\mathbf{e} = \mathbf{H}^t \mathbf{u}$, and in the cases in which the movements are not small, $\mathbf{e}_{NL} = \mathbf{H}^t(\mathbf{u})$ should be used instead. To solve the nonlinear problem is a rather difficult task, but when a specific \mathbf{u} is obtained (for example, by solving the linear problem) calculating \mathbf{e}_{NL} is simple: By introducing $\mathbf{e}_r^{(t-1)} = \mathbf{e}_{NL}^{(t-1)} - \mathbf{e}_L^{(t-1)}$, where the subscript r is defined as a “residue”, then $\mathbf{e}_{NL}^{(t)} \approx \mathbf{e}_L^{(t)} + \mathbf{e}_r^{(t-1)}$. If the subscripts are omitted, one can write $\mathbf{e} \approx \mathbf{e}_L + \mathbf{e}_r^{(t-1)}$; $\mathbf{e} \approx \mathbf{H}^t \mathbf{u} + \mathbf{e}_r^{(t-1)}$.

With this correction of the \mathbf{e} vector, the linear problem at each step is solved:

$$\max W_{\text{ext}} = \mathbf{f}^t \cdot \mathbf{u} \quad \text{such that } \mathbf{e}_N \geq \mathbf{c}_N, \mathbf{e}_V = \mathbf{c}_v, \begin{bmatrix} \mathbf{e}_N \\ \mathbf{e}_V \end{bmatrix} = \begin{bmatrix} \mathbf{H}_N^t \\ \mathbf{H}_V^t \end{bmatrix} \mathbf{u} + \begin{bmatrix} \mathbf{e}_{r,N}^{(t-1)} \\ \mathbf{e}_{r,V}^{(t-1)} \end{bmatrix}, \quad (3-1)$$

or the other option

$$\max W_{\text{ext}} = \mathbf{f}^t \cdot \mathbf{u} \quad \text{such that } \mathbf{H}_N^t \cdot \mathbf{u} \geq \mathbf{c}_N - \mathbf{e}_{r,N}^{(t-1)}, \mathbf{H}_V^t \cdot \mathbf{u} = \mathbf{c}_V - \mathbf{e}_{r,V}^{(t-1)}. \quad (3-2)$$

Note that if $\mathbf{e}_r^{(t)} = \mathbf{e}_r^{(t-1)}$ at the iteration t , then $\mathbf{e}_{NL}^{(t)} = \mathbf{e}_L^{(t)} + \mathbf{e}_r^{(t-1)}$ and the constraint of the kinematic problem can be written as

$$\begin{bmatrix} \mathbf{H}_N^t(\mathbf{u}) \\ \mathbf{H}_V^t(\mathbf{u}) \end{bmatrix} = \begin{bmatrix} \mathbf{e}_{NL,N} \\ \mathbf{e}_{NL,V} \end{bmatrix}; \quad \mathbf{e}_{NL,N} \geq \mathbf{c}_N, \mathbf{e}_{NL,V} = \mathbf{c}_v. \quad (3-3)$$

In this way, the nonlinear equations $\mathbf{H}(\mathbf{u})^t = \mathbf{e}_{NL}$ are verified, as are the restriction constraints of the arch support.

When the iteration has been corrected, and always before calculating the next step, the equilibrium of the new geometry is checked. For that reason, a linear “kinematic” problem is solved by minimizing $\mathbf{f}^t \mathbf{u}$ using the new geometry with the constraint that the joints that have been opened cannot be closed. If the new geometry is equilibrated, then $\mathbf{f}^t \mathbf{u}$ must vanish. If it does not happen, it must be because the system becomes a mechanism, and a new equilibrated position could be found if any joint closes. In these cases, often another joint opens, and it is in this way that the positions of the hinges of the arch change.

The linear problem solved in this step is similar to (1-1): it is needed only to modify \mathbf{c}_N . The nonzero components correspond to the deformation of the hinges. Then, a simple interpretation of the static dual problem can be extracted: The function of the static problem is a linear combination of the axial forces

applied to the vertices of the opened joints. If the equilibrium of the arch remains with hinges, the sum of these axial forces must be null. In another case, some of these axial forces must not be zero in order to enable the equilibrium. This same “incremental” process is applied to solve the new problem.

4. Results

Figure 1 shows the study of the effect of a given displacement of the left support of a semicircular arch composed of twelve voussoirs. The ratio between the interior and exterior radius is 5 : 8. The external load applied to this model is zero, and only the weight of the arch has been considered.

Section 1 shows the classic problem of analyzing the effect of horizontal creep of an arch support and its dual problem (maximum/minimum thrust). It is obvious that to formulate the problem of the descent/ascent of one of the supports of the same arch (and its dual minimum/maximum vertical reaction), it is enough to substitute α (the angle between the plane of the joint and the horizontal line) by its complementary value in the target function definition (1-3).

In Figure 1 the abscissa represents the normalized displacements of the support of the arch, v_z/D (D being the interior diameter of the arch) and \bar{v}_z has been defined as $\bar{v}_z = 10v_z/D$. In Figure 1,

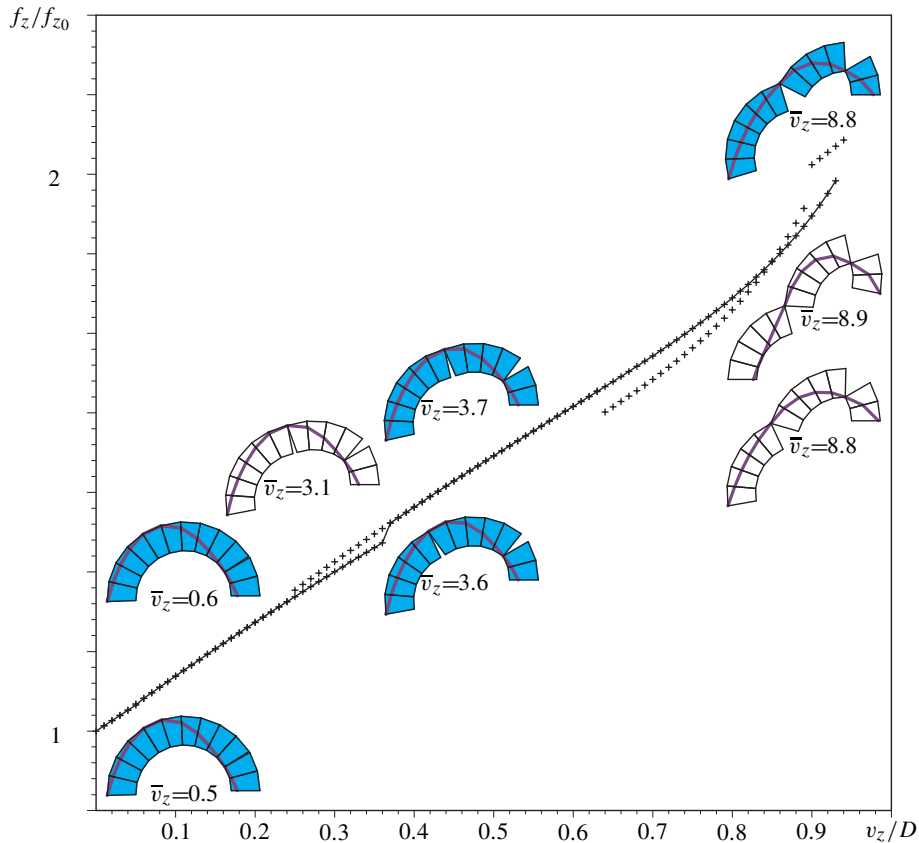


Figure 1. Variation of the vertical reaction in the left support f_z/f_{z0} depending on the relative displacement v_z/D of the arch ($\bar{v}_z = 10v_z/D$).

the ordinate axis represents the normalized value of the vertical reaction force $f_z/f_{z,0}$, where $f_{z,0}$ is the minimum vertical reaction force calculated at the support of the arch in the initial geometry (nondeformed arch). The continuous line represented in Figure 1 has been built by applying a progressive increment in the vertical movement of the left support of the arch, and the resultant curve is similar to the curves found in [Ochsendorf 2006], in which the horizontal force of the arch is related to the horizontal displacement. In both cases, the reaction force increases when the movement advances. In this way, this movement would not stop due to the steps of Figure 1 as they have been obtained using the minimum reaction force from which the movement begins. In real masonry structures, movements like these should be due to a settlement of the foundation. In these cases, the soil would behave more or less elastic and this behavior would stop the movement of the arch unless the foundation collapses. This last consideration is difficult to justify when the horizontal movement is due to other external effects, for example, when the consequence is due to the effect of a wall, when the arch is built against a massive buttresses, etc., [Ochsendorf 2006].

The graph of Figure 1 is discontinuous, unlike the results that can be found in [Ochsendorf 2006]. This discontinuity appears at $\bar{v}_z \approx 3.7$ and $\bar{v}_z \approx 0.5$. In this last case it is more difficult to appreciate it due to the scale of the graph. Both these discontinuities correspond to steps at which the position of the hinges changes. Thus, when $\bar{v}_z = 3.6$ the sixth joint opens (between the fifth and sixth voussoirs) while when $\bar{v}_z = 3.7$ the hinge is located between the sixth and seventh voussoirs. These results are coherent with Section 2, where the nonlinearity of the problem is exposed.

In Figure 1, the geometry of the arch has been represented. In this way, the deformation at different steps of the process can be clearly observed. As can be observed, the steps corresponding to $\bar{v}_z = 0.5, 0.6, 3.6, 3.7, 8.8$ have been colored and the thrust lines have been incorporated. It can be observed that the equilibrium of the step with $\bar{v}_z = 3.6$ is tight, because the thrust line is almost tangent to the external surface of the arch near the sixth voussoir. From this step, when the position of the hinge changes, when $\bar{v}_z = 3.7$, it can be observed that the equilibrium of the arch improves.

Between the steps in which $\bar{v}_z = 0.5$ and $\bar{v}_z = 0.6$ the position of the hinge changes from the fourth-fifth voussoirs to the fifth-sixth ones. The position of the hinge when $\bar{v}_z \leq 0.5$ corresponds to the results using classic linear analysis.

From $\bar{v}_z = 3.7$ to the last step, in which the solution is located at $\bar{v}_z = 9.2$, the position of the hinges does not vary. One deformed arch in this family of results has been drawn ($\bar{v}_z = 8.8$, colored arch). If this state is compared to $\bar{v}_z = 3.7$, it can be seen that when the vertical displacement in the left support increases, the thrust lines tend to approach the right of the arch. It is easy to find the step in which collapse occurs: when the thrust line is located on the far right of the right support it is not possible to find equilibrated positions.

Additionally, the graph in Figure 1 shows the results when the direction of the movement of the right support changes from $\bar{v}_z = 3.7$ (the dashed line between $\bar{v}_z = 3.6$ and $\bar{v}_z = 2.5$). If a new analysis is performed from $\bar{v}_z = 3.7$ in order to calculate the state with lower vertical displacement of the support ($\bar{v}_z = 3.6, \bar{v}_z = 3.5$, etc.), a new solution is obtained that is different from the previous one (when the displacement of the support was gradually increasing). It is important to note that the position of the joints in these new solutions do not vary from the position of the state $\bar{v}_z = 3.7$. As expected in Section 2, this problem has no unique solution. One of these new solutions is represented ($\bar{v}_z = 3.1$, without color

arch). When $\bar{v}_z < 2.5$, the joint located between the sixth and seventh voussoirs returns to its original position.

Due to the similarity between both solutions (2.5, 3.6) it can be assumed that the first or second solution may be obtained indistinctly. Any small imperfection or minor perturbation could cause the change from one step to another.

In Figure 1 another second family of solutions has been shown using a dashed line. From step $\bar{v}_z = 6.4$ to $\bar{v}_z = 8.8$, solutions appear once again in which the hinges are located between the fifth and sixth voussoirs. This location continues during the entire interval (although \bar{v}_z may increase or decrease the position of the hinges).

This occurs until the value decreases to $\bar{v}_z = 6.4$. It is in this step when the arch geometry is modified and the location of the hinge varies by closing the seventh joint and opening the sixth. In the following steps, the solution obtained matches the original ones (represented by the continuous line), independently of the increase or decrease in \bar{v}_z . From this point, it is necessary to add a new perturbation into the algorithm in order to obtain the same results again. An example of such a perturbation could be to include the prevention of the aperture in the seventh joint so that the joint can not be opened. One of the deformed arches in this family of results has been drawn, $\bar{v}_z = 8.8$ (without color). It can be observed that this step corresponds to the last one, because the thrust line reaches the right of the right support. This step is similar to the one previously described (when $\bar{v}_z = 8.8$ and the arch is colored). However, in this new point the arch has not yet collapsed. The vertical displacement can increase to $\bar{v}_z = 8.8$, further opening the right hinge and slightly closing the left one ($\bar{v}_z = 8.9$, without color arch).

These results cannot be generalized, nor can it be confirmed that the position of the hinges changes when vertical displacement increases.

Figure 2 shows the analysis of the same arch when the number of voussoirs varies. The left graph corresponds to an arch with ten voussoirs, and it can be seen that the position of the hinges does not vary until movements approach arch collapse. In this case, the location of the hinges does not depend on \bar{v}_z . During the last steps, when the location of the hinge varies, $\bar{v}_z = 8.1$, the left hinge closes while on contrary the right hinge opens. This effect was previously observed in analysis of the twelve voussoir arch. In this graph, different steps of the deformed arch have been represented ($\bar{v}_z = 0.1, 0.5, 8.0, 8.1$) and the main solution of Figure 1 has been included with a dashed line. The step when $\bar{v}_z = 8.1$ has been shown over the immediately previous step (without color). In this way the sharp variation between both steps can be observed.

Figure 2 (right) shows the results of analysis of the arch composed of thirteen voussoirs. The solution obtained is similar to the one shown previously in Figure 1. It can be observed that in this case, when the deformation of the left support of the arch increases, the hinge changes twice: when $\bar{v}_z = 2.1$ and when $\bar{v}_z = 5.4$. From this step, if the direction of the displacement is inverted, two different families of solutions are obtained. Both solutions are similar to the one previously obtained in the first arch when $2.5 < \bar{v}_z < 3.6$. Similar solutions to the steps where $\bar{v}_z > 6.4$ in the twelve voussoir arch have not been obtained. However, it is not possible to state that they do not exist. It must be noted that in spite of incorporating the same perturbations in the algorithm, a different solution was obtained. Again, the main solution of Figure 1 has been included with a dashed line so that both results can be compared.

Figure 3 shows the results of the same analysis in the arch with seven (left) and twenty (right) voussoirs. When the number of voussoirs increases — Figure 3 (right) — the discontinuities of the function $f_z =$

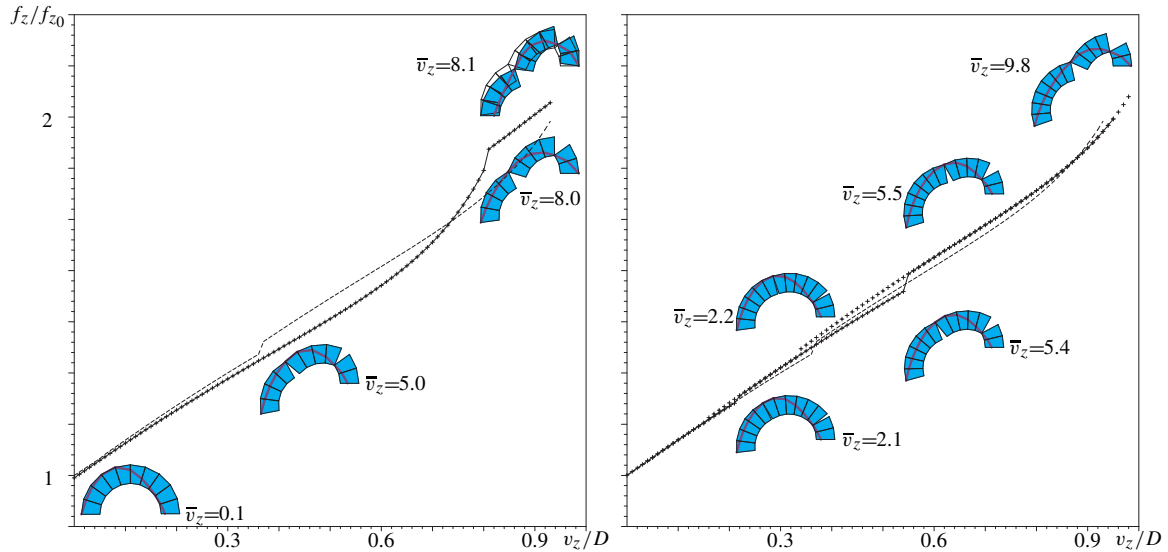


Figure 2. Variation of the vertical reaction in the left support f_z/f_{z_0} depending on the relative displacement \bar{v}_z/D of the arch composed of 10 voussoirs (left) and 13 (right) ($\bar{v}_z = 10v_z/D$).

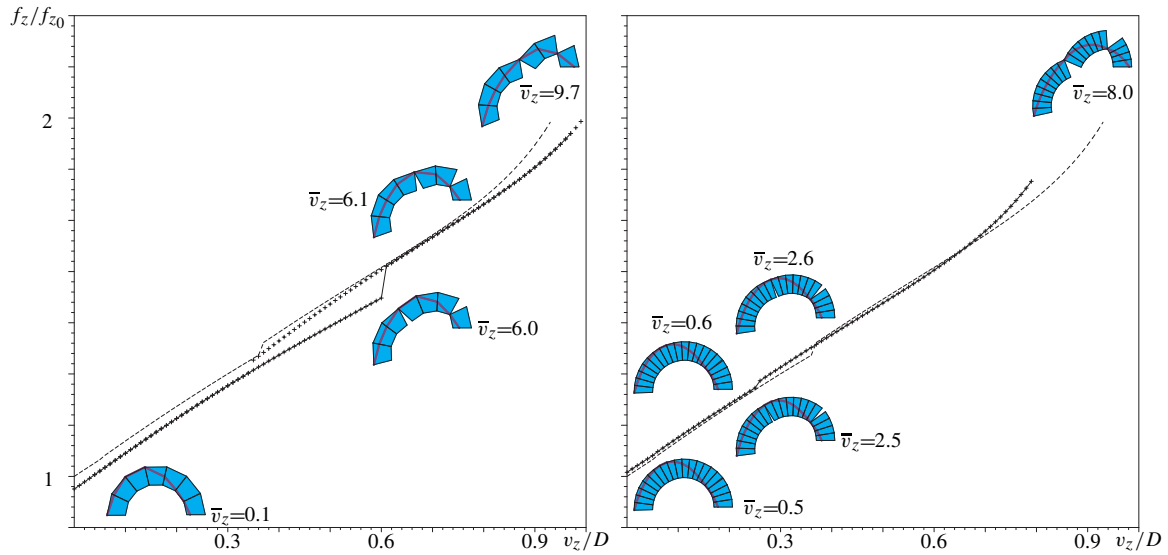


Figure 3. Variation of the vertical reaction in the left support f_z/f_{z_0} depending on the relative displacement \bar{v}_z/D of the arch composed of seven voussoirs (left) and twenty voussoirs (right) ($\bar{v}_z = 10v_z/D$).

$f_z(\bar{v}_z)$ are attenuated. On the other hand, when the number of voussoirs decreases, the effect of the discontinuities increases; see Figure 3 (left). It can be concluded that the decrease of the number of voussoirs increasingly differs from the effect described in [Ochsendorf 2006].

It can be seen that the arch composed of seven voussoirs has a wide range in which two different states

can occur with the same \bar{v}_z value. The second hinge can be located between the third and fourth or fourth and fifth voussoirs. Unlike the results obtained in the twelve voussoir arch, Figure 3 (left) shows that unless a significant perturbation occurs it is not viable to transition from the two states ($3.8 < \bar{v}_z < 6.0$).

Although this work presents the results of an arch with a 5 : 8 ratio between its internal and external radii, a previous parametric study carried out in arches showed this ratio varied from 5 : 6 to 5 : 10. The geometry of the arch studied here corresponds to the proportion which shows the highest hinge variability. For example, in a slender arch with a ratio of 5 : 6, these effects are insignificant. Only in models with a high number of voussoirs may some of the hinges vary. It has been shown that in these cases the effect of the variation in the position of the hinges is reduced; see Figure 3 (right). In this slender arch case the solution obtained is unique. Even when a perturbation was included in the algorithm, no variation in the solution arose.

This previous study also explains why this work focuses on the vertical displacement of one of the arch supports. This study shows that the effect of horizontal displacement variation has a minimum influence on the variation of the position of the hinges. When horizontal displacements were applied, only in exceptional cases does an abrupt change in the position of the hinges occur. This effect does not imply that the solution must be unique. In these cases it is simple to obtain alternative solutions. For example, when an arch with an odd number of voussoirs is studied, two different solutions can be obtained depending on whether the hinge is located on one side or the other of the central voussoirs. Although every solution becomes stable (within a certain margin) it is necessary to include perturbations in the algorithm to move from one state to other.

5. Conclusions

The results obtained in this work show the possibility that the position of the opened joints changes along the arch, when the displacement imposed at the support of the arch is modified.

This change of the position of the opened joints spontaneously occurs when the movement of one support gradually increases or decreases. However, when the direction of the movement changes, the abrupt deformation of the arch does not occur at the same point.

Unlike [Ochsendorf 2006], the case studies presented in the present article exhibit multiple solutions. The change from one solution to another can occur when the movement of one support of the arch increases or decreases, but also can occur due to an external perturbation. This phenomenon is shown in the arch of twelve voussoirs studied in Section 4.

The results obtained in this work are specific to the shape (semicircular arch) and slenderness ratio (5 : 8) chosen, and can be hardly generalized. The study of the effect of form and slenderness ratio on the outcome of the progressive settlements deserve further study. The results here presented show a great diversity of qualitative responses that make difficult the possibility of a simple classification.

Currently, also with the aim of seeing if this classification can be done, the present method of calculation offers the possibility to analyze different particular cases of form and slenderness.

Finally, the nonlinear effects observed in the cases studied in this work occur when the movements resultant are definitely large compared to the overall dimensions of the structure. Thus, the solutions obtained with linear formulations, the classic formulation for small movements, is accurate enough for small displacements.

References

- [Fishwick 1996] R. J. Fishwick, *Limit analysis of rigid block structures*, Ph.D. thesis, University of Portsmouth, 1996.
- [Fortunato et al. 2016] A. Fortunato, E. Babilio, M. Lippiello, A. Gesualdo, and M. Angelillo, “Limit analysis for unilateral masonry-like structures”, *Open Constr. Build. Tech. J.* **10**:suppl. 2:M12 (2016), 346–362.
- [Fortunato et al. 2018] A. Fortunato, F. Fabbrocino, M. Angelillo, and F. Fraternali, “Limit analysis of masonry structures with free discontinuities”, *Meccanica (Milano)* **53**:7 (2018), 1793–1802.
- [Gilbert and Melbourne 1994] M. Gilbert and C. Melbourne, “Rigid-block analysis of masonry structures”, *Struct. Eng.* **72**:21 (1994), 356–361.
- [Heyman 1966] J. Heyman, “The stone skeleton”, *Int. J. Solids Struct.* **2**:2 (1966), 249–279.
- [Heyman 1995] J. Heyman, *The stone skeleton: structural engineering of masonry architecture*, Cambridge Univ. Press, 1995.
- [Heyman 2007] J. Heyman, “The plasticity of unreinforced concrete”, pp. 157–162 in *Morley symposium on concrete plasticity and its application* (Cambridge, 2007), edited by C. Burgoyne et al., Cambridge Univ. Press, 2007.
- [Hu et al. 2012] J. Hu, J. E. Mitchell, J.-S. Pang, and B. Yu, “On linear programs with linear complementarity constraints”, *J. Global Optim.* **53**:1 (2012), 29–51.
- [Huerta and López 1997] S. Huerta and G. López, “Stability and consolidation of an ashlar barrel vault with great deformations: the church of Guimarei”, pp. 587–596 in *Structural studies, repairs and maintenance of historical buildings*, edited by C. A. Brebbia and S. Sánchez-Beitia, WIT Trans. Built Environment **26**, WIT Press, Southampton, 1997.
- [Iannuzzo et al. 2018] A. Iannuzzo, M. Angelillo, E. De Chiara, F. De Guglielmo, F. De Serio, F. Ribera, and A. Gesualdo, “Modelling the cracks produced by settlements in masonry structures”, *Meccanica (Milano)* **53**:7 (2018), 1857–1873.
- [Livesley 1978] R. K. Livesley, “Limit analysis of structures formed from rigid blocks”, *Int. J. Numer. Methods Eng.* **12**:12 (1978), 1853–1871.
- [Magdalena Layos 2013] F. Magdalena Layos, *El problema del rozamiento en el análisis de estructuras de fábrica mediante modelos de sólidos rígidos*, Ph.D. thesis, Universidad Politécnica de Madrid, 2013, <https://tinyurl.com/fmlphd>.
- [Méry 1840] E. Méry, “Mémoire sur l’équilibre des voûtes en berceau”, *Annales des Ponts et Chaussées* **19** (1840), 50–70, plates 183–184.
- [Ochsendorf 2006] J. A. Ochsendorf, “The masonry arch on spreading supports”, *Struct. Eng.* **84**:2 (2006), 29–36.
- [Portioli and Cascini 2017] F. Portioli and L. Cascini, “Large displacement analysis of dry-jointed masonry structures subjected to settlements using rigid block modelling”, *Eng. Struct.* **148** (2017), 485–496.

Received 30 Apr 2018. Revised 3 Dec 2018. Accepted 9 Dec 2018.

JOSÉ IGNACIO HERNANDO GARCÍA: joseignacio.hernando@upm.es

Department of Building Structures and Physics, Universidad Politécnica de Madrid, Madrid School of Architecture (ETSAM, UPM), Madrid, Spain

FERNANDO MAGDALENA LAYOS: fernando.magdalena@upm.es

Department of Building Construction, Universidad Politécnica de Madrid, Madrid School of Building Engineering (ETSEM, UPM), Madrid, Spain

ANTONIO AZNAR LÓPEZ: antonio.aznar@upm.es

Department of Building Structures and Physics, Universidad Politécnica de Madrid, Madrid School of Architecture (ETSAM, UPM), Madrid, Spain

RESISTANCE OF FLAT VAULTS TAKING THEIR STEREOTOMY INTO ACCOUNT

MATHIAS FANTIN, THIERRY CIBLAC AND MAURIZIO BROCATO

We study the structural performance of flat vaults, depending on the patterns of voussoirs. For this purpose, we propose three archetypes, derived from the 18th–19th century literature on stereotomy, with fit simplifications.

The ultimate structural answer of these models are evaluated, searching numerically for statically admissible loading conditions by means of an enhanced version of the thrust network analysis, assuming failure occurring by joints' opening, crushing or sliding, while voussoirs remain rigid.

The considered enhancements allow one to better capture the contact forces acting on the joints and to define consistently the safety factor of the structure. They are based on the introduction of additional partial branches in the thrust network that represent actions internal to the voussoirs and are essential to describe, at least in some cases, their rotational equilibrium, which is neglected by the standard analyses.

The three examples are compared by superposing their domains of statically admissible loadings, represented in terms of vertical uniformly distributed load vs. thrust. Our findings support but partly some of the conjectures presented in the 18th century and later literature, especially because of a plate effect that can be observed at the corners of these structures. They also allow us to classify flat vaults according to the local shape of the force network, as elliptical, parabolic or hyperbolic, thus opening to a new interpretation of their nature.

1. Introduction

A flat vault is a structural system, spanning horizontally with a reduced thickness, that withstands mainly vertical loads, normally its own weight plus additional dead and living loads, discharging them at its boundary by means of a vault effect, i.e., with a horizontal thrust. Flatness of the intrados is what characterises these structures with respect to standard (curved) vaults.

The vault effect we refer to is related to the fragmentation of the vault into voussoirs, with the joints having milder mechanical properties than the stones. Stereotomy is thus a paramount feature of these systems and our purpose here is to understand its role. Systems reaching supports in one piece, as monolithes, or stone-coffered ceilings whose span is covered by stone slabs, are not studied here.

Three bondings of flat vaults will be considered here, derived from historical examples presented in Section 2, with parameters set in Section 3, and their statically admissible ultimate structural performances compared by means of an enhanced version of the thrust network analysis.

The thrust network analysis [O'Dwyer 1999; Block and Ochsendorf 2007] has been applied to produce form finding tools [van Swinderen and Coenders 2009; Rippmann et al. 2012], and several advances and extensions have been published concerning the optimisation procedures [Vouga et al. 2012; Block and

Keywords: vaults, stereotomy, limit analysis, thrust network analysis.

Lachauer 2014b] and the related variational formulations [Fraternali 2010; de Goes et al. 2013] that can be set up to define the parameters left otherwise undefined by the equilibrium equations. It has also been applied to some historical structures on gothic fan vaults [Block and Ochsendorf 2008], rose-windows, and thin-shelled spiral staircases [Block 2009; Block and Lachauer 2014a].

Flat vaults, as flat arches, are not distinguishable from each other by their form. Per se their strength depends on the pattern in which voussoirs are cut and laid. Hence the need arises for an analytical tool capable of gaining an insight into the vault's masonry bonding.

With this need in mind, the method proposed in Section 4 is based on a more-detailed-than-usual translation of the information on the structure into the arena where forces and strengths contend. While in the standard thrust network analysis voussoirs are related to mass-points (being the nodes of a network whose branches represent, but roughly, the connections between first neighbours), a refinement of this network is made here, subdividing voussoirs in such a way that the branches of the network are a more accurate representation of the forces exchanged across joints. This refinement has been already presented in [Ciblac and Fantin 2015; Fantin and Ciblac 2016; Fantin 2017] and is applied here to the cases at issue.

The numerical implementation of the method is briefly presented in Section 5 and the results are given in Section 6. It appears that the proposed refinement allows us to define more statically admissible states than the standard thrust network analysis does. Thanks to this result, the differences among the limit static interactions in the three studied cases can be displayed and discussed.

2. A historical survey on the stereotomy of flat vaults

Many options were available in the past for the stereotomy of flat vaults and technology opens even more today, but a taxonomy is needed for our purposes. A grouping proposed by Rondelet [1804] is handy, where cutting patterns are named with respect to their analogous in curved vaults, namely (see Figure 1, from left to right):

- (1) barrel vaults (*voûte en berceau* in [Rondelet 1804]);
- (2) pavillon vault (*voûte en arc de cloître*);
- (3) spherical vault (*coupole*);
- (4) groin vault (*voûte d'arêtes*).

Various examples of such flat vaults were built in France during the 16th, 17th, and 18th centuries [Pérouse de Montclos 1982], and many exist in other countries and from different ages (see [López Mozo 2003]).

The cases covered by this nomenclature share a common trait: loads decrease “monotonically” toward the boundary. The adverb can be qualitatively explained as follows: observing any voussoir, the sheaf of vertical planes cutting it through its centre contains one element across which shear forces are exchanged whose absolute value is minimal, the plane orthogonal to it in the same sheaf bearing the maximum absolute shear. When the minimal-valued shear is null, it is possible to sever all voussoirs along the then unique nonsheared plane, without changing the load descent.

If the pattern drawn by the intersection of the planes of maximum absolute shear with the plane of the vault is made of parallel lines, then the flat vault can be called unidirectional or parabolic (i.e., inheriting the properties of a barrel vault), as it is the case of item (1). Loading is discharged in one

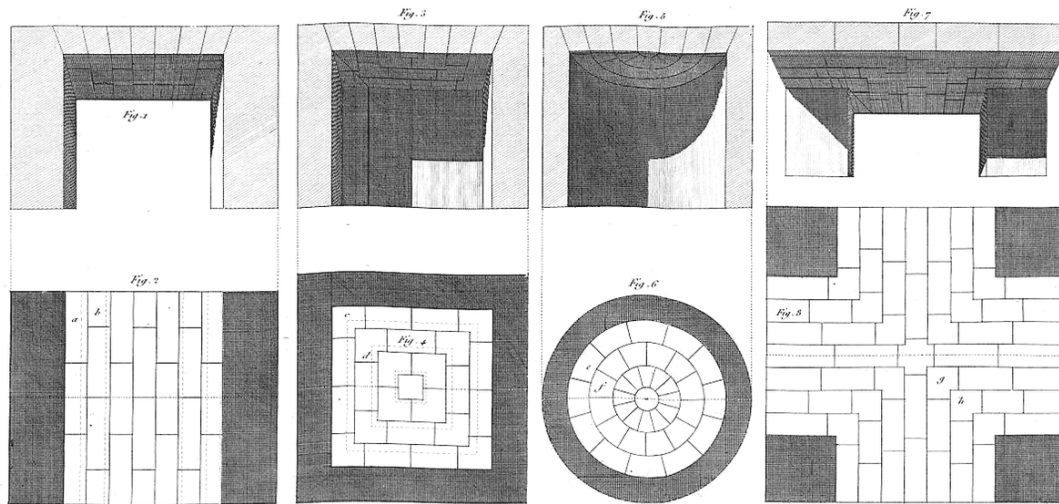


Figure 1. Flat vaults cutting pattern from [Rondelet 1804, Pl.XXXI; 1828, Pl.XXX].

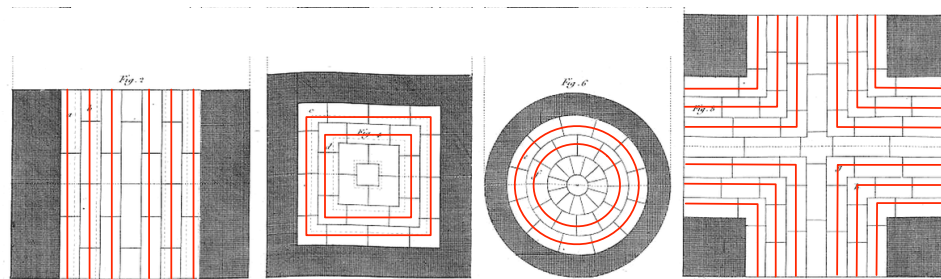


Figure 2. Patterns drawn by the maximum shear planes on the vaults of Figure 1: parallel lines correspond to a unidirectional or parabolic flat vault, concentric lines to a bidirectional or elliptical one.

direction (orthogonal to those lines) from one support to the other on two opposite sides of the vault, which necessarily covers a quadrilateral (possibly rectangular) surface, with nothing supporting the vault along the two other sides.

Otherwise, as concentric figures are found, one faces case (2) (concentric squares), (3) (circles), or (4) (cross-shaped figures). The vault can then be called bidirectional or elliptical (see Figure 2).

A third case can be considered, not in that list, with vaults that can be called hyperbolic: the above mentioned nonsheared plane is not unique, as two orthogonal planes partake of the same property at each voussoir. This dyad defines four quarters; two crossed by planes bearing positive shear forces, among which a plane of maximum shear exists, and two crossed by negative sheared planes, with one carrying a minimal shear.

These statements, presently calling upon intuition, will be made precise thanks to some of the developments presented herein. Three examples will be studied, representing the families of parabolic, elliptical, and hyperbolic flat vaults:

- (1) a “barrel” flat vault, akin to the first example on the left of Figure 1;
- (2) a “pavillon” flat vault, akin to the second example from the left in the same figure;
- (3) an “Abeille” flat vault.

Abeille’s flat vaults are so named today after their inventor, Joseph Abeille, who lived in 18th century France. Though we have a first hint of their invention in [de Bélidor 1729]¹, we owe the earliest evidence of their geometry to Gallon [1735].

The vaults patented by Abeille in 1699 were, unlike any other existing example, made of one single type of voussoir: a trapezohedron, cut in such a way that the lower face is a rectangle, the upper a square, and the two central sections obtained through planes normal to the sides of the square are isosceles trapezia, one upside down with respect to the other. Thanks to this design, when voussoirs are properly assembled, the intrados form a continuous ceiling and the extrados form a floor with pyramidal gaps.

What makes Abeille’s vaults the paradigm of a whole family of new structures is their interlocking stereotomy. In the assembly, each voussoir has four first neighbours: two of them, at opposite sides in one direction, prevent it from moving downward, the other two from moving upward. Hence, when loaded, each sustains two neighbours and is sustained by the other two. It has then been noticed that these are, at the same time, “catenary” structures (or based on the principle of the inverted chain) and “levery” structures (or based on the principle of the lever [Brocato 2011; Brocato and Mondardini 2012]), as they partake of the nature of curved vaults and of nexorades [Baverel 2000; Baverel et al. 2000; Baverel and Nooshin 2007], possibly due to the influence on their author of a particular type of timber frame — later called Serlio’s floors [Émy 1837; Yeomans 1997] — existing much earlier as pictures by Villard De Honnecourt, Leonardo da Vinci, and Sebastiano Serlio indicate, and studied by his contemporary John Wallis (see Figure 3, where two such frames are depicted, with reference to [Heyman 1995; Khandelwal et al. 2015]).

Already during his time, it was recognised that Abeille’s interlocking bond results in the possibility of building the system the other way around, with squares on top and pyramidal gaps above. Furthermore, alternative were proposed in the same session of the French Academy, without gaps, but using more complex cuts, by Sebastien Truchet (see Figure 3). Finally, and most importantly for our scope here, it was understood that these vaults ought to discharge loads equally on the four sides².

Even though the information on Abeille’s idea was not lost after it came out (19th century drawings of the assembly are conserved at the *Arts and Métiers* museum in Paris), only two flat vaults were built following it, in 18th and 19th century Spain (Lugo’s cathedral in 1769 and Casa de Mina de Limpia at Ponton de la Oliva in 1853 [Rabasa Díaz 1998; de Nichilo 2003; Uva 2003]). Nevertheless, a renewed attention has been devoted to this subject in the last decade and some stone structures built copying

¹“Mr Abeille Ingenieur du Canal de Picardie, a imaginé une construction de plate-Bande fort ingenieuse, la coupe des Clavaux en est singuliere & contribue beaucoup à diminuer la poussée que les piés-droits auroient à soutenir, j’en aurois volontiers fait la description si elle étoit venue à ma connoissance avant que les planches de ce second Livre fussent gravées.” — de Bélidor [1729, Livre II, p. 61].

²“Puisque les coupes des claveaux des *Voutes plates* [d’Abeille] sont tournées de quatre côtéz alternativement, il est clair que ces voutes poussent aussi de quatre côtéz, à la difference des *Platebandes*, qui ne poussent que de deux côtéz; d’où il suit qu’elles font la moitié moins d’effort que les platebandes pour renverser leurs piedroits, & par consequent demandent moitié moins d’épaisseur de mur, ce qui est un avantage.” — Frézier [1738, Volume 2, p. 77].

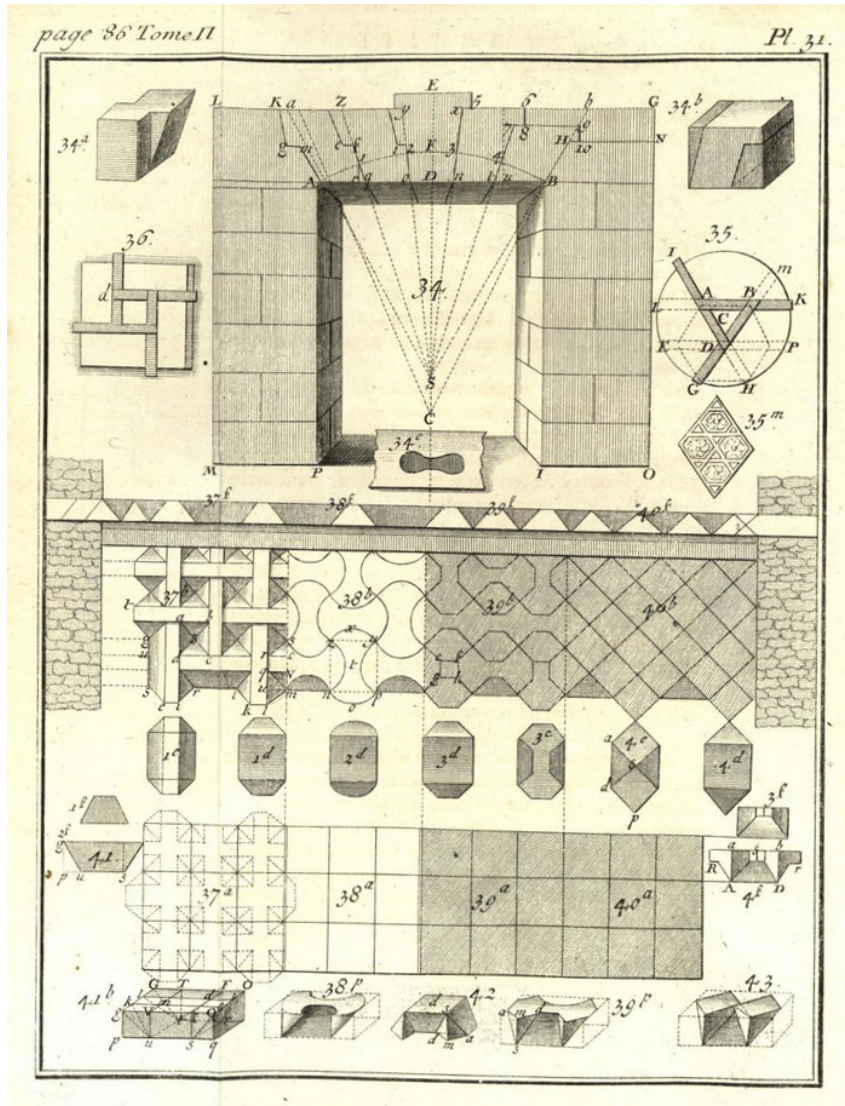


Figure 3. Alternative cuts proposed by Sebastien Truchet [Fréziers 1738, Volume 2, Pl. 31].

or adapting Abeille's interlocking principle [Etlin et al. 2008; Fallacara 2006; 2009; Sakarovitch 2006; Fleury 2009; 2010; Brocato and Mondardini 2010; 2012; 2015; Brocato et al. 2014; Mondardini 2015].

At Ponton de la Oliva, the dimensions are 3.10 m × 3.80 m × 0.21 m [Rabasa Díaz and López Mozo 2012]. Between 2003 and 2006, three vaults were built and loaded until failure at the Grands Ateliers de l'Isle d'Abeau (France), spanning square surfaces of side 2.52 m or 1.26 m, with thickness $\frac{1}{14}$ the span and joints inclined at 30° and 45° with respect to the vertical [Sakarovitch 2006; Fleury 2009; 2010].

At the same time, a vast literature has been produced on the subject of what has been — perhaps imprecisely — called “topologically interlocking materials” [Dyskin et al. 2001; 2003a; 2003b; Estrin et al. 2004; 2011; Khandelwal et al. 2012; 2015; Weizmann et al. 2016; Brocato 2018]. Abeille's

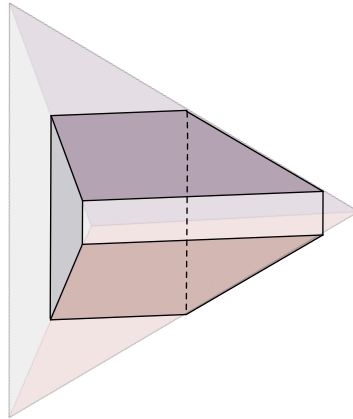


Figure 4. An example of how an Abeille’s voussoir can be obtained from a tetrahedron.

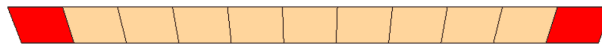


Figure 5. Vertical cut on the typical flat arch bonded according to the $\frac{1}{3}$ rule.

vaults appear then as a particular case, with interlocking blocks obtained by cutting a, possibly regular, tetrahedron with two parallel planes, one at half distance between any two nonconcurrent edges (see Figure 4).

3. Model settings

Our purpose is to perform a comparative limit analysis of the aforementioned three types of flat vaults: parabolic (or unidirectional), elliptical (or plainly bidirectional), and hyperbolic (or interlocking bidirectional). The geometries that we will define for this purpose are derived from some historical examples, but simplified to avoid unnecessary complexities.

The archetypal parabolic vault we consider here is an array of flat arches, closely disposed next to each other so that their lateral and vertical faces are in contact, but not otherwise bonded. Voussoirs are irregular polyhedra, whose upper and lower faces are squares, shifted in the direction of the span, so that two opposite faces rest vertically and the two others are suitably inclined. Their slope is defined following the so-called “1 on 3” rule of the French masons (see [Fantin 2017] for a thorough discussion on this and alternative rules in 18th and 19th century France), which means that it varies linearly between springers, where it takes the maximum absolute value of $\frac{1}{3}$, or an inclination on the vertical $\varphi = \arctan\left(\frac{1}{3}\right) = 18.4^\circ$ (see Figure 5).

It must be noticed that this disposition is not consistent with any known existing structure, because of the shift of courses that obviously appears there (see the rightmost drawing of Figure 1). As already mentioned in the previous paragraph, voussoirs can be ideally severed with planes containing the load descent path without changing this path; hence the geometry we use is statically consistent with what observable in practice (see Figure 6).

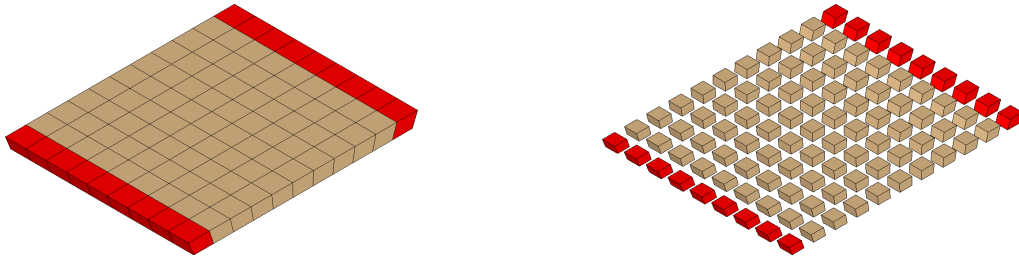


Figure 6. Archetype of a parabolic flat vault.

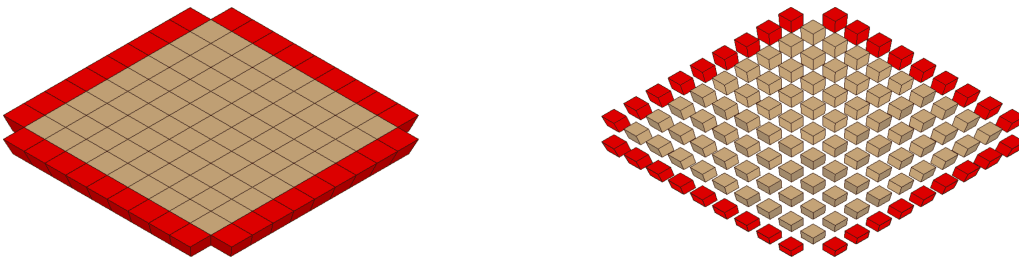


Figure 7. Archetype of an elliptical flat vault.

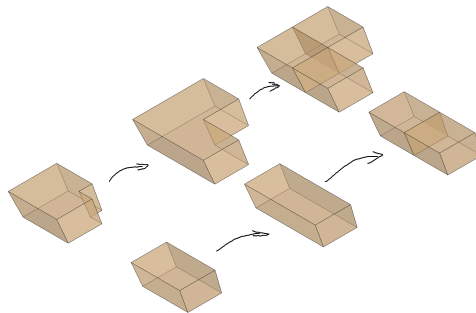


Figure 8. Simplification of the pattern of the elliptical flat vault adopted for numerical computations.

The model of elliptical flat vaults that we take into account is similar to the previous one, but now the square sides of the polyhedral voussoirs are shifted in a particular radial direction, so that all the other four faces are inclined. The inclination respects, again, the $\frac{1}{3}$ rule, but the progression is bidirectional, so that, if an array of flat arches is still observable in one direction, each arch leans on the next, proceeding from the centre to the springers, so that the same type of array can be observed in the orthogonal direction (see Figure 7).

As for parabolic vaults, in this case the model does not replicate the geometry of known examples, but remains statically representative of them because of the same principle concerning the severing of voussoirs along appropriate planes. Considering, for instance, the corner stones of the second structure from the left of Figure 1, they are modelled here as any other piece of the assembly through the steps presented in Figure 8, assuming that this simplification does not significantly affect results.

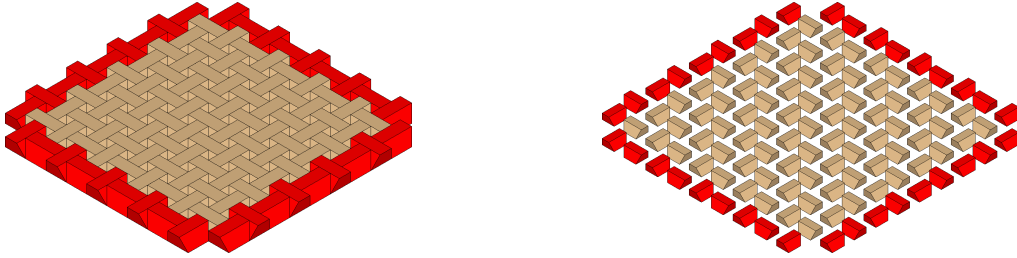


Figure 9. Archetype of a hyperbolic flat vault.

The hyperbolic flat vault archetype is made of voussoirs that can be described, in fair generality, by four parameters (see [Brocato and Mondardini 2015]), but, as the lower face of Abeille's voussoirs is meant to be a square, three suffice in the present case (when the lower face is not a square, then the gaps cross the vault through its whole thickness, or the cutting of the lateral sides is more complex than in Abeille's). The question is thus reduced to the same kind of information as in the previous cases, taking as independent parameters the side of the square, the thickness of the vault, and the angle of the joints with respect to the vertical. Differently than previously, here the angle is the same everywhere (as all voussoirs are equal) and we take the maximum angle defined by the $\frac{1}{3}$ rule, i.e., $\varphi = 18.4^\circ$. Notice that this choice is consistent with Gallon's written prescription [1735], which, as the author underlines, does not give the proportions that appear in his enclosed drawing.

As already mentioned, we are going to compare numerical results obtained for three models, the bonding of which has been presented above. Their overall geometry is the same: a square of 2.80 m, measured at mid-distance between the intrados and the extrados, with a thickness of 0.20 m (hence a ratio thickness on span of $\frac{1}{14}$). All structures are composed of $9 \times 9 = 81$ voussoirs. The considered mechanical properties are

- density (1658 kg/m^3),
- compression strength (10 MPa), and
- friction coefficient (0.7).

The loading applied for the analyses are a vertical force, uniformly distributed on the horizontal surface of the vault, and a set of forces acting independently on each of the springers of the vault. The latter have a vertical component, equilibrating the distributed force, but otherwise freely set, and a free horizontal component, or thrust, which is assumed to be orthogonal to the perimeter of the vault.

The purpose of the limit analysis is to determine a domain where the loading respects at the same time the equilibrium conditions and all safety criteria related, at the joints, to the limited compression strength, the null tension strength, and the Coulomb's friction.

The variables used to describe such domains of statically admissible loads in two dimensions are the intensity of the resultant of the vertical forces W and the intensity of the resultant of the horizontal thrusts at one side of the perimeter of the vault, say, in the x direction, $\sum H_x$.

Notice that while the parabolic vault springs from two sides only, the elliptical vault has a diagonal symmetry and thus acts equally on all sides, and the hyperbolic vault is chiral, so that it can be assumed

that the sums of the normal components of its actions along two consecutive sides of the perimeter are equal.

To handle dimensionless variables, the above mentioned forces are considered per unit weight of the vaults, so that the domains will be plotted in the W/W_0 vs. $\sum H_x/W_0$ plane, with W_0 being the total weight of the structure. Due to the gaps left by the bonding, Abeille's vault is lighter than the two others and we have

- parabolic and elliptical vault: $W_0 = 26.00$ kN;
- hyperbolic vault: $W_0 = 23.19$ kN.

4. Computational method

The planned comparisons will be carried on in the framework of limit analysis. The reason is two-fold: first, this analysis gives a hint on the ultimate structural performance requiring the least possible nongeometrical information; second, it addresses mechanical concepts (related to the onset of failure) that are, as much as possible, close to those that were used in the 18th and 19th centuries, when the debate on flat vaults flourished.

Within the broad field of limit analysis, an offspring of the force network method as first published by O'Dwyer [1999] is used here. This method generalises to three dimensions the funicular polygons constructed in two dimensional graphic statics. In short, it consists in finding the shape given by gravity to a net loaded by known weights at its nodes and respecting appropriate conditions at its boundaries, assuming the horizontal projection of the net is fixed, so that only the vertical position of the nodes at equilibrium is unknown. The solution of this problem defines both the shape of the net and the internal forces in the fabric depending on as many parameters as the assumption that the former does not depend on the intensity of the forces implies. If directly applicable to inextensible tensile nets (which generalise catenaries), the problem can be also translated to masonry vaults, where it helps define a network that generalised the concept of the inverted catenary (or the inverted funicular of a dead load). This method was extended by [Block and Ochsendorf 2007], with the use of reciprocal figures, under the name of thrust network analysis.

Consider a mass network, i.e., the network built on a given vault, with nodes corresponding to the centres of gravity of the voussoirs and branches corresponding to the interfaces between them; the thrust network analysis workflow is as follows:

- (1) Vertical forces are assigned at the nodes, corresponding to the weights of the voussoirs.
- (2) A cost function is defined, depending on the vertical coordinates of the nodes.
- (3) The geometry of the network projected on the horizontal plane is assigned.
- (4) The vertical positions of the boundary nodes are assigned (fit for the cost function); they are chosen among the parameters that will be left undetermined by the equilibrium problem and become the degrees of freedom of the optimisation problem.
- (5) A given number of force parameters is assigned, depending on the static indeterminacy of the system (usually corresponding to the thrusts along the branches of the network); they join the previous ones in the list of the degrees of freedom of the optimisation problem.

- (6) The set of internal forces verifying the self equilibrium of the network when projected in the horizontal plane is determined on the basis of the information provided in steps (3)–(5) (notice that, as only vertical loads will be applied, they are not considered at this step).
- (7) The vertical coordinates of the nodes and the internal forces in the branches are determined respecting the vertical equilibrium of the system under the load given at step (1) and the finding of step (6).
- (8) The value of the cost function of step (2) is computed.
- (9) Coming iteratively back to step (4), an optimisation procedure is run to define the best set of degrees of freedom based on the cost function defined at step (2).

When used as a limit analysis tool, this method is generally used to find, among all networks generated by the parameters, those whose nodes fall within the limits of the masonry structure. Notwithstanding the recurrence of the idea that this result can be directly related to safety (see [O’Dwyer 1999; Block and Ochsendorf 2008; Block 2009; Block and Lachauer 2014a; 2014b]), a digression is needed here.

In a vault made of voussoirs, failure may occur by opening joints. The relevant information is then the set of centres of pressure, i.e., the points where the resultant of the contact stresses intersects the plane of the joint. The safe theorem expressed by Heyman [1995] helps conclude that the vault is stable — under the hypotheses that the joints offer no tensile strength and infinite compressive strength, and suffer no sliding — if all centres of pressure fall within the convex hull of the corresponding contact surface (and fall strictly within it in a sufficient number of fit sequences to avoid potential failure).

Any stability condition expressed in terms of positions of the nodes is then to be understood as an approximation of the one deduced from the safe theorem, which concerns the positions of centres of pressure, even though the two sets are correlated. Clearly, in the limit of infinitesimal voussoirs, i.e., when both the distance between subsequent joints and the thickness of the vault tend to zero, the network of nodes coincides with that of centres of pressure, but if any of the two characteristic lengths quoted above are finite, the two pieces of information are distinct. This difference can be deemed negligible when the method is applied to form finding for design purposes, as then the voussoir’s geometry is defined after the thrust network. On the contrary, it is not so in at least one of the cases at issue, namely in hyperbolic flat vaults.

To tackle problems where the limit of infinitesimal voussoirs can’t be accepted and enhance the thrust network method as a tool to study existing masonry structures, the first two authors have analysed some historical methods for vault calculation and proposed the introduction of new equilibrium states among those available for the net by considering additional partial branches as described below [Ciblac and Fantin 2015; Fantin and Ciblac 2016].

The thrust network analysis is based on the hypothesis that all forces applied to one voussoir converge into one point, taken as a node of the thrust network. This is a sufficient but not a necessary condition to ensure moment equilibrium of the voussoir. Considering a single block subject to four forces and its own weight, four different equilibrium cases can be given, as shown in Figure 10. Only the case (a) respects the intersection hypothesis, and can thus be produced by a thrust network analysis, as in cases (b), (c), and (d), although force and moment equilibrium are fulfilled, forces intersect in two points, or do not intersect at all.

Notice that in case (b), the intersections of the forces take place in two distinct nodes, instead of one, but the horizontal projections of these nodes are identical. This configuration can be obtained using the

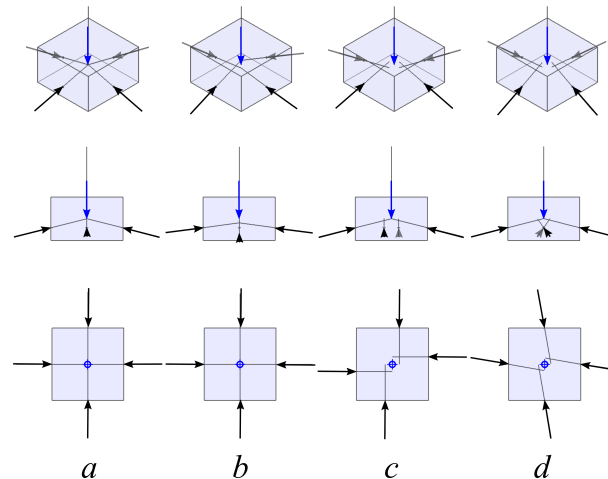


Figure 10. Equilibrium cases: (a) concurrent forces and (b-d) nonconcurrent forces.

particular mass network refinement proposed by Fantin and Ciblac [2016]. For this purpose, instead of relating each voussoir to one and only one node in the mass network, let us divide it into two smaller units and create correspondingly two nodes in the network, with their respective masses. The two nodes are joined by a new branch, which we call the “additional partial branch”, that is related to the internal force across the surface splitting the voussoir. The other branches of the network, which normally connect any two adjacent nodes and can be called “standard thrusting branches”, are not necessarily doubled in this process, as they are defined in such a way that each carries a relevant piece of information on a joint between voussoirs (e.g., one branch per joint).

Let us focus on the case when all additional partial branches are vertical (i.e., voussoirs are ideally split by one horizontal cut; notice that it is possible, though not needed here, to remove this assumption [Fantin and Ciblac 2016]). Then, the horizontal equilibrium of step (6) in the workflow above, not taking into account the forces in the additional partial branches, leaves them undetermined. Consequently, neither can the vertical equilibrium of step (7) be used to compute them. Hence, these forces must be included in the list of the degrees of freedom in the optimisation problem. Figure 11 illustrates the case when the mass refinement splits one node into two, belonging to the same vertical line, which allows one to consider an equilibrium similar to case (b) of Figure 10, but not cases (c) and (d).

When it comes to the optimisation procedure, the method of [Ciblac and Fantin 2015; Fantin and Ciblac 2016] introduces another variant to the thrust network analysis: the cost function is not built uniquely on the vertical coordinates of the nodes, as it takes into account the intersections of each of the standard thrusting branches with the surface of the corresponding joint. This is an important advantage, as the processed information is now consistent with the safety criteria of vaults for joint opening or sliding, even if, to obtain it, a much larger problem than the standard must have been posed by including the forces along the additional partial branches among the degrees of freedom of the system.

In particular, it is handy using as the cost function the global coefficient of safety of the structure, defined as the Euclidean distance between the quoted intersection and the boundary of the joint, which requires some additional computational stratagem to be quickly evaluated.

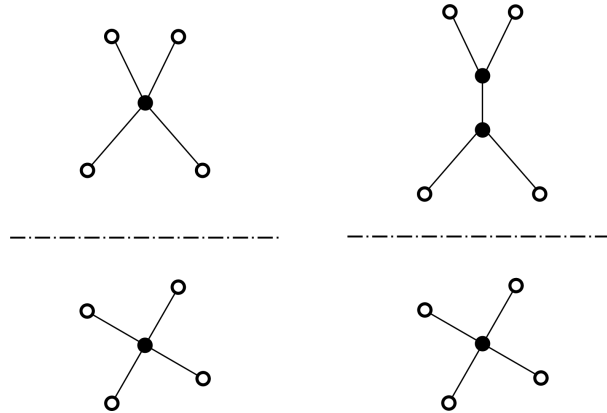


Figure 11. Front view (top) and horizontal projection (bottom) of a four-valent node before (left) and after (right) mass network refinement.

5. Numerical implementation

A numerical application of the described extension of the thrust network analysis, named Manacoh, was implemented in a Microsoft Excel worksheet with Visual Basic developments. Manacoh and its tutorials are freely available in a dedicated web site (<http://bestrema.fr/manacoh/>). It builds the geometry for parametric preset examples (specific geometries can also be loaded), solves the equilibrium equations, and offers the possibility to explore various equilibrium solutions through optimisation strategies derived from historical examples and including the techniques presented in this paper.

Because the computing capacity of Manacoh is relatively limited by the use of a general public environment, some numerical stratagems have been used to reduce the duration of computations. The various types of degrees of freedom (the horizontal forces in the standard thrusting branches, the vertical position of the boundary nodes, and the vertical forces in the additional partial branches) usually exhibit some regularity when at the optimum solution, provided that the structure studied has a regular geometry. This potential regularity is exploited by Manacoh, calling upon Lagrange polynomials to interpolate the degrees of freedom and thus lessen the number of free parameters in the optimisation process.

A second numerical scheme to make computations faster is the smoothing of the cost function by the following type of approximation: given any real function $d(x)$,

$$x : \min_x \|d(x)\| \approx x : \min_x (d(x)^{-p})^{-1/p} \quad \text{for } p \geq p_0 > 0;$$

p_0 being large enough for the approximation to be acceptable.

The type and number of degrees of freedom in the parabolic case, not introducing additional partial branches with respect to the standard thrust network analysis, are

(A) 9 horizontal thrusts, becoming 1 by translational invariance;

(B) 18 vertical coordinates of the boundary nodes, becoming 1 by translational invariance and symmetry;

when including partial branches, this case requires the additional

(C) 81 internal forces in the vertical partial branches, becoming 5 by translational invariance and symmetry.

In the elliptical cases, not introducing additional partial branches,

(A) 18 horizontal thrusts, becoming 5 by symmetry;

(B) 36 vertical coordinates of the boundary nodes, becoming 5 by symmetry;

when including partial branches, add

(C) 81 internal forces in the vertical partial branches, becoming 10 by symmetry;

thus rising the size of the problem to a minimal number of 20 degrees of freedom.

To lighten the optimisation problem in the second case, the (A) and (B) parameters were separately interpolated by a Lagrange polynomial of degree $k = 0, 2, \text{ or } 9$ ($k = 0$ means that a uniform thrust and an equal vertical position of the boundary nodes are considered, $k = 9$ means no interpolation).

The Abeille vault possesses less symmetries than the previous ones and it is not possible to analyse it by the standard method without partial branches. The total number of degrees of freedom is in this case 45, divided as follows:

(A) 18 horizontal thrusts, becoming 10 by symmetry;

(B) 36 vertical coordinates of the boundary nodes, becoming 10 by symmetry;

(C) 81 internal forces in the vertical partial branches, becoming 25 by symmetry.

Performing calculations with a smaller Abeille vault (5×5 voussoirs) it has been observed that the forces in the partial branches of the optimum solution depend approximately linearly on the distance from the centre of the vault. Hence, in addition to the interpolation by Lagrange polynomials of degree k of the (A) and (B) parameters, an approximation of the (C) parameters with polynomials of degree $r = 2$ in the quoted distance has been implemented to reduce the optimisation problem.

In any case, the domains of statically admissible loads were computed taking into account the intersections of the standard thrusting branches with the joints, not the positions of the nodes of the network. Processing this information it is also possible to take friction into account, by checking that the slope of the branch on the surface of the joint is below the limit of Coulomb's friction coefficient.

6. Results on the statically admissible loadings

Results obtained for the parabolic and elliptical vault are plotted in Figure 12. From the point of view of the method used for the analysis, they show that the introduction of partial branches improves the result, as it helps find a larger domain of statically admissible loadings (orange plots), especially if the forces in all partial branches are taken into account ($F_v \neq 0$, light orange case in the plot).

If the forces in all partial branches are taken as null ($F_v = 0$, dark orange case in the plot), the thrusting branches along the x and the y axis are totally independent from each other. This type of solution cannot be attained with a standard thrust network analysis without partial branches. The computed domain is, as expected, very close to an affine transformation of the domain of the parabolic vault doubling the vertical extent (compare the dark orange and grey plots in Figure 12). This result is a better approximation than the best obtained without partial branches (light blue plot) at least in the range of mid to high thrusts and

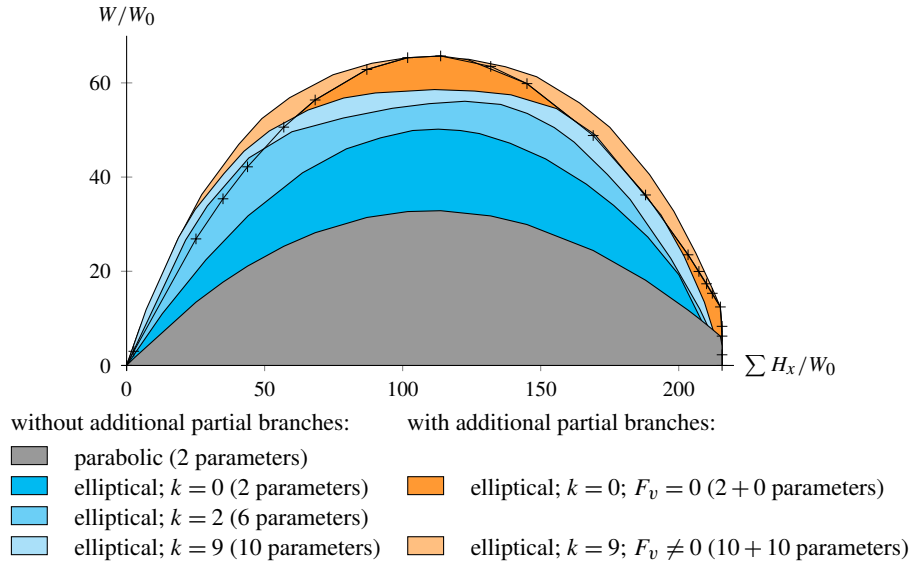


Figure 12. Domains of the statically admissible loadings in the a -dimensional thrust vs. weight plane, for parabolic and elliptical flat vaults. The results obtained by the refined method, including partial branches, displayed in orange, give a better approximation of the real domain.

it has been obtained with only two parameters, instead of the ten required by the competing unrefined network.

From the point of view of the numerical tools, even if the interpolation with Lagrange polynomials reduces — more than expected — the size of the domain, it is useful for finding a good starting point, which is crucial for optimisation. To test this advantage, we have started an optimisation with $k = 0$, then use the found optimal solution to start a new optimisation process with $k = 2$ and finally go from this result to the one with $k = 9$. This process was found to be much more time efficient than optimising directly without interpolation.

Finally, from the point of view of the structural comparison, we observe that the domain of statically admissible loading of the elliptical flat vault is notably larger than the domain of the parabolic one, with the elliptical vault performing better than the sum of two (orthogonal) parabolic ones (see the difference between the grey and light orange plots in Figure 12; in the same figure, the boundary of the domain obtained doubling the height of the grey plot is a line marked by +).

Examples of the shape of the related thrust networks are given in Figures 13 and 14. It can be observed that the addition of partial branches allows the lines of thrust to gain more inclination where the release of a larger shear is needed, while the orthogonal lines may come closer to the shape of an ideal catenary. This effect is particularly important in the vicinity of the boundary, where an equivalent plate would experience negative bending moments and withstand Kirchhoff shear forces pointing downward at the corners.

Results concerning the hyperbolic, or Abeille's, vault are shown in Figure 15, superposed to the largest domains obtained for the other cases.

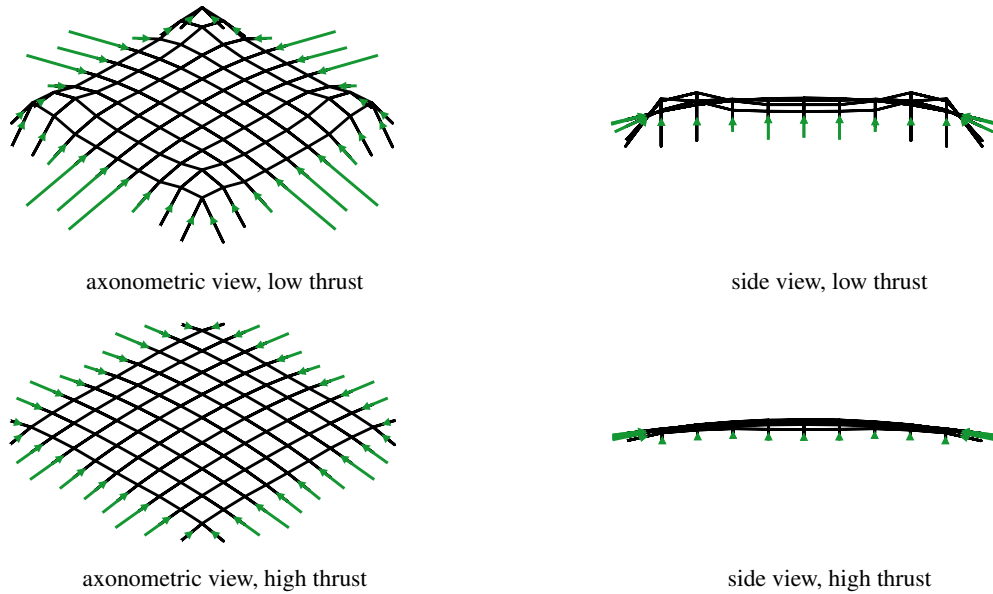


Figure 13. Axonometric view (left) and side view (right) of thrust networks without additional branches for the elliptical flat vault, computed for $k = 9$, under low thrust (above) and high thrust (below).

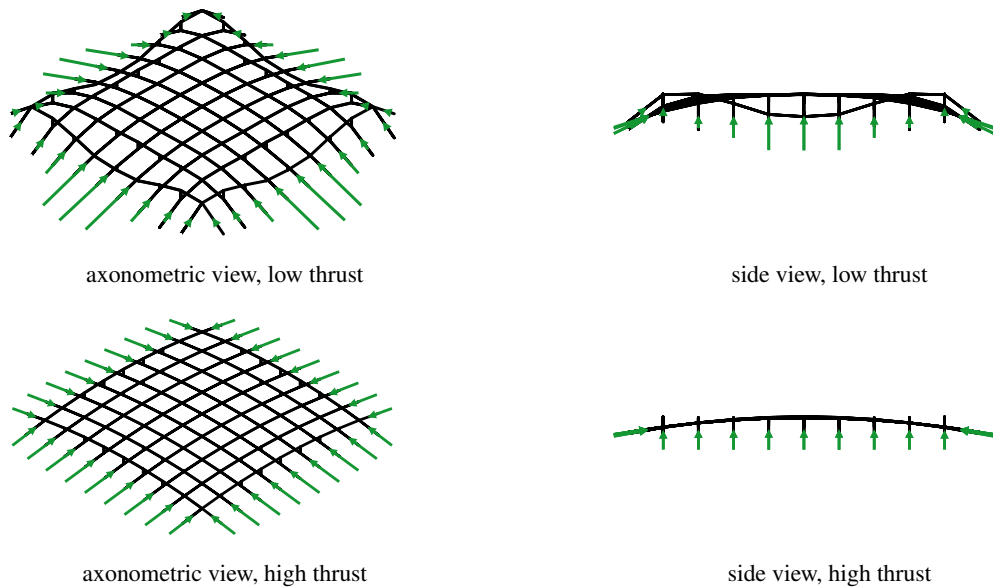


Figure 14. Axonometric view (left) and side view (right) of thrust networks with additional partial branches for the elliptical flat vault, computed for $k = 9$ and $F_v \neq 0$, under low thrust (above) and high thrust (below).

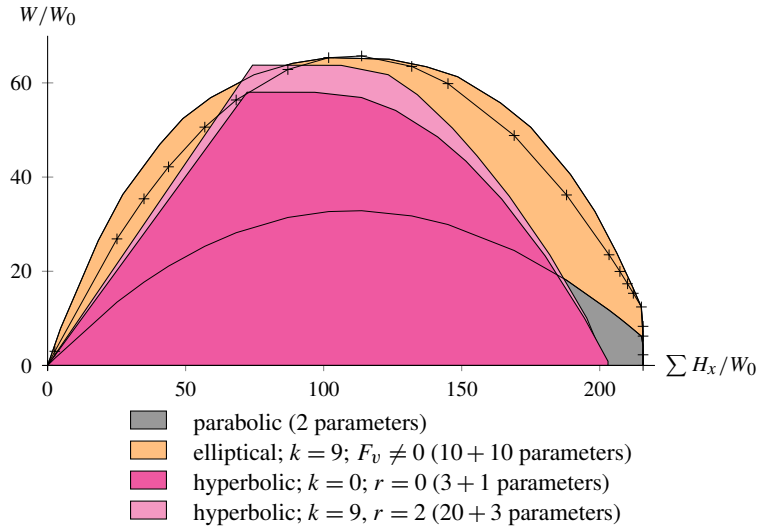


Figure 15. Domains of the statically admissible positive loadings for Abeille's vault, compared to those of the parabolic and elliptical vault. Notice that Abeille's vault admits negative loadings.

Notice that the boundaries of the domains displayed for the parabolic and the elliptical vault do not include parts depending on the selected value of the friction coefficient: failure of these vaults occurs always by opening of the joints. This is not the case of Abeille's vault, where the friction criterion controls the minimum thrust (an infinite resistance to friction entailing the possibility of supporting vertical loads with no thrust) and thus the domains of statically admissible loadings are limited from the side of small thrusts by a straight line corresponding to the limit of failure by sliding.

Still from the point of view of the structural comparison of the three systems, it can be observed that the domain of the hyperbolic one is smaller than that of the two others for high thrust, due to the smaller size of the joints in the former. The hyperbolic vault performs otherwise better than the parabolic one and is quite close to the elliptical vault only for middle thrusts, being less resistant than the latter in the range of low thrusts.

Finally, it must be observed that only the part of the domain of Abeille's vault including positive loads is displayed in Figure 15; this vault can actually withstand forces in the opposite direction within the same or very close limits, which is not possible for the two others.

Observing Figure 14, the adjective elliptical designating this type of vault can be explained, at least within the accuracy limits of the thrust network image of the internal actions. Let us call $z_{ij}^{(x)}$ and $z_{ij}^{(y)}$ the vertical coordinates of the two nodes of the network representing one voussoir (i.e., joined by a vertical, additional partial branch), assume i counting nodes having the same y coordinate and j having the same x and the exponent in $z_{ij}^{(x)}$ and $z_{ij}^{(y)}$ denote the direction along which the node is connected to its neighbours by a standard thrusting branch.

Let us define, at any point ij ,

$$\kappa_{ij}^{(x)} = z_{i-1j}^{(x)} - 2z_{ij}^{(x)} + z_{i+1j}^{(x)}; \quad \kappa_{ij}^{(y)} = z_{ij-1}^{(y)} - 2z_{ij}^{(y)} + z_{ij+1}^{(y)}.$$

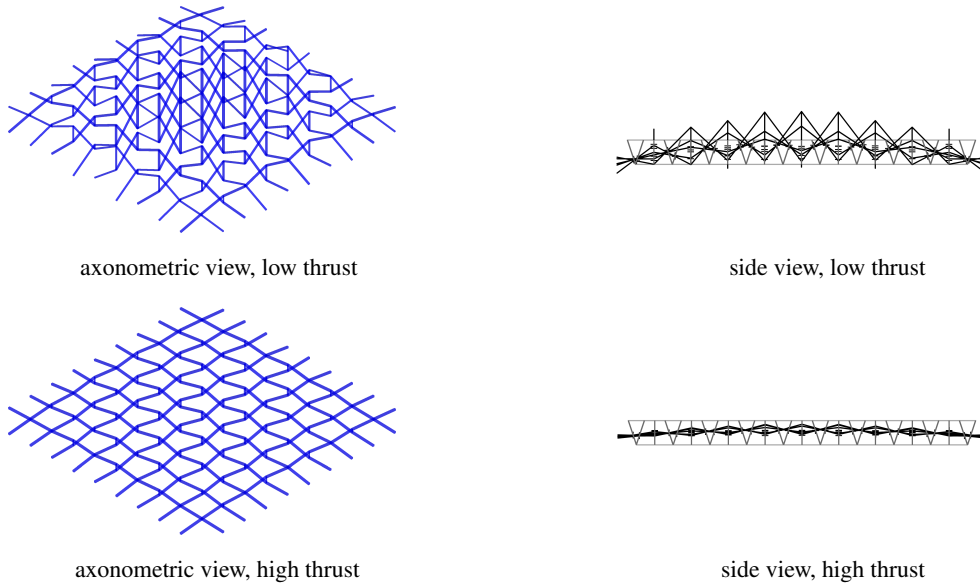


Figure 16. Axonometric view (left) and side view (right) of thrust networks with additional partial branches for the hyperbolic flat vault, computed for $k = 9$ and $r = 2$, under low thrust (above) and high thrust (below).

Any two nodes of the network representing one voussoir are in equilibrium under the weight of the voussoir and the four forces acting along the standard thrusting branches. With the exception of some of the boundary nodes, these four internal forces point upward; it is

$$\kappa_{ij}^{(x)} \kappa_{ij}^{(y)} > 0. \quad (6-1)$$

If we denote by $v_{ij/hj}$ the vertical component of the force carried by the branch joining the ij node with the hj node and $v_{ij/ik}$ that joining the ij with ik , the equality of the signs of the thrusts in the x and y direction entail

$$\text{sgn}((v_{ij/i-1j} - v_{ij/i+1j})(v_{ij/ij-1} - v_{ij/ij+1})) = \text{sgn}(\kappa_{ij}^{(x)} \kappa_{ij}^{(y)});$$

which means that the net contributions of the branches converging on the ij node in the two directions point upward when (6-1) is true (both opposed to the external force).

Observing Figure 16, on the contrary, we find

$$\kappa_{ij}^{(x)} \kappa_{ij}^{(y)} < 0, \quad (6-2)$$

with two branches pushing upward and two downward. Finally, even if not graphically presented here, the case of parabolic vaults is evidently one where

$$\kappa_{ij}^{(x)} \kappa_{ij}^{(y)} = 0, \quad (6-3)$$

and one of the two couples of branches is inactive.

Let us imagine the surface that has, locally at ij , $\kappa_{ij}^{(x)}$ and $\kappa_{ij}^{(y)}$ as curvatures and x and y as principal directions of curvature. This surface has there a Dupin's indicatrix that is an ellipse if $\kappa_{ij}^{(x)} \kappa_{ij}^{(y)} > 0$,

a parabola if $\kappa_{ij}^{(x)} \kappa_{ij}^{(y)} = 0$ and a hyperbola if $\kappa_{ij}^{(x)} \kappa_{ij}^{(y)} < 0$; correspondingly, ij is currently named an elliptical, parabolic, or hyperbolic point of the surface.

By analogy with this nomenclature, we named elliptical the flat vault having a thrust network whose “analogous” surfaces have (almost everywhere) elliptical points, parabolic the vault whose limit surfaces have a.e. parabolic points, and hyperbolic those whose limit surfaces have a.e. hyperbolic points. Equations (6-1), (6-2), and (6-3) disambiguate the attribution.

Statically, this characteristic entails that some branches push upward, some downward (as explained before), hence the image presented in Section 2 of a “monotonic” load descent in parabolic and elliptical vaults, with the maximally sheared plane corresponding to the maximum force acting along a standard thrusting branch and a minimally sheared plane corresponding to the minimal force along such a branch (clearly, the case where max and min coincide being possible).

In the case of hyperbolic flat vaults, the max and min shear have opposite sign, hence the image of a local division of the voussoir in quarters, with alternating shears.

7. Conclusion

Three model flat vaults, derived from historical examples, have been compared on the basis of their statically admissible loadings, using an enhanced version of the thrust network analysis:

- (1) a unidirectional vault, designed following the pattern of a “barrel” vault and named here parabolic;
- (2) a plainly bidirectional vault, having the pattern of a “pavillon” vault and named here elliptical;
- (3) an interlocking bidirectional vault, made according to Abeille’s system, which we named hyperbolic.

The work presented here lead to the conclusion that an enhancement of the thrust network analysis, taking more precisely into account the rotational equilibrium of voussoirs, is necessary to capture a wider domain of statically admissible loadings and, in one case, to be able to describe the system at all.

Computations were performed on a Microsoft Excel-based application, named Manacoh, developed by the first and second authors and publicly accessible on the internet. Some numerical expedients, called here to circumvent limitations arising from the use of a general public environment, can prove useful to handle large systems within more powerful numerical implementations. In particular, Lagrange polynomials can reduce the computational effort when used to interpolate iteratively the degrees of freedom of the optimisation procedure inherent in the thrust network analysis.

The comparison of the three archetypes shows that the bonding of voussoirs plays — as expected — a fundamental role in their stability, with system (1) having the best performances under vertical descending loadings and system (2), the resistance of which is quite close to that of the former, being also capable of withstanding ascending loadings.

Observing the thrust networks obtained in the different cases at the onset of failure, it is possible to gain an insight on the mechanical behaviour of flat vaults (at least if the shift from the limit is allowed). If parabolic flat vaults are plainly catenary structures (with parallel discharge arches bridging across supports), the elliptical ones are not exactly so and hyperbolic even less.

Elliptical vaults mimic the behaviour of continuous plates and thus the rotational equilibrium of their voussoirs plays an important role when close to the corners. In these areas the enhanced thrust network

displays the superposition of two inverted catenary structures, but not the existence of a single inverted “catenary net”, which can be observed elsewhere in the structure.

Hyperbolic flat vaults do not show at all the formation of such a single net, so that they can barely be considered catenary structures. Their thrust networks are wavy, not as a single net could do, but as a weaving fabric. Each voussoir, bearing shear forces of alternating sign at quarters of the horizontal projection, works both as a lever and as the link of an inverted chain, which confirms the idea that these are partly catenary and partly “levery” structures, if the neologism is accepted.

Acknowledgements

The results presented in this paper have been obtained during Mr. Fantin’s doctorate. The authors thank for his help on numerical methods Marco Czarnecki, Institut de Mathématiques et Modélisation de Montpellier, UMR 5030 CNRS, Université Montpellier 2, France.

References

- [Baverel 2000] O. L. S. Baverel, *Nexorades: a family of interwoven space structures*, Ph.D. thesis, University of Surrey, 2000, <https://tinyurl.com/bavnex>.
- [Baverel and Nooshin 2007] O. Baverel and H. Nooshin, “Nexorades based on regular polyhedra”, *Nexus Netw. J.* **9**:2 (2007), 281–298.
- [Baverel et al. 2000] O. Baverel, H. Nooshin, Y. Kuroiwa, and G. A. R. Parke, “Nexorades”, *Int. J. Space Struct.* **15**:2 (2000), 155–159.
- [de Bélidor 1729] B. F. de Bélidor, *La science des ingénieurs dans la conduite des travaux de fortification et d’architecture civile*, Jombert, Paris, 1729.
- [Block 2009] P. C. V. Block, *Thrust network analysis: exploring three-dimensional equilibrium*, Ph.D. thesis, Massachusetts Institute of Technology, 2009, <https://tinyurl.com/phdbloc>.
- [Block and Lachauer 2014a] P. Block and L. Lachauer, “Three-dimensional (3D) equilibrium analysis of Gothic masonry vaults”, *Int. J. Archit. Herit.* **8**:3 (2014), 312–335.
- [Block and Lachauer 2014b] P. Block and L. Lachauer, “Three-dimensional funicular analysis of masonry vaults”, *Mech. Res. Commun.* **56** (2014), 53–60.
- [Block and Ochsendorf 2007] P. Block and J. Ochsendorf, “Thrust network analysis: a new methodology for three-dimensional equilibrium”, *J. IASS* **48**:3 (2007), 167–173.
- [Block and Ochsendorf 2008] P. Block and J. Ochsendorf, “Lower-bound analysis of masonry vaults”, pp. 593–600 in *Structural analysis of historic construction: preserving safety and significance* (Bath, UK, 2008), edited by D. D’Ayala and E. Fodde, Proc. Int. Conf. Struct. Anal. Historic Constr. **6**, CRC, London, 2008.
- [Brocato 2011] M. Brocato, “Reciprocal frames: kinematical determinacy and limit analysis”, *Int. J. Space Struct.* **26**:4 (2011), 343–358.
- [Brocato 2018] M. Brocato, “A continuum model of interlocking structural systems”, *Rend. Accad. Naz. Lincei* **29**:1 (2018), 63–83.
- [Brocato and Mondardini 2010] M. Brocato and L. Mondardini, “Geometric methods and computational mechanics for the design of stone domes based on Abeille’s bond”, pp. 149–162 in *Advances in architectural geometry* (Vienna, 2010), edited by C. Ceccato et al., Springer, 2010.
- [Brocato and Mondardini 2012] M. Brocato and L. Mondardini, “A new type of stone dome based on Abeille’s bond”, *Int. J. Solids Struct.* **49**:13 (2012), 1786–1801.
- [Brocato and Mondardini 2015] M. Brocato and L. Mondardini, “Parametric analysis of structures from flat vaults to reciprocal grids”, *Int. J. Solids Struct.* **54** (2015), 50–65.

- [Brocato et al. 2014] M. Brocato, W. Deleporte, L. Mondardini, and J.-E. Tanguy, “A proposal for a new type of prefabricated stone wall”, *Int. J. Space Struct.* **29**:2 (2014), 97–112.
- [Ciblac and Fantin 2015] T. Ciblac and M. Fantin, “Rediscovering Durand-Claye’s method using force network method implemented for construction history”, pp. 439–446 in *Proc. Fifth International Congress on Construction History* (Chicago, 2015), edited by D. Friedman et al., Constr. Hist. Soc. Amer., Chicago, 2015.
- [Dyskin et al. 2001] A. V. Dyskin, Y. Estrin, A. J. Kanel-Belov, and E. Pasternak, “A new concept in design of materials and structures: assemblies of interlocked tetrahedron-shaped elements”, *Scr. Mater.* **44**:12 (2001), 2689–2694.
- [Dyskin et al. 2003a] A. V. Dyskin, Y. Estrin, A. J. Kanel-Belov, and E. Pasternak, “A new principle in design of composite materials: reinforcement by interlocked elements”, *Compos. Sci. Technol.* **63**:3-4 (2003), 483–491.
- [Dyskin et al. 2003b] A. V. Dyskin, Y. Estrin, A. J. Kanel-Belov, and E. Pasternak, “Topological interlocking of platonic solids: a way to new materials and structures”, *Philos. Mag. Lett.* **83**:3 (2003), 197–203.
- [Émy 1837] A.-R. Émy, *Traité de l’art de la charpenterie*, Carilian-Gœury, Paris, 1837.
- [Estrin et al. 2004] Y. Estrin, A. V. Dyskin, E. Pasternak, S. Schaare, S. Stanchits, and A. J. Kanel-Belov, “Negative stiffness of a layer with topologically interlocked elements”, *Scr. Mater.* **50**:2 (2004), 291–294.
- [Estrin et al. 2011] Y. Estrin, A. V. Dyskin, and E. Pasternak, “Topological interlocking as a material design concept”, *Mater. Sci. Eng. C* **31**:6 (2011), 1189–1194.
- [Etlin et al. 2008] R. A. Etlin, G. Fallacara, and L. C. P. Tamborero, *Plaited stereotomy: stone vaults for the modern world*, Aracne, Rome, 2008.
- [Fallacara 2006] G. Fallacara, “Digital stereotomy and topological transformations: reasoning about shape building”, pp. 1075–1092 in *Proc. Second International Congress on Construction History, I* (Cambridge, 2006), edited by M. Dunkeld et al., Constr. Hist. Soc., Cambridge, 2006.
- [Fallacara 2009] G. Fallacara, “Toward a stereotomic design: experimental constructions and didactic experiences”, pp. 553–559 in *Proc. Third International Congress on Construction History* (Cottbus, Germany, 2009), edited by K.-E. Kurrer et al., Neunplus1, Berlin, 2009.
- [Fantin 2017] M. Fantin, *Étude des rapports entre stéréotomie et résistance des voûtes clavées*, Ph.D. thesis, Université Paris-Est, 2017, <http://tel.archives-ouvertes.fr/tel-01834617>.
- [Fantin and Ciblac 2016] M. Fantin and T. Ciblac, “Extension of thrust network analysis with joints consideration and new equilibrium states”, *Int. J. Space Struct.* **31**:2-4 (2016), 190–202.
- [Fleury 2009] F. Fleury, “Evaluation of the perpendicular flat vault inventor’s intuitions through large scale instrumented testing”, pp. 611–618 in *Proc. Third International Congress on Construction History* (Cottbus, Germany, 2009), edited by K.-E. Kurrer et al., Neunplus1, Berlin, 2009.
- [Fleury 2010] F. Fleury, “Les idées sous-jacentes à la conception de la voûte plate perpendiculaire”, pp. 283–291 in *Édifices & artifices: histoires constructives* (Paris, 2008), edited by R. Carvais et al., Picard, Paris, 2010.
- [Fraternali 2010] F. Fraternali, “A thrust network approach to the equilibrium problem of unreinforced masonry vaults via polyhedral stress functions”, *Mech. Res. Commun.* **37**:2 (2010), 198–204.
- [Frézier 1738] A.-F. Frézier, *La théorie et la pratique de la coupe des pierres et des bois pour la construction des voûtes et autres parties des bâtiments civils et militaires, ou traité de stereotomie a l’usage de l’architecture, II*, Doulsseker, Strasbourg, 1738.
- [Gallon 1735] J.-G. Gallon, *Machines et inventions approuvées par l’Académie royale des sciences, depuis son établissement jusqu’à present, avec leur description, I*, Martin, Coignard, Guerin, Paris, 1735.
- [de Goes et al. 2013] F. de Goes, P. Alliez, H. Owahdi, and M. Desbrun, “On the equilibrium of simplicial masonry structures”, *ACM Trans. Graph.* **32**:4 (2013), art. id. 93.
- [Heyman 1995] J. Heyman, *The stone skeleton: structural engineering of masonry architecture*, Cambridge Univ. Press, 1995.
- [Khandelwal et al. 2012] S. Khandelwal, T. Siegmund, R. J. Cipra, and J. S. Bolton, “Transverse loading of cellular topologically interlocked materials”, *Int. J. Solids Struct.* **49**:18 (2012), 2394–2403.
- [Khandelwal et al. 2015] S. Khandelwal, T. Siegmund, R. J. Cipra, and J. S. Bolton, “Adaptive mechanical properties of topologically interlocking material systems”, *Smart Mater. Struct.* **24**:4 (2015), art. id. 045037.

- [López Mozo 2003] A. López Mozo, “Planar vaults in the Monastery of El Escorial”, pp. 1327–1334 in *Proc. First International Congress on Construction History* (Madrid, 2003), edited by S. Huerta Fernández, Inst. Juan de Herrera, Madrid, 2003.
- [Mondardini 2015] M. L. Mondardini, *Contribution au développement des structures en pierre de taille: modélisation, optimisation et outils de conception*, Ph.D. thesis, Université Paris-Est, 2015, <https://tinyurl.com/mond2015>.
- [de Nichilo 2003] E. de Nichilo, “Learning from stone traditional vaulted systems for the contemporary project of architecture”, pp. 743–754 in *Proc. First International Congress on Construction History, II* (Madrid, 2003), edited by S. Huerta Fernández, Inst. Juan de Herrera, Madrid, 2003.
- [O’Dwyer 1999] D. O’Dwyer, “Funicular analysis of masonry vaults”, *Comput. Struct.* **73**:1-5 (1999), 187–197.
- [Pérouse de Montclos 1982] J.-M. Pérouse de Montclos, *L’architecture à la française: du milieu du XVe à la fin du XVIIIe siècle*, Picard, Paris, 1982.
- [Rabasa Díaz 1998] E. Rabasa Díaz, “La bóveda plana de Abeille en Lugo”, pp. 409–415 in *Actas del Segundo Congreso Nacional de Historia de la Construcción* (A Coruña, Spain, 1998), edited by F. Bores et al., Inst. Juan de Herrera, Madrid, 1998.
- [Rabasa Díaz and López Mozo 2012] E. Rabasa Díaz and A. López Mozo, “Les joints occultes sur plates-bandes et voûtes plates en Espagne”, pp. 288–295 in *L’architrave, le plancher, la plate forme: Nouvelle histoire de la construction*, edited by R. Gargiani, Presses Polytech. Univ. Romandes, Lausanne, Switzerland, 2012.
- [Rippmann et al. 2012] M. Rippmann, L. Lachauer, and P. Block, “Interactive vault design”, *Int. J. Space Struct.* **27**:4 (2012), 219–230.
- [Rondelet 1804] J. Rondelet, *Traité théorique et pratique de l’art de bâtir*, tome II, Chez l’Auteur, Paris, 1804.
- [Rondelet 1828] J. Rondelet, *Traité théorique et pratique de l’art de bâtir: planches*, Chez l’Auteur, Paris, 1828.
- [Sakarovitch 2006] J. Sakarovitch, “Construction history and experimentation”, pp. 2777–2792 in *Proc. Second International Congress on Construction History* (Cambridge, 2006), edited by M. Dunkeld, Constr. Hist. Soc., Cambridge, 2006.
- [van Swinderen and Coenders 2009] T. van Swinderen and J. Coenders, “Tool to design masonry double-curved shells”, pp. 1136–1144 in *Evolution and trends in design, analysis and construction of shell and spatial structures* (Valencia, 2009), edited by A. Domingo and C. Lázaro, Editorial UPV, Valencia, 2009.
- [Uva 2003] G. R. Uva, “Learning from traditional vaulted systems for the contemporary design: an updated reuse of flat vaults: analysis of structural performance and recent safety requirements”, pp. 2015–2021 in *Proc. First International Congress on Construction History* (Madrid, 2003), edited by S. Huerta Fernández, Inst. Juan de Herrera, Madrid, 2003.
- [Vouga et al. 2012] E. Vouga, M. Höbinger, J. Wallner, and H. Pottmann, “Design of self-supporting surfaces”, *ACM Trans. Graph.* **31**:4 (2012), art. id. 87.
- [Weizmann et al. 2016] M. Weizmann, O. Amir, and Y. J. Grobman, “Topological interlocking in buildings: a case for the design and construction of floors”, *Automation Constr.* **72**:1 (2016), 18–25.
- [Yeomans 1997] D. Yeomans, “The Serlio floor and its derivations”, *Archit. Res. Quart.* **2**:3 (1997), 74–83.

Received 16 Jun 2018. Revised 28 Jan 2019. Accepted 4 Feb 2019.

MATHIAS FANTIN: mathias.fantin@polytechnique.edu
Laboratoire GSA, ENSA Paris-Malaquais, Paris, France

THIERRY CIBLAC: thierry.ciblac@paris-malaquais.archi.fr
Laboratoire GSA, ENSA Paris-Malaquais, Paris, France

MAURIZIO BROCATO: maurizio.brocato@paris-malaquais.archi.fr
Laboratoire GSA, ENSA Paris-Malaquais, Paris, France

SEISMIC VULNERABILITY OF DOMES: A CASE STUDY

CONCETTA CUSANO, CLAUDIA CENNAMO AND MAURIZIO ANGELILLO

In this work, a simplified structural analysis of the main dome of San Francesco di Paola in Naples is performed by adopting both analytical and graphical approaches. The analytical process is based on the simplified membrane theory and the graphical methodology on the slicing technique. Both methods are used to determine the safety of the dome design under vertical and horizontal loads. We explore the effects of earthquakes by introducing horizontal forces proportional to the weight. Since the slicing technique does not consider the hoop compressive stresses building up in the upper part of the cap, the geometrical safety factor obtained by combining the analytical with the graphical method for the sole dome is lower than the one obtained with the analytical method. The estimate of the a/g factor for the dome-buttress structural system obtained with the graphical method is greater than the level accepted for the seismic area of Naples.

1. Introduction

The aim of the present work is to compare results of equilibrium analyses of masonry domes, treated as composed of Heyman's unilateral material and performed with both analytical and graphical methods, for a case study. The analytical method is based on the simplified membrane theory for unilateral materials (see [Angelillo and Fortunato 2004]) and the graphical method on the so-called slicing technique (see [Heyman 1966]). The two methods can be both employed to assess the geometrical safety factor of domes under the effect of vertical and horizontal loads.

A number of studies on dome analysis, based on kinematical approaches and considering the effect of earthquakes through collapse mechanisms, can be found in the recent literature (see, for example, [Arcidiacono et al. 2015; Zuccaro et al. 2017; Casapulla et al. 2017]). Whilst the present study is focused on structures composed of unilateral material, the seismic Italian codes on the stress verification for structures, such as vaults and domes, refer to materials which can withstand both tension and compression.

The reliability of analyses based on unilateral models, and for which the safety of the structure depends mainly on shape rather than on strength, directly depends on correct geometrical reconstructions. Besides geometry, the knowledge of constructive features, such as masonry stone/brick texture, details concerning the double shell function, and detection of voids inside the wall are essential: the relation between the construction technique and structural behavior is a key point in a structural safety assessment (see [Cennamo et al. 2018b]). Therefore, our analysis has been deepened with the knowledge both on the material of the construction and on the history of the construction.

The stability of historical masonry structures, such as arches, vaults, and domes, is effectively visualized through funicular curves (that is thrust paths of internal forces) carrying the external loads. It is

Keywords: seismic vulnerability, masonry domes.

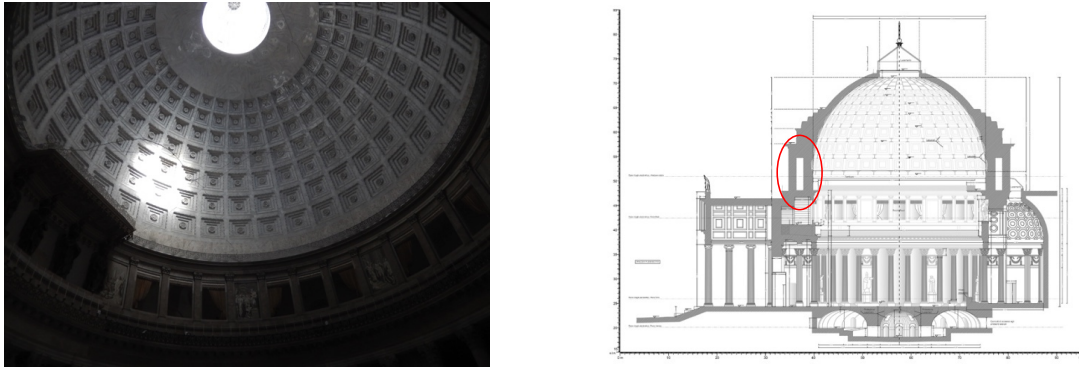


Figure 1. San Francesco di Paola in Naples: interior of the dome with coffers (left) and section of the Basilica by Tecno IN Geosolutions (right).

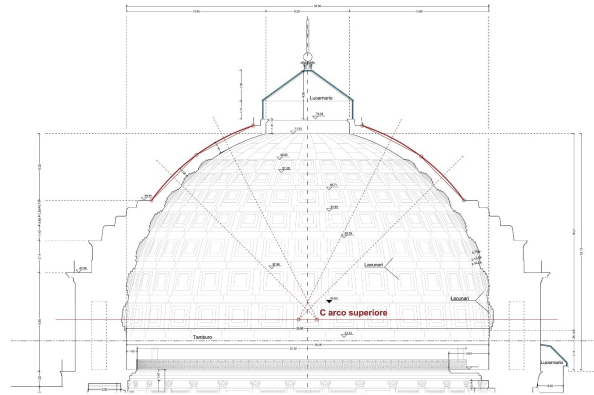


Figure 2. Drawing by the authors. Studies on the geometry of the dome.

their geometry that establishes the capacity to resist loads, both in statics and dynamics [Cennamo and Cusano 2018]. Masonry represents the typological opposite of buildings designed to cope with disasters [Cennamo et al. 2012] and yet, in practice, it often fares well in such emergencies, lasting centuries and millennia undamaged.

The method we propose to analyze domes is applied to a case study, the dome of San Francesco di Paola in Naples, a structural problem already laid out in [Cusano et al. 2017; Cennamo et al. 2017b].

From geognostic surveys carried out jointly with the Laboratory of the Department of Civil Engineering of the University of Salerno using GPR (ground penetrating radar), it can be seen that the brickwork is of good quality (that is, correctly toothed) and compact (that is, with no voids) [Cennamo et al. 2018b].

2. Seismic equivalent static analysis

The main load acting on a dome is the dead load due to the self-weight of the structure and of the superstructure; in normal conditions these loads act vertically.

The undulatory effect of the action of the earthquake ground motion, as a first approximation, can be represented by horizontal forces proportional to the weight. Then the direction of the loads become

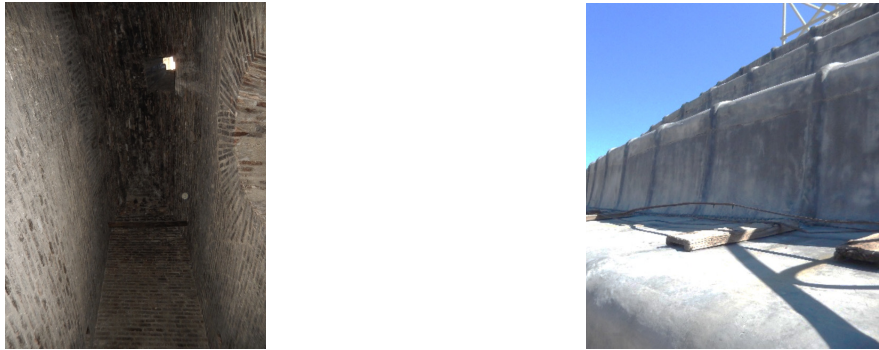


Figure 3. San Francesco di Paola in Naples: particular of the annular aisle in the drum (circled in red in Figure 1, right), whose structure is made of solid brick walls (left) and view of the upper surface of the dome covered with lead (right).

inclined with respect to the vertical: the slope of this direction, that is, the ratio between the horizontal and vertical components, is a measure, usually expressed in g , of the ground acceleration. The approximation inherent to the static approach is two-fold: it neglects both elastic deformation and wave propagation effects. Indeed, the main deformation of a masonry structure arises after a first phase of essentially uniform acceleration, when a mechanism is formed and the structure oscillates, essentially, as a one degree of freedom system. Besides the wave length of earthquake surface waves is at least two or three orders of magnitude bigger than the characteristic dimensions of any conventional masonry structure, that is, the effect of the soil movement is approximately uniform.

2.1. Slicing method. In order to analyze these three-dimensional structures with the slicing method [Cennamo et al. 2017b], the analyst slices the structure, reducing the 3D problem to a combination of 2D problems, for which the structural behavior becomes a combination of arch actions [Block and Ochsendorf 2008]. A dome can be cut with meridian planes, dividing it into arches: the stability condition (safe load theorem) states that a masonry dome which fulfills the theoretical assumptions of a limit analysis [Block and Ochsendorf 2008] is stable if a thrust line can be drawn within this arch section, that is, a possible equilibrium state of compression can be found. If this is the case, then the dome is safe, and will not collapse [Huerta 2001].

3. Case study

3.1. Graphical method. By adopting the slicing technique [Cennamo et al. 2017c], the dome has been divided into slices and the slices into ideal voussoirs. Figure 4 shows a generic slice of the dome, cut between two meridional planes.

With the graphical method, reported in Figure 5, the directions of the loads have been assumed with a slope of 10° with respect to the vertical axis. This corresponds to a value of $\lambda = a/g = 0.176$, a level of acceleration which is above the value of horizontal acceleration prescribed by the Italian regulations in the seismic area of Naples. As can be seen from Figure 5, by using the slicing method, such a level represents the maximum value of horizontal acceleration for which the thrust line can be entirely drawn within the masonry. Therefore, up to an inclination of the loads of 10° , as stated by the fundamental safe

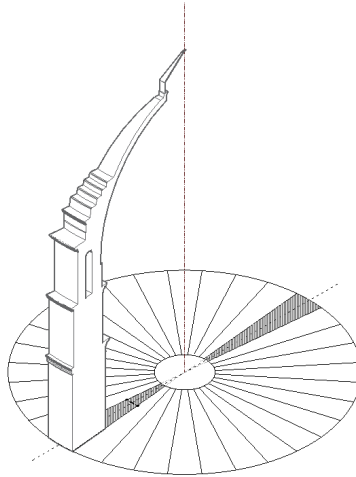


Figure 4. San Francesco di Paola in Naples. In order to study its stability, the dome has been divided into 32 spherical sectors.

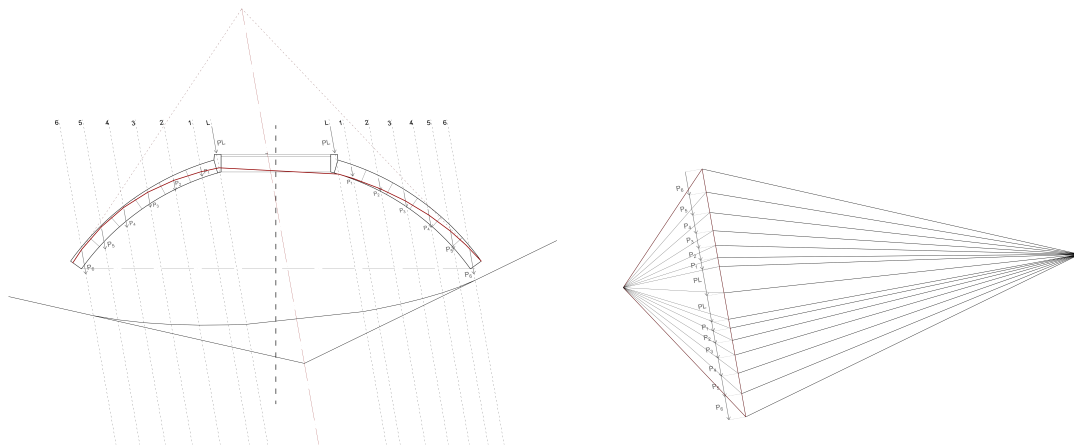


Figure 5. Graphical analysis with the loads inclined of 10° : calculation of the thrust line (left) and force diagram of the loads (right).

theorem [Cennamo et al. 2017b], the structure is stable and collapse cannot occur [Huerta 2004; Cusano et al. \geq 2018].

The peak thrust force per unit length corresponding to $a = 0.176$ g is $H = 304.73$ kN.

Stability of the buttress. The stability of the buttress is studied first by considering the element itself, without the effect of the thrust of the dome. The total weight of the buttress (1679230.11 kN) is applied in the centroid G of the element. The limit value of λ is then $\lambda^\circ = 0.30$ (see Figure 6, left). Considering the effect of the dome, the total force acting on the buttress is depicted in Figure 6, right. For such a force the limit value of λ is 0.175. Therefore, the whole system results in being stable with a value of 10° of inclination ($\lambda = 0.175$).

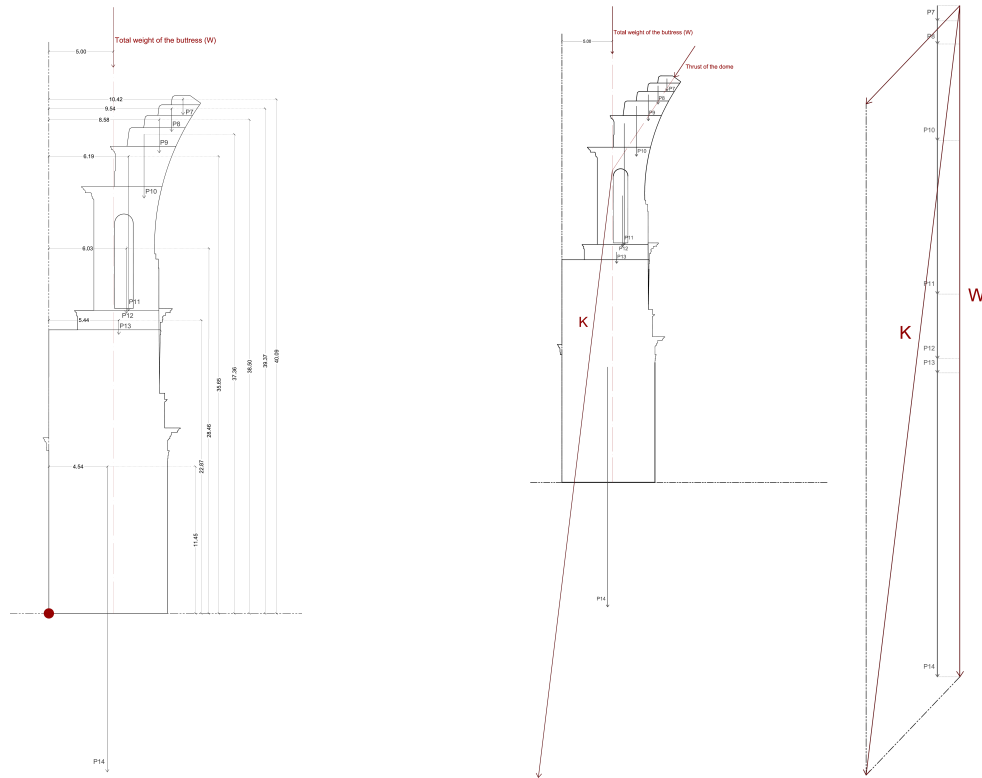


Figure 6. Left: total weight of the buttress and calculation of the limit value of λ without the effect of the thrust of the dome. Right: total force acting on the buttress considering the effect of the dome. Note that the total weight of the buttress (W) is 1679230.11 kN, the thrust of the dome is 339676.96 kN, and the total thrust (K) is 1939734.25 kN.

3.2. Membrane analysis. In this section the equilibrium of the dome is studied with the thrust membrane analysis. The external load is considered lumped on a surface S internal to the masonry, as a distributed load per unit area. The internal stress is also lumped on the surface S , that is, as a generalized membrane stress per unit length concentrated on S .

Under these hypotheses, the equilibrium of the membrane S can be expressed in terms of projected stresses defined on the planform Ω of S [Pucher 1934; Angelillo and Fortunato 2004; Heyman 2012].

In a Cartesian reference $\{0; x_1, x_2, x_3\}$, with the planform Ω contained in the plane $\{0; x_1, x_2\}$, the basic differential equation which rules the equilibrium of the membrane S , written in terms of projected Cartesian stress components $S_{\alpha\beta}$ (the shades of the actual membrane stresses on the planform) with $\alpha, \beta \in \{1, 2\}$ is

$$S_{\alpha\beta} f_{,\alpha\beta} - p_\gamma f_{,\gamma} + p_3 = 0, \quad (1)$$

where p_1, p_2, p_3 are the components of the distributed weight per unit area, f charts the surface S in Monge description, and $f_{,\gamma}, f_{,\alpha\beta}$, are the components of the gradient and of the Hessian of f .

When forces stand parallel to the axis x_3 , then $p_1 = 0$, $p_2 = 0$, and the obtained stresses can be expressed in terms of an Airy's stress potential F :

$$S_{11} = F_{,22}, \quad S_{22} = F_{,11}, \quad S_{12} = S_{21} = -F_{,12}. \quad (2)$$

From (2), it is possible to rewrite the transverse equilibrium equation in the form

$$F_{,22}f_{,11} + F_{,22}f_{,11} - 2F_{,12}f_{,12} - p = 0, \quad (3)$$

where $p = -p_3$. If proper boundary conditions are prescribed at the boundary of Ω , the second order partial differential equation for the stress function F can be solved univocally. To ensure that the dome is in a compression state, the stress function F must be concave (the Hessian of F must be negative semidefinite) and the surface S must be contained within the masonry. In the present study, a convenient form f has been fixed inside the dome and, by solving numerically the transverse equilibrium equation, the corresponding stress F has been found.

By using cylindrical curvilinear coordinates $\{\rho, \vartheta, z\}$, relations (2) and (3) can be rewritten in the forms

$$S_{\rho\rho} = \frac{1}{\rho}F_{,\rho} + \frac{1}{\rho^2}F_{,\vartheta\vartheta}, \quad S_{\vartheta\vartheta} = F_{,\rho\rho}, \quad S_{12} = S_{21} = -\left(\frac{1}{\rho}F_{,\vartheta}\right), \quad (4)$$

$$\left(\frac{1}{\rho}F_{,\rho} + \frac{1}{\rho^2}F_{,\rho\rho}\right)f_{,\rho\rho} + F_{,\rho\rho}\left(\frac{1}{\rho}f_{,\rho} + \frac{1}{\rho^2}f_{,\vartheta\vartheta}\right) - 2\left(\frac{1}{\rho}F_{,\vartheta}\right)_{,\rho}\left(\frac{1}{\rho}f_{,\vartheta}\right)_{,\rho} - p = 0. \quad (5)$$

In the particular case in which axial symmetry of the load and of the boundary conditions is present, the functions F , f depend on ρ only, and (4), (5) reduce to the simple forms

$$S_{\rho\rho} = \frac{1}{\rho}F_{,\rho}, \quad S_{\vartheta\vartheta} = F_{,\rho\rho}, \quad S_{12} = S_{21} = 0, \quad (6)$$

$$\left(\frac{1}{\rho}F_{,\rho}\right)f_{,\rho\rho} + F_{,\rho\rho}\left(\frac{1}{\rho}f_{,\rho}\right) - p = 0. \quad (7)$$

The transverse equilibrium equation (7) can be easily solved numerically after becoming an ordinary differential equation for F .

By making the aforesaid simplifications on the effect of the seismic actions, that is, by considering that the structure is rigid and is rigidly connected to the soil, calling ρ the mass density of the material and a the given acceleration of the soil, the body load per unit volume acting on the structure consists of a vertical component ρg and of a horizontal component ρa . It is possible to estimate the level of ground acceleration that the structure can sustain by considering increasing values of the horizontal load component and by detecting, for any such value, a stress regime that is balanced with the loads and within the limits of the material [De Piano et al. 2017; Cennamo and Fiore 2013].

When reaching its limit horizontal acceleration, the structure forms a mechanism composed of rigid blocks articulated among each other, and a dynamic motion of the structure, different from that of the soil, begins. In the present paper, the study is restricted to the dynamic phase which precedes the formation of such a mechanism.

3.3. Vertical and slanted loads. Considering a horizontal component ρa of the given forces, the loads are no longer purely vertical and axial symmetry relative to the z axis is lost, but the loads can be

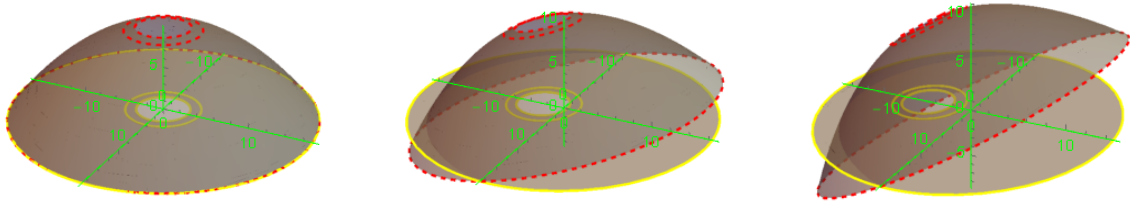


Figure 7. Rotated shapes for $a = 0.000 \text{ g}$, $\alpha = 0^\circ$ (left); $a = 0.268 \text{ g}$, $\alpha = 15^\circ$ (middle); and $a = 0.577 \text{ g}$, $\alpha = 30^\circ$ (right).

approximated as parallel; thus, the dome equilibrium can be given again by (8), rewritten in a Cartesian reference system in which the axes z and y are rotated about the x axis of an angle $\alpha = \arctan(a/g)$.

On the plane of the rotated axes x , y , the planform Ω becomes the projection in the rotated z direction of the ring of internal radius $r_i = 4.20 \text{ m}$ and external radius $r_e = 16.95 \text{ m}$.

The transverse equilibrium equation (that is, a second-order PDE in the unknown scalar function F) is rewritten below in Cartesian:

$$F_{,22}f_{,11} + F_{,22}f_{,11} - 2F_{,12}f_{,12} - p = 0. \quad (8)$$

Such a differential equation for F , approximated variationally, is solved numerically with the package for approximate PDE solutions in the program Mathematica.

Taking into account that in the case of a dome with an oculus where the stress must be zero at the internal rim, the boundary conditions are two: the first of Dirichlet type ($F = 0$), and the second of Neumann type ($dF/dn = 0$), both prescribed at the internal boundary. Consequently, an iterative shooting method has been adopted to solve the problem by imposing boundary conditions in the form of a Neumann homogeneous condition at the internal rim and of a sequence of Dirichlet boundary conditions at the external boundary, until the value of F at the internal boundary was approximately zero. In the analysis, three values of $a = \lambda g$, and the corresponding angles of rotation $\alpha = \arctan(\lambda)$, have been considered:

$$a = 0.000 \text{ g}, \quad \alpha = 0^\circ,$$

$$a = 0.268 \text{ g}, \quad \alpha = 15^\circ,$$

$$a = 0.577 \text{ g}, \quad \alpha = 30^\circ.$$

In the first case the loads are vertical.

Figure 7 illustrates the rotated shapes, corresponding to the three analyzed cases, and the corresponding distributed loads per unit projected area.

In Figure 8, the shape adopted for the membrane and a comparison of the shape of the membrane with the extrados and intrados surfaces in a axial section of the dome are shown in Figure 8.

In Figure 9, the solutions for the three cases in terms of stress potential are shown as 3D plots.

Note that, with the maximal horizontal acceleration that we consider $a = 0.577 \text{ g}$, small tractions begin to appear along the “upwind” side of the outer boundary. These tensile stresses could be easily removed by concavifying a small part of the stress surface F , and adapting the membrane surface at the same location, by solving (8) for f .

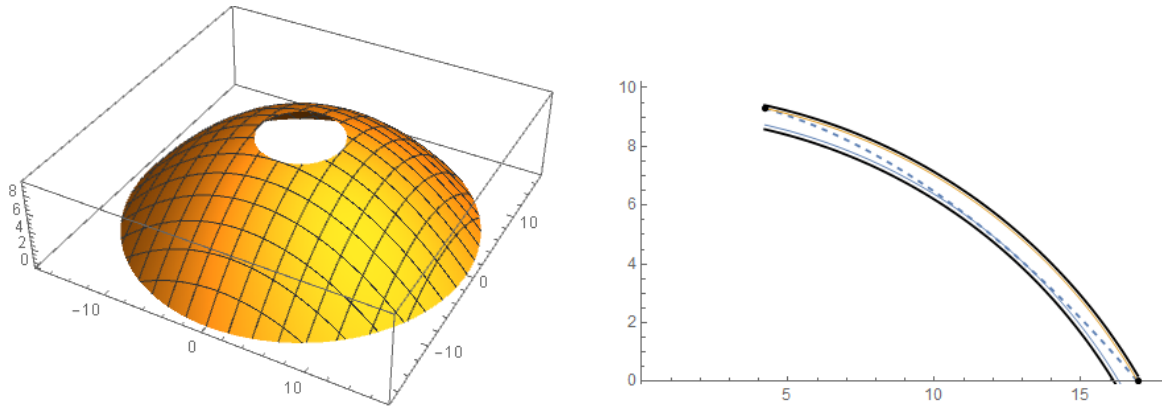


Figure 8. Paraboloid S : sections (left) and membrane surface (dotted), extrados and intrados surfaces (thick lines, right); the light gray lines denote the traces of the spheres tangent to the paraboloid.

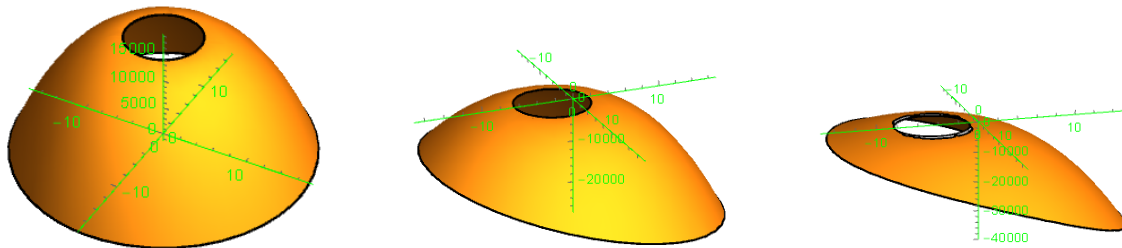


Figure 9. 3D plots of the stress function for the three cases: $a = 0.000$ g, $\alpha = 0^\circ$ (left); $a = 0.268$ g, $\alpha = 15^\circ$ (middle); and $a = 0.577$ g, $\alpha = 30^\circ$ (right).

	$a = 0.000$ g	$a = 0.268$ g	$a = 0.577$ g
H	175.4 kN/m	245.7 kN/m	334.1 kN/m
σ_{\max}	0.375 MPa	0.416 MPa	0.545 MPa

Table 1. Maximum thrust force per unit length and maximum negative stress.

The stress state represented in Figure 9 (right) can be accepted as statically admissible. In Table 1, the estimates of the peak thrust force per unit length H and of the maximum negative stress σ_{\max} , obtained in the three cases, are reported.

The level lines of the maximal and minimal principal stresses and the isostatic lines are reported in Figure 10 for the three cases.

The graphical analysis performed in Section 3.1 shows that the value $\lambda = 0.176$ is already at the limit state of rocking for the buttress (see Figure 6). Therefore, this improved value of the horizontal force multiplier is actually ineffective with regards to the stability of the dome-buttress aggregate.

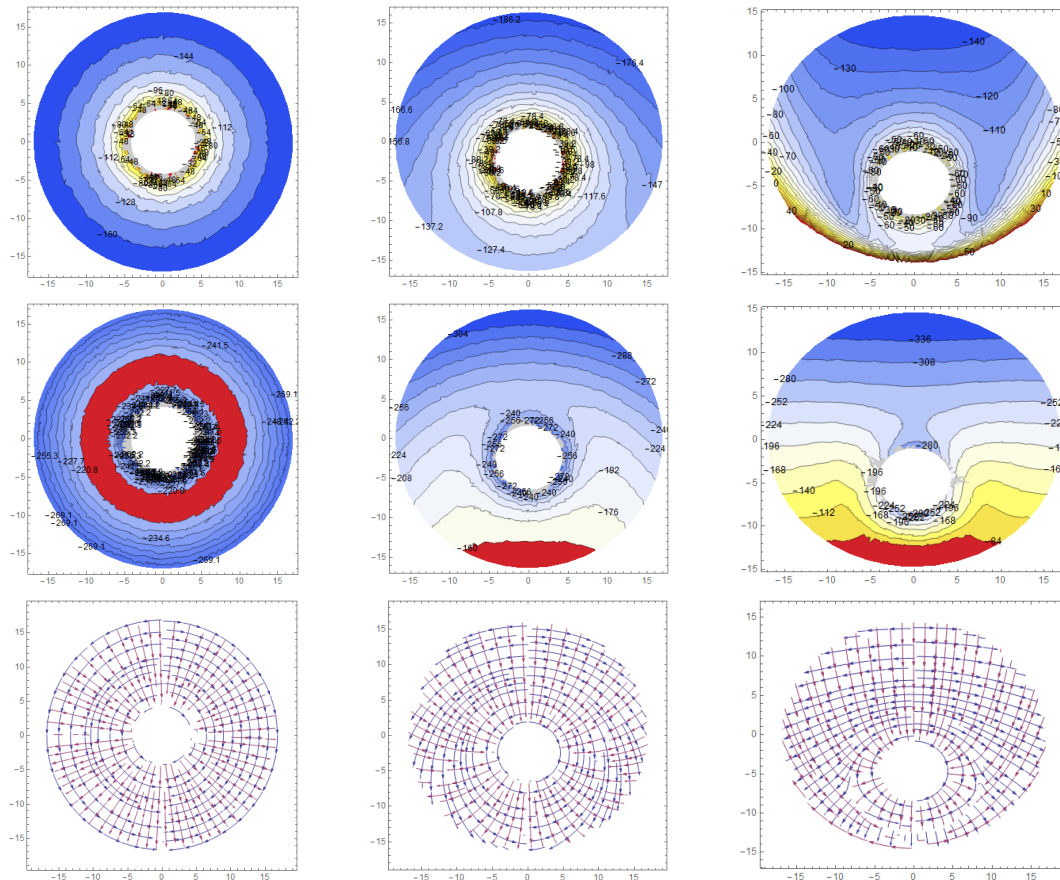


Figure 10. Level curves of the maximal and minimal normal stresses and isostatic lines trajectories for the three cases: $a = 0.000$ g, $\alpha = 0^\circ$ (left column); $a = 0.268$ g, $\alpha = 15^\circ$ (middle column); and $a = 0.577$ g, $\alpha = 30^\circ$ (right column).

4. Conclusions

In a recent work on the Dome of San Francesco di Paola by the same authors (see [Cennamo et al. 2017a; 2018a]) the stability of the dome under vertical loads was discussed by using both the kinematic theorem and the safe theorem of limit analysis.

The aim of this further study is to assess the stability under horizontal actions. The horizontal force capacity of the dome-buttress system can be evaluated through a tilting test, that is, by rotating the structure about a horizontal axis (say the y axis) until the collapse load is reached. The aim of the present work is to determine the limit value of the dome inclination for which the masonry is still entirely compressed, and to assess the buttress stability.

The tilting test was simulated by rotating the body forces of an angle α and studying first the effect of tilting on the sole dome with two different methods, the graphical “slicing” method and the thrust membrane analysis, obtaining with the first method a limit value of $\alpha = 10^\circ$, and with the second method of $\alpha = 30^\circ$.

By considering the effect of tilting on the dome-buttress structural system, the whole system results in stable up to a value of 10° of inclination. This value corresponds to a value of a/g of 0.175 which is above the value of ground acceleration prescribed by the seismic regulation for the zone of the historical center of Napoli.

References

- [Angelillo and Fortunato 2004] M. Angelillo and A. Fortunato, “Equilibrium of masonry vaults”, pp. 105–111 in *Novel approaches in civil engineering*, edited by M. Frémond and F. Maceri, Lect. Notes Appl. Comput. Mech. **14**, Springer, 2004.
- [Arcidiacono et al. 2015] V. Arcidiacono, G. P. Cimellaro, and J. A. Ochsendorf, “Analysis of the failure mechanisms of the basilica of Santa Maria di Collemaggio during 2009 L’Aquila earthquake”, *Eng. Struct.* **99** (2015), 502–516.
- [Block and Ochsendorf 2008] P. Block and J. Ochsendorf, “Lower-bound analysis of masonry vaults”, pp. 593–600 in *Structural analysis of historic construction* (Bath, UK, 2008), edited by D. D’Ayala and E. Fodde, Proc. Int. Conf. Structural Anal. Historical Constructions **6**, CRC Press, Boca Raton, 2008.
- [Casapulla et al. 2017] C. Casapulla, A. Maione, and L. U. Argiento, “Seismic analysis of an existing masonry building according to the multi-level approach of the Italian guidelines on cultural heritage”, *Ingegneria Sismica* **34**:1 (2017), 40–59.
- [Cennamo and Cusano 2018] C. Cennamo and C. Cusano, “The gothic arcade of Santa Maria Incoronata in Naples: equilibrium of gothic arches”, *Int. J. Masonry Res. Innov.* **3**:2 (2018), 92–107.
- [Cennamo and Fiore 2013] C. Cennamo and M. D. Fiore, “Best practice of structural retrofit: the SS. Rosario Church in Gesualdo, Italy”, *Int. J. Disaster Resilience in the Built Environment* **4** (2013), 215–235.
- [Cennamo et al. 2012] C. Cennamo, G. M. Cennamo, and B. Chiaia, “Robustness-oriented design of a panel-based shelter system in critical sites”, *J. Architect. Engin.* **18**:2 (2012), 123–139.
- [Cennamo et al. 2017a] C. Cennamo, M. Angelillo, and C. Cusano, “Structural failures due to anthropogenic sinkholes in the urban area of Naples and the effect of a FRP retrofitting”, *Compos. B Eng.* **108** (2017), 190–199.
- [Cennamo et al. 2017b] C. Cennamo, C. Cusano, and M. Angelillo, “The neoclassical dome of San Francesco di Paola in Naples: a study on form and stability”, pp. 1439–1448 in *Proc. 23rd Conf. Italian Association of Theoretical and Applied Mechanics* (Salerno, 2017), edited by L. Ascione et al., Univ. Salerno, 2017.
- [Cennamo et al. 2017c] C. Cennamo, C. Cusano, and L. Guerriero, “The slicing technique for the evaluation of the formal efficiency: a comparative study”, pp. 1543–1554 in *Proc. 23rd Conf. Italian Association of Theoretical and Applied Mechanics* (Salerno, 2017), edited by L. Ascione et al., Univ. Salerno, 2017.
- [Cennamo et al. 2018a] C. Cennamo, C. Cusano, and M. Angelillo, “On the statics of large domes: a static and kinematic approach for San Francesco di Paola in Naples”, pp. 504–517 in *Proc. 10th Int. Masonry Conference* (Milan, 2018), 2018.
- [Cennamo et al. 2018b] C. Cennamo, C. Cusano, A. Fortunato, and M. Angelillo, “A study on form and seismic vulnerability of the dome of San Francesco di Paola in Naples”, *Ingegneria Sismica* **35**:1 (2018), 88–108.
- [Cusano et al. 2017] C. Cusano, C. Cennamo, and M. Angelillo, “Estabilidad en el neoclásico napolitano y vulnerabilidad sísmica de la cúpula de San Francisco de Paula [sic] en Nápoles”, pp. 399–406 in *Congreso Internacional Hispanoamericano de Historia de la Construcción, II* (Donostia/San Sebastián, 2017), edited by S. Huerta et al., Inst. Juan de Herrera, Madrid, 2017.
- [Cusano et al. ≥ 2018] C. Cusano, C. Cennamo, and M. Angelillo, “A limit analysis approach for masonry domes: the basilica of San Francesco di Paola in Naples”, *Int. J. Masonry Res. Innov.* **4**:3, 227–242.
- [De Piano et al. 2017] M. De Piano, M. Modano, G. Benzoni, V. P. Berardi, and F. Fraternali, “A numerical approach to the mechanical modeling of masonry vaults under seismic loading”, *Ingegneria Sismica* **34**:4 (2017), 103–119.
- [Heyman 1966] J. Heyman, “The stone skeleton”, *Int. J. Solids Struct.* **2**:2 (1966), 249–279.
- [Heyman 2012] J. Heyman, “The membrane analysis of thin masonry shells”, pp. 281–290 in *Nuts & bolts of construction history: culture, technology and society* (Paris, 2012), edited by R. Carvais et al., Proc. Int. Congress on Construction History **4**, Picard, Paris, 2012.

- [Huerta 2001] S. Huerta, “Mechanics of masonry vaults: the equilibrium approach”, pp. 47–69 in *Historical constructions: possibilities of numerical and experimental techniques* (Guimarães, 2001), edited by P. B. Lourenço and P. Roca, Proc. Int. Conf. Structural Anal. Historical Constructions **3**, Univ. Minho, Guimarães, Portugal, 2001.
- [Huerta 2004] S. Huerta, *Arcos, bóvedas y cúpulas: geometría y equilibrio en el cálculo tradicional de estructuras de fábrica*, Inst. Juan de Herrera, Madrid, 2004.
- [Pucher 1934] A. Pucher, “Über der Spannungszustand in gekrümmten Flächen”, *Beton Eisen* **33** (1934), 298–304.
- [Zuccaro et al. 2017] G. Zuccaro, F. Dato, F. Cacace, D. D. De Gregorio, and S. Sessa, “Seismic collapse mechanisms analyses and masonry structures typologies: a possible correlation”, *Ingegneria Sismica* **34**:4 (2017), 121–149.

Received 7 Aug 2018. Accepted 20 Aug 2018.

CONCETTA CUSANO: concetta.cusano@unicampania.it

Department of Architecture and Industrial Design, University of Campania “Luigi Vanvitelli”, Aversa, Italy

CLAUDIA CENNAME: claudia.cennamo@unicampania.it

Department of Architecture and Industrial Design, University of Campania “Luigi Vanvitelli”, Aversa, Italy

MAURIZIO ANGELILLO: mangelillo@unisa.it

Dipartimento di Ingegneria Civile, Università degli Studi di Salerno, Fisciano, Italy

ORTHOTROPIC PLANE BODIES WITH BOUNDED TENSILE AND COMPRESSIVE STRENGTH

MASSIMILIANO LUCCHESI, BARBARA PINTUCCHI AND NICOLA ZANI

The constitutive equation of the nonlinear elastic material with limited tensile and compressive strength has been generalized to account for an orthotropic elasticity tensor. The main difference between this case and the simpler isotropic one is the loss of the coaxiality between the strain and the stress tensor, which leads the principal directions of the stress to become an unknown of the problem. The proposed constitutive equation has been implemented in the finite element code Mady and applied to the study of a masonry panel.

1. Introduction

The mechanical behavior of many elastic materials which are unable to withstand certain types of stress is generally described by the constitutive equation of the so-called normal elastic material [Del Piero 1989]. For these materials the stress \boldsymbol{T} must belong to the stress range, a closed and convex subset \mathcal{K} of all symmetric second-order tensors. Consequently, \boldsymbol{T} does not coincide with the image of the strain \boldsymbol{E} via the elasticity tensor \mathbb{C} , but with the projection on \mathcal{K} of $\mathbb{C}\boldsymbol{E}$ with respect to a suitable scalar product. It is useful to represent the deformation as decomposed additively in an “elastic part” of which the stress is the image through \mathbb{C} and in an “inelastic part” that belongs to the normal cone to \mathcal{K} at \boldsymbol{T} [Lucchesi et al. 2008; Šilhavý 2014; Angelillo 2014]. If the elasticity tensor is (symmetric and) positive definite, for each assigned strain, the solution of the constitutive equation exists and is unique in virtue of the minimum norm theorem. Moreover, this solution can be obtained quite easily when \mathbb{C} is isotropic, as in this case the coaxiality of the stress and strain tensors allows to solve the problem in their common characteristic space.

To date, materials with limited resistance to tensile, compressive, and shear stress have been successfully modeled via this approach [Lucchesi et al. 2018a; 2018b] and many different types of structures such as arches, towers, and churches studied. Indeed, this approach may still be effective for studying certain monumental constructions, where the texture and the properties of masonry are not easily evaluable. Nevertheless, for several applications, a model that accounts for different properties of the material in various directions is undoubtedly more realistic [Lourenço et al. 1998; Berto et al. 2002; Pelà et al. 2011; Lishak et al. 2012].

Since the constraints on the stress are expressed in terms of its invariants, the tensors belonging to the boundary of \mathcal{K} and the elements of the corresponding normal cone are coaxial, even if \mathbb{C} is not isotropic. Of course, in this case there is no coaxiality between the stress and the strain tensor, and the characteristic space of the stress is part of the unknowns of the problem.

As in the isotropic case, there exists a natural partition of Sym , the space of all symmetric second-order tensors, to which corresponds a partition of \mathcal{K} . The belonging of $\mathbb{C}\boldsymbol{E}$ to one of the regions of the partition

Keywords: orthotropic materials, masonry panels.

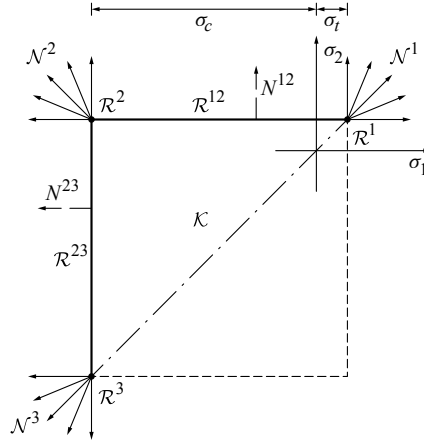


Figure 1. The elastic range.

of Sym implies that its projection (i.e., the associated stress) belongs to the corresponding region of the partition of \mathcal{K} . When the material is orthotropic, however, the assignment of $\mathbb{C}E$ to one of these regions is not immediate and requires a more complex procedure with respect to the isotropic case.

The proposed constitutive model, implemented in the finite element Mady code [Lucchesi et al. 2017], has been applied to the study of a panel subjected firstly to its own weight and to a uniformly distributed vertical load, and then to a progressively increased horizontal displacement imposed at its top.

2. Materials with bounded tensile and compressive strength

Let σ_t and σ_c be two nonnegative constants and \mathbf{I} the identity tensor. Consider a plane stress state for a material whose stress tensor \mathbf{T} must belong to the closed and convex set

$$\mathcal{K} = \{\mathbf{T} \in \text{Sym} : \mathbf{T} - \sigma_t \mathbf{I} \in \text{Sym}^-, \mathbf{T} + \sigma_c \mathbf{I} \in \text{Sym}^+\},$$

where Sym^- and Sym^+ are the cones of the seminegative and semipositive definite elements of Sym , respectively. The following regions make up a partition of the boundary $\partial\mathcal{K}$ of \mathcal{K} (Figure 1):

$$\begin{aligned} \mathcal{R}^1 &= \{\sigma_t \mathbf{I}\}, & \mathcal{R}^2 &= \{\mathbf{T} \in \text{Sym} : \text{tr } \mathbf{T} = -\sigma_c + \sigma_t, \det \mathbf{T} = -\sigma_c \sigma_t\}, & \mathcal{R}^3 &= \{-\sigma_c \mathbf{I}\}, \\ \mathcal{R}^{12} &= \{\mathbf{T} \in \text{Sym} : -\sigma_c + \sigma_t < \text{tr } \mathbf{T} < 2\sigma_t, \gamma^{12}(\mathbf{T}) = -\det(\mathbf{T} - \sigma_t \mathbf{I}) = 0\}, \end{aligned}$$

and

$$\mathcal{R}^{23} = \{\mathbf{T} \in \text{Sym} : -2\sigma_c < \text{tr } \mathbf{T} < \sigma_t - \sigma_c, \gamma^{23}(\mathbf{T}) = -\det(\mathbf{T} + \sigma_c \mathbf{I}) = 0\}.$$

Then, if $\mathbf{T} \in \mathcal{R}^{12}$, σ_t is principal stress, while if $\mathbf{T} \in \mathcal{R}^{23}$, $-\sigma_c$ is principal stress. Moreover, if σ denotes the other principal value of \mathbf{T} , in both cases it holds that

$$-\sigma_c < \sigma < \sigma_t.$$

By noting that, in view of the Hamilton–Cayley theorem, this results in

$$\gamma^{12}(\mathbf{T}) = -\sigma_t^2 + \sigma_t \text{tr } \mathbf{T} - \frac{1}{2}((\text{tr } \mathbf{T})^2 - \|\mathbf{T}\|^2)$$

and

$$\gamma^{23}(\mathbf{T}) = -\sigma_c^2 - \sigma_c \operatorname{tr} \mathbf{T} - \frac{1}{2}((\operatorname{tr} \mathbf{T})^2 - \|\mathbf{T}\|^2)$$

and, moreover,

$$D\gamma^{12}(\mathbf{T}) = \mathbf{T} + (\sigma_t - \operatorname{tr} \mathbf{T})\mathbf{I}, \quad D\gamma^{23}(\mathbf{T}) = \mathbf{T} - (\sigma_c + \operatorname{tr} \mathbf{T})\mathbf{I}$$

and

$$\|\mathbf{T} + (\sigma_t - \operatorname{tr} \mathbf{T})\mathbf{I}\| = 2\sigma_t - \operatorname{tr} \mathbf{T}, \quad \|\mathbf{T} - (\sigma_c + \operatorname{tr} \mathbf{T})\mathbf{I}\| = 2\sigma_c + \operatorname{tr} \mathbf{T},$$

the outward unit normal vectors to \mathcal{K} at \mathcal{R}^{12} and \mathcal{R}^{23} are

$$\mathbf{N}^{12} = \frac{\mathbf{T} + (\sigma_t - \operatorname{tr} \mathbf{T})\mathbf{I}}{2\sigma_t - \operatorname{tr} \mathbf{T}} \quad \text{and} \quad \mathbf{N}^{23} = \frac{\mathbf{T} - (\sigma_c + \operatorname{tr} \mathbf{T})\mathbf{I}}{2\sigma_c + \operatorname{tr} \mathbf{T}}$$

respectively. It is worth observing that \mathbf{N}^{12} and \mathbf{N}^{23} commute with the corresponding stress, so that they have the same characteristic space.

Moreover, it is easy to verify that the normal cones to \mathcal{K} at \mathcal{R}^1 , \mathcal{R}^2 , and \mathcal{R}^3 are respectively

$$\mathcal{N}^1 = \operatorname{Sym}^+, \quad \mathcal{N}^2 = \{N \in \operatorname{Sym} : N = \alpha N^{12} - \omega N^{23}, \alpha \geq 0, \omega \geq 0\}, \quad \mathcal{N}^3 = \operatorname{Sym}^-.$$

Let \mathbb{C} be the elasticity tensor, which is hypothesized to be symmetric and positive definite and \mathbf{E} the assigned strain tensor. Moreover, let $\|\bullet\|_E$ be the energy norm, defined in Sym by $\|\mathbf{S}\|_E^2 = \mathbf{S} \cdot \mathbb{C}^{-1}\mathbf{S}$. In order to determine $\mathbf{T} \in \mathcal{K}$ having the minimum distance from $\mathbb{C}\mathbf{E}$ with respect to $\|\bullet\|_E$, let us denote $\mathbf{E}^e = \mathbb{C}^{-1}\mathbf{T}$ and $\mathbf{E}^a = \mathbf{E} - \mathbf{E}^e$ so that

$$\mathbf{T} = \mathbb{C}[\mathbf{E} - \mathbf{E}^a].$$

If $\mathbb{C}\mathbf{E} \in \mathcal{K}$ then the response of the material is linear elastic, i.e.,

$$\mathbf{E}^a = \mathbf{0} \quad \text{and} \quad \mathbf{T} = \mathbb{C}\mathbf{E}.$$

Otherwise, it is necessary to consider the partition of $\operatorname{Sym} \setminus \mathcal{K}$ in the five regions specified below, as the stress depends on which region contains $\mathbb{C}\mathbf{E}$.

(i) $\mathbb{C}\mathbf{E} \in \mathcal{T}^1$ if $\mathbf{E} - \sigma_t \mathbb{C}^{-1}\mathbf{I} \in \mathcal{N}^1$, i.e., $\det(\mathbf{E} - \sigma_t \mathbb{C}^{-1}\mathbf{I}) \geq 0$ and $\operatorname{tr}(\mathbf{E} - \sigma_t \mathbb{C}^{-1}\mathbf{I}) \geq 0$, then

$$\mathbf{E}^a = \mathbf{E} - \sigma_t \mathbb{C}^{-1}\mathbf{I} \quad \text{and} \quad \mathbf{T} = \sigma_t \mathbf{I}; \quad (2-1)$$

(ii) $\mathbb{C}\mathbf{E} \in \mathcal{T}^{12}$ if there exists $\alpha > 0$ such that $\mathbb{C}[\mathbf{E} - \alpha N^{12}] \in \mathcal{R}^{12}$, then

$$\mathbf{E}^a = \alpha N^{12} \quad \text{and} \quad \mathbf{T} = \mathbb{C}[\mathbf{E} - \alpha N^{12}]; \quad (2-2)$$

(iii) $\mathbb{C}\mathbf{E} \in \mathcal{T}^2$ if there exist $\alpha > 0$ and $\omega > 0$ such that $\operatorname{tr} \mathbb{C}[\mathbf{E} - \alpha N^{12} - \omega N^{23}] = \sigma_t - \sigma_c$ and $\det \mathbb{C}[\mathbf{E} - \alpha N^{12} - \omega N^{23}] = -\sigma_t \sigma_c$, then

$$\mathbf{E}^a = \alpha N^{12} - \omega N^{23} \quad \text{and} \quad \mathbf{T} = \mathbb{C}[\mathbf{E} - \alpha N^{12} + \omega N^{23}]; \quad (2-3)$$

(iv) $\mathbb{C}\mathbf{E} \in \mathcal{T}^{23}$ if there exists $\omega > 0$ such that $\mathbb{C}[\mathbf{E} - \omega N^{23}] \in \mathcal{R}^{23}$, then

$$\mathbf{E}^a = \omega N^{23} \quad \text{and} \quad \mathbf{T} = \mathbb{C}[\mathbf{E} - \omega N^{23}]; \quad (2-4)$$

(v) $\mathbb{C}\mathbf{E} \in \mathcal{T}^3$ if $\mathbf{E} + \sigma_c \mathbb{C}^{-1}\mathbf{I} \in \mathcal{N}^3$, i.e., $\det(\mathbf{E} + \sigma_c \mathbb{C}^{-1}\mathbf{I}) \geq 0$ and $\operatorname{tr}(\mathbf{E} + \sigma_c \mathbb{C}^{-1}\mathbf{I}) \leq 0$, then

$$\mathbf{E}^a = \mathbf{E} + \sigma_c \mathbb{C}^{-1}\mathbf{I} \quad \text{and} \quad \mathbf{T} = -\sigma_c \mathbf{I}. \quad (2-5)$$

3. Orthotropic materials

Let the orthonormal vectors \mathbf{e}_1 and \mathbf{e}_2 define the symmetry directions of a plane orthotropic body [Mallick 1988], with E_{11} , E_{22} and ν_{12} , ν_{21} the corresponding Young and Poisson moduli, respectively. Then the elasticity tensor is

$$\mathbb{C} = \begin{pmatrix} C_{1111} & C_{1122} & 0 \\ C_{1112} & C_{2222} & 0 \\ 0 & 0 & C_{2323} \end{pmatrix}$$

with

$$C_{1111} = \frac{E_{11}}{1 - \nu_{12}\nu_{21}}, \quad C_{1122} = \frac{\nu_{12}E_{22}}{1 - \nu_{12}\nu_{21}} = \frac{\nu_{21}E_{11}}{1 - \nu_{12}\nu_{21}}, \quad C_{2222} = \frac{E_{22}}{1 - \nu_{12}\nu_{21}}, \quad C_{2323} = 2G.$$

By denoting

$$E_{22} = \beta E_{11}, \quad \nu_{21} = \beta \nu_{12}, \quad 2G = \frac{\phi E_{11}}{1 - \beta \nu_{12}^2},$$

and writing E for E_{11} and ν for ν_{12} , we obtain

$$C_{1111} = \frac{E}{1 - \beta \nu^2}, \quad C_{1122} = \frac{\beta \nu E}{1 - \beta \nu^2}, \quad C_{2222} = \frac{\beta E}{1 - \beta \nu^2}, \quad C_{2323} = \frac{\phi E}{1 - \beta \nu^2},$$

that is,

$$\mathbb{C} = \frac{E}{1 - \beta \nu^2} \begin{pmatrix} 1 & \beta \nu & 0 \\ \beta \nu & \beta & 0 \\ 0 & 0 & \phi \end{pmatrix} \quad (3-1)$$

and

$$\mathbb{C}^{-1} = \frac{1}{E} \begin{pmatrix} 1 & -\nu & 0 \\ -\nu & 1/\beta & 0 \\ 0 & 0 & (1 - \beta \nu^2)/\phi \end{pmatrix}. \quad (3-2)$$

In the particular case when $\beta = 1$ and $\phi = 1 - \nu$, the material is isotropic. In order to guarantee that \mathbb{C} is positive definite, it is assumed that

$$E > 0, \quad \phi > 0, \quad \nu \in (0, \frac{1}{2}) \text{ and } \beta \in (0, 1].$$

Let

$$\mathbf{E} = \epsilon_{11} \mathbf{e}_1 \otimes \mathbf{e}_1 + \epsilon_{22} \mathbf{e}_2 \otimes \mathbf{e}_2 + \epsilon_{12} (\mathbf{e}_1 \otimes \mathbf{e}_2 + \mathbf{e}_2 \otimes \mathbf{e}_1)$$

be the assigned strain tensor. Then

$$\mathbb{C}\mathbf{E} = \frac{E}{1 - \beta \nu^2} ((\epsilon_{11} + \beta \nu \epsilon_{22}) \mathbf{e}_1 \otimes \mathbf{e}_1 + \beta (\epsilon_{22} + \nu \epsilon_{11}) \mathbf{e}_2 \otimes \mathbf{e}_2 + \phi \epsilon_{12} (\mathbf{e}_1 \otimes \mathbf{e}_2 + \mathbf{e}_2 \otimes \mathbf{e}_1)), \quad (3-3)$$

so that

$$\begin{aligned} \text{tr } \mathbb{C}\mathbf{E} &= \left(\frac{E}{1 - \beta \nu^2} \right) ((\epsilon_{11} + \beta \nu \epsilon_{22}) + \beta (\epsilon_{22} + \nu \epsilon_{11})), \\ \det \mathbb{C}\mathbf{E} &= \left(\frac{E}{1 - \beta \nu^2} \right)^2 (\beta (\epsilon_{11} + \beta \nu \epsilon_{22}) (\epsilon_{22} + \nu \epsilon_{11}) - \phi^2 \epsilon_{12}^2). \end{aligned}$$

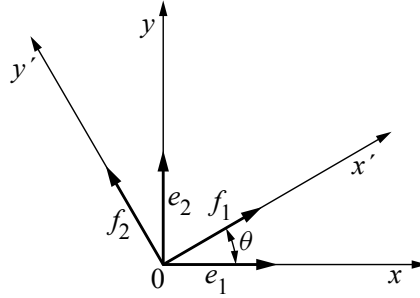


Figure 2. Reference systems.

Moreover, as

$$\mathbb{C}^{-1}\mathbf{I} = \frac{1}{E} \left((1-\nu)\mathbf{e}_1 \otimes \mathbf{e}_1 + \frac{1-\beta\nu}{\beta}\mathbf{e}_2 \otimes \mathbf{e}_2 \right),$$

it holds

$$\text{tr}(\sigma_t \mathbb{C}^{-1}\mathbf{I}) = \frac{\sigma_t(1-2\beta\nu+\beta)}{\beta E}, \quad \det(\sigma_t \mathbb{C}^{-1}\mathbf{I}) = \frac{\sigma_t^2}{\beta E^2}(1-\nu)(1-\beta\nu).$$

and similar expressions are obtained for $-\sigma_c \mathbb{C}^{-1}\mathbf{I}$.

4. Determination of the stress

At any point of $\partial\mathcal{K}$, the stress \mathbf{T} and the elements of the corresponding normal cone can be expressed with respect to an orthonormal basis of their characteristic space, that will be denoted by $\mathbf{f}_1, \mathbf{f}_2$ (Figure 2).

Then, $\mathbf{T} \in \mathcal{R}^{12}$ implies

$$\mathbf{T} = \sigma \mathbf{f}_1 \otimes \mathbf{f}_1 + \sigma_t \mathbf{f}_2 \otimes \mathbf{f}_2, \quad \mathbf{N}^{12} = \mathbf{f}_2 \otimes \mathbf{f}_2 \quad (4-1)$$

and $\mathbf{T} \in \mathcal{R}^{23}$ implies

$$\mathbf{T} = -\sigma_c \mathbf{f}_1 \otimes \mathbf{f}_1 + \sigma \mathbf{f}_2 \otimes \mathbf{f}_2, \quad \mathbf{N}^{23} = -\mathbf{f}_1 \otimes \mathbf{f}_1 \quad (4-2)$$

Let $\theta \in \left[-\frac{\pi}{2}, \frac{\pi}{2}\right]$ be the angle between the vectors \mathbf{e}_1 and \mathbf{f}_1 , with $\mathbf{e}_1 \wedge \mathbf{e}_2 = \mathbf{e}_1 \wedge \mathbf{f}_1 / |\mathbf{e}_1 \wedge \mathbf{f}_1|$, so that

$$\mathbf{f}_1 \cdot \mathbf{e}_1 = \mathbf{f}_2 \cdot \mathbf{e}_2 = \cos \theta, \quad \mathbf{f}_1 \cdot \mathbf{e}_2 = -\mathbf{f}_2 \cdot \mathbf{e}_1 = \sin \theta$$

from which

$$\mathbf{f}_1 \otimes \mathbf{f}_1 = \frac{1}{1+t^2} (\mathbf{e}_1 \otimes \mathbf{e}_1 + t(\mathbf{e}_1 \otimes \mathbf{e}_2 + \mathbf{e}_2 \otimes \mathbf{e}_1) + t^2 \mathbf{e}_2 \otimes \mathbf{e}_2) \quad (4-3)$$

and

$$\mathbf{f}_2 \otimes \mathbf{f}_2 = \frac{1}{1+t^2} (t^2 \mathbf{e}_1 \otimes \mathbf{e}_1 - t(\mathbf{e}_1 \otimes \mathbf{e}_2 + \mathbf{e}_2 \otimes \mathbf{e}_1) + \mathbf{e}_2 \otimes \mathbf{e}_2), \quad (4-4)$$

with $t = \tan \theta$. The expressions of \mathbf{T} , \mathbf{N}^{12} , \mathbf{N}^{23} , $\mathbb{C}\mathbf{N}^{12}$, and $\mathbb{C}\mathbf{N}^{23}$ with respect to the basis $\mathbf{e}_1, \mathbf{e}_2$ can now be deduced by (4-1)–(4-4), and (3-1). If $\mathbf{T} \in \mathcal{R}^{12}$, then

$$\begin{aligned} \mathbf{T} &= \frac{1}{1+t^2} \left((\sigma + \sigma_t t^2) \mathbf{e}_1 \otimes \mathbf{e}_1 + t(\sigma - \sigma_t)(\mathbf{e}_1 \otimes \mathbf{e}_2 + \mathbf{e}_2 \otimes \mathbf{e}_1) + (\sigma t^2 + \sigma_t) \mathbf{e}_2 \otimes \mathbf{e}_2 \right), \\ \mathbf{N}^{12} &= \frac{1}{1+t^2} (t^2 \mathbf{e}_1 \otimes \mathbf{e}_1 - t(\mathbf{e}_1 \otimes \mathbf{e}_2 + \mathbf{e}_2 \otimes \mathbf{e}_1) + \mathbf{e}_2 \otimes \mathbf{e}_2), \end{aligned} \quad (4-5)$$

and, with the help of (3-3), the components of the stress can be deduced from the equation $\mathbf{T} = \mathbb{C}\mathbf{E} - \alpha\mathbb{C}\mathbf{N}^{12}$, as functions of α , σ and t :

$$T_{11} = \frac{\sigma + \sigma_t t^2}{1 + t^2} = \frac{E}{1 - \beta v^2} \left(\epsilon_{11} + \beta v \epsilon_{22} - \alpha \frac{t^2 + \beta v}{1 + t^2} \right), \quad (4-6)$$

$$T_{22} = \frac{\sigma t^2 + \sigma_t}{1 + t^2} = \frac{E}{1 - \beta v^2} \left(\beta(\epsilon_{22} + v\epsilon_{11}) - \alpha \frac{\beta(1 + vt^2)}{1 + t^2} \right), \quad (4-7)$$

$$T_{12} = \frac{(\sigma - \sigma_t)t}{1 + t^2} = \frac{\phi E}{1 - \beta v^2} \left(\epsilon_{12} + \frac{\alpha t}{1 + t^2} \right). \quad (4-8)$$

If $\mathbf{T} \in \mathcal{R}^{23}$, then

$$\begin{aligned} \mathbf{T} &= \frac{1}{1 + t^2} ((\sigma t^2 - \sigma_c) \mathbf{e}_1 \otimes \mathbf{e}_1 - t(\sigma_c + \sigma)(\mathbf{e}_1 \otimes \mathbf{e}_2 + \mathbf{e}_2 \otimes \mathbf{e}_1) + (\sigma - \sigma_c t^2) \mathbf{e}_2 \otimes \mathbf{e}_2), \\ \mathbf{N}^{23} &= -\frac{1}{1 + t^2} (\mathbf{e}_1 \otimes \mathbf{e}_1 + t(\mathbf{e}_1 \otimes \mathbf{e}_2 + \mathbf{e}_2 \otimes \mathbf{e}_1) + t^2 \mathbf{e}_2 \otimes \mathbf{e}_2) \end{aligned} \quad (4-9)$$

and the components of the stress, deduced from $\mathbf{T} = \mathbb{C}\mathbf{E} - \omega\mathbb{C}\mathbf{N}^{23}$, are

$$T_{11} = \frac{\sigma t^2 - \sigma_c}{1 + t^2} = \frac{E}{1 - \beta v^2} \left(\epsilon_{11} + \beta v \epsilon_{22} + \omega \frac{1 + \beta v t^2}{1 + t^2} \right), \quad (4-10)$$

$$T_{22} = \frac{\sigma - \sigma_c t^2}{1 + t^2} = \frac{E}{1 - \beta v^2} \left(\beta(\epsilon_{22} + v\epsilon_{11}) + \omega \frac{\beta(t^2 + v)}{1 + t^2} \right), \quad (4-11)$$

$$T_{12} = -\frac{(\sigma + \sigma_c)t}{1 + t^2} = \frac{\phi E}{1 - \beta v^2} \left(\epsilon_{12} + \frac{\omega t}{1 + t^2} \right). \quad (4-12)$$

It is worth noting that, by taking into account that $\alpha > 0$, $\omega > 0$ and $\sigma - \sigma_t < 0$, $-(\sigma + \sigma_c) < 0$, from (4-8) and (4-12), it follows that $\epsilon_{12} = 0$ if and only if $t/(1 + t^2) = 0$, i.e., $\theta = 0$ or $\theta = \frac{\pi}{2}$. Otherwise, t and ϵ_{12} must have opposite sign.

From (4-6) and (4-7), α and σ can be determined easily, as functions of t :

$$\alpha = \frac{(1 + t^2)[t^2(\beta v \epsilon_{22} + \epsilon_{11} - \beta(v\epsilon_{11} + \epsilon_{22})) + \bar{\sigma}_t(1 - t^2)(1 - \beta v^2)]}{t^4 - \beta}, \quad (4-13)$$

$$\sigma = E \frac{\beta(1 + t^2)(t^2 \epsilon_{22} - \epsilon_{11}) + \bar{\sigma}_t[\beta v t^4 - t^2(1 - \beta) - \beta v]}{t^4 - \beta}, \quad (4-14)$$

where $\bar{\sigma}_t = \sigma_t/E$. Substituting these expressions in (4-8) gives the algebraic equation

$$\begin{aligned} t^4 + \frac{\beta^2 v^2 (\epsilon_{22} + v \sigma \bar{\sigma}_t) + \beta [-\epsilon_{22}(1 - v\phi) - v \sigma \bar{\sigma}_t (1 + v(1 - \phi))] + \phi \epsilon_{11} + \sigma \bar{\sigma}_t (1 - \phi)}{\phi \epsilon_{12}} t^3 \\ - \frac{\beta v^2 (\epsilon_{11} - \sigma \bar{\sigma}_t (1 - v)) + \beta [-\epsilon_{11}(1 - v\phi) + \phi \epsilon_{22} + \sigma \bar{\sigma}_t (1 - v + \phi v^2)] - \sigma \bar{\sigma}_t \phi}{\phi \epsilon_{12}} t - \beta = 0. \end{aligned} \quad (4-15)$$

Similarly, (4-10) and (4-11) give

$$\omega = \frac{(1 + t^2)[t^2 \beta (v \epsilon_{11} + \epsilon_{22}) - \beta v \epsilon_{22} - \epsilon_{11} - \sigma \bar{\sigma}_c (1 - t^2)(1 - \beta v^2)]}{1 - \beta t^4}, \quad (4-16)$$

and

$$\sigma = E \frac{\beta(1+t^2)(t^2\epsilon_{11} - \epsilon_{22}) - \sigma \bar{\sigma}_c [\beta vt^4 + t^2(1-\beta) - \beta v]}{1 - \beta t^4}, \quad (4-17)$$

with $\bar{\sigma}_c = \sigma_c/E$, from which

$$t^4 + \frac{\beta^2 v^2 (\epsilon_{11} + \bar{\sigma}_c (1-v)) + \beta [-\epsilon_{11} (1-v\phi) + \phi \epsilon_{22} - \sigma \bar{\sigma}_c (1-v + \phi v^2) + \bar{\sigma}_c \phi]}{\beta \phi \epsilon_{12}} t^3 - \frac{\beta (v^2 \epsilon_{22} - \sigma \bar{\sigma}_c v^3) + \beta [-\epsilon_{22} (1-v\phi) - v \sigma \bar{\sigma}_c (-1+v(\phi-1))] + \phi \epsilon_{11} + \sigma \bar{\sigma}_c (1-\phi)}{\beta \phi \epsilon_{12}} t - \frac{1}{\beta} = 0 \quad (4-18)$$

is obtained.

4A. Assignment of $\mathbb{C}E$ to its region. Once the strain E (with $\mathbb{C}E \notin \mathcal{K}$) has been assigned, in order to determine the stress it is necessary to establish which region of the partition of $\text{Sym} \setminus \mathcal{K}$ $\mathbb{C}E$ belongs to. For the regions \mathcal{T}^1 and \mathcal{T}^3 the check is trivial; then, if successful, the inelastic strain and the stress can be obtained by (2-1) and (2-5), respectively.

Otherwise, one can proceed by trial, until the region containing $\mathbb{C}E$ is found. In order to verify whether $\mathbb{C}E$ belongs to region \mathcal{T}^{12} , once that t , α , and σ have been determined from (4-13)–(4-15), the relations $\alpha > 0$ and $-\sigma_c < \sigma < \sigma_t$ must be satisfied. In the same way, to verify whether $\mathbb{C}E$ belongs to \mathcal{T}^{23} , equations (4-16)–(4-18) can be used. If the check is satisfied, the inelastic strain and the stress are given by (2-2) in the first case and by (2-4) in the second.

In regards to \mathcal{T}^2 , it is observed that

$$T = -\sigma_c f_1 \otimes f_1 + \sigma_t f_2 \otimes f_2$$

and a generic element belonging to the normal cone to $\partial\mathcal{K}$ at \mathcal{T}^2 is of the form

$$A = -\omega f_1 \otimes f_1 + \alpha f_2 \otimes f_2$$

with

$$\alpha > 0 \quad \text{and} \quad \omega > 0. \quad (4-19)$$

Then, with the help of (3-2), (4-3), and (4-4), from the equation $E - \mathbb{C}^{-1}T = E^a$ the system

$$\begin{aligned} \epsilon_{11} - \frac{\sigma_t t^2 - \sigma_c - v(\sigma_t - \sigma_c t^2)}{E(1+t^2)} &= \frac{-\omega + \alpha t^2}{1+t^2}, \\ \epsilon_{22} - \frac{\beta v(\sigma_c - \sigma_t t^2) + \sigma_t - \sigma_c t^2}{\beta E(1+t^2)} &= \frac{\alpha - \omega t^2}{1+t^2}, \\ \epsilon_{12} + \frac{(1-\beta v^2)(\sigma_c + \sigma_t)t}{\phi E(1+t^2)} &= \frac{-(\omega + \alpha)t}{(1+t^2)} \end{aligned}$$

is obtained, whose solution allows us to calculate α , ω , and t , and to verify if the condition (4-19) is satisfied. If so, the inelastic strain and the stress are given by (2-3), with N^{12} and N^{23} given by (4-5) and (4-9), respectively.

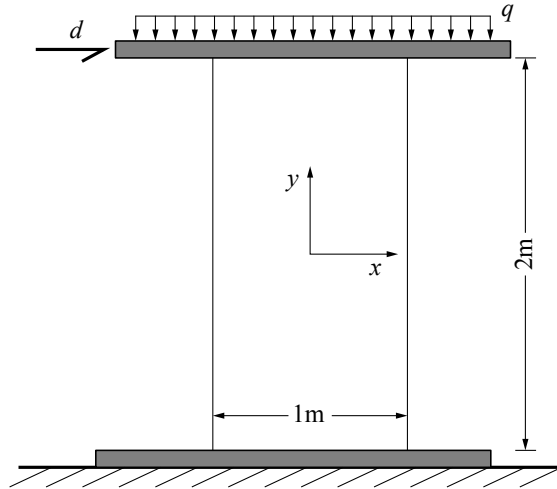


Figure 3. The analyzed masonry panel.

4B. Calculation of the stress derivatives. For the numerical solution of the equilibrium problem with the Newton–Raphson method, it is necessary to know the derivative of the stress with respect to the strain. To this aim, let D_{ijlm} be the derivative of the stress components T_{ij} with respect to the strain components ϵ_{lm} . It is hypothesized the existence of a differentiable function $\hat{t} : \mathbb{R}^3 \rightarrow \mathbb{R}$, such that $t = \hat{t}(\epsilon_{11}, \epsilon_{12}, \epsilon_{22})$, although one does not know its explicit expression. Then

$$D_{ijlm} = \frac{\partial T_{ij}}{\partial \epsilon_{lm}} + \frac{\partial T_{ij}}{\partial t} \frac{\partial \hat{t}}{\partial \epsilon_{lm}}.$$

The derivatives $\partial T_{ij}/\partial \epsilon_{lm}$ and $\partial T_{ij}/\partial t$ can be calculated directly from (4-6)–(4-8) or from (4-10)–(4-12), while in order to calculate $\partial \hat{t}/\partial \epsilon_{lm}$ it is necessary to use the implicit function theorem. For this purpose let $G(\epsilon_{11}, \epsilon_{12}, \epsilon_{22}, t)$ be the left member of (4-15) or (4-18), with $\partial G/\partial t \neq 0$, so that

$$\frac{\partial \hat{t}}{\partial \epsilon_{lm}} = - \frac{\partial G/\partial \epsilon_{lm}}{\partial G/\partial t}.$$

5. Example

The proposed model has been implemented into Mady [Lucchesi et al. 2017], a FEM code developed by the authors. The analysis presented in the following has been conducted by using plane stress four-node isoparametric elements.

Let us consider a masonry wall 2 m height, 1 m wide and 0.1 m thick, which is subjected to a permanent load, consisting of its own weight and a uniform vertical load q , and to a horizontal displacement d incrementally imposed at the top (Figure 3). The mechanical properties assumed for the material are $\nu = 0.1$, $\rho = 1800 \text{ kg/m}^3$, $\sigma_t = 0$, $\sigma_c = 5 \text{ MPa}$, $\Phi = 1 - \nu$. For the vertical load, the values $q_1 = 0.5 \text{ MPa}$ and $q_2 = 1 \text{ MPa}$ have been assumed. For each load case, two further cases have been considered for the Young moduli. In the former, E_x has been assumed equal to 5 GPa while E_y has been varied as shown in Figures 4 and 6; in the second case, E_x has been varied as shown in Figures 5 and 7, whereas $E_y = 5 \text{ GPa}$ has been kept constant.

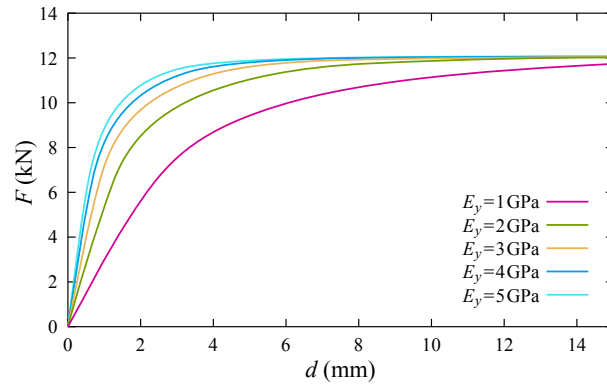


Figure 4. Shear force vs. displacement for $q = 0.5$ MPa, $E_x = 1$ GPa and several values of E_y .

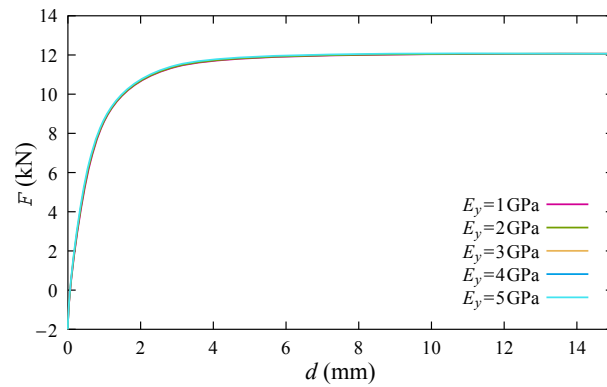


Figure 5. Shear force vs. displacement for $q = 0.5$ MPa, $E_y = 1$ GPa and several values of E_x .

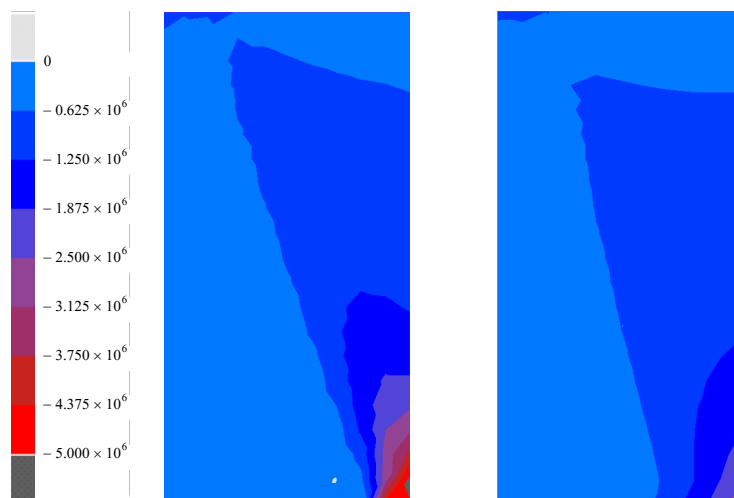


Figure 6. Principal compressive stress for $q = 0.5$ MPa and $d = 5$ mm in two cases. Left: $E_x = E_y = 5$ GPa (isotropic). Right: $E_x = 5$ GPa, $E_y = 1$ GPa.

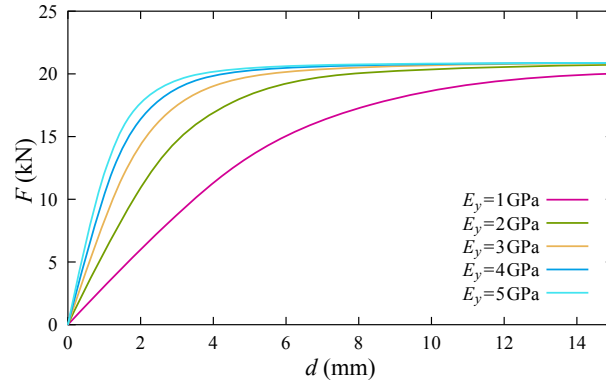


Figure 7. Shear force vs. displacement for $q = 1$ MPa, $E_x = 1$ GPa and several values of E_y .

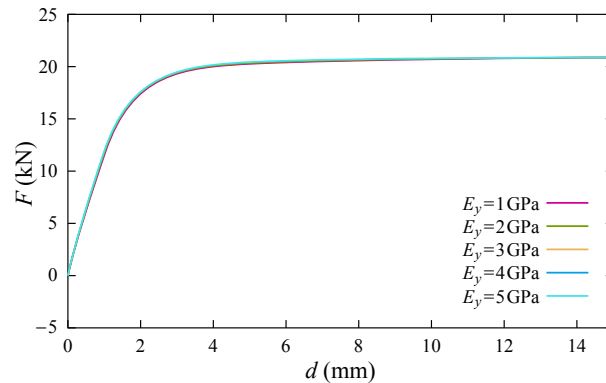


Figure 8. Shear force vs. displacement for $q = 1$ MPa, $E_y = 1$ GPa and several values of E_x .

Figures 4, 5 and Figures 7, 8 show the graphs of the horizontal reaction at the base of the panel as a function of the imposed displacement, for the four cases considered. Their trends confirm a well-known result, i.e., for this load condition, the value of the Young's modulus in the vertical direction affects the stiffness of the panel much more than that in the horizontal direction [Smilovic et al. 2019]. In order to highlight the difference between isotropic and orthotropic behavior, Figure 6 shows the principal compressive stress for $q_1 = 0.5$ MPa and $d = 5$ mm by comparing the case of $E_x = E_y = 5$ MPa (isotropic) and $E_x = 5$ MPa, $E_y = 1$ MPa.

6. Conclusions

The main outcome of the paper is the development of a constitutive model that considers masonry as a nonlinear orthotropic elastic material with bounded tensile and compressive stresses. This approach allows us to describe in a more realistic way the behavior of masonry buildings (which are generally made of a nonisotropic material) and to develop useful nonisotropic damage laws. This latter issue, as well as a more general constitutive equation for orthotropic materials (e.g., those unable to withstand high shear stress) will be the object of a forthcoming paper.

References

- [Angelillo 2014] M. Angelillo, “Practical applications of unilateral models to masonry equilibrium”, pp. 109–210 in *Mechanics of masonry structures*, edited by M. Angelillo, CISM Courses and Lect. **551**, Springer, 2014.
- [Berto et al. 2002] L. Berto, A. Saetta, R. Scotta, and R. Vitaliani, “An orthotropic damage model for masonry structures”, *Int. J. Numer. Methods Eng.* **55**:2 (2002), 127–157.
- [Del Piero 1989] G. Del Piero, “Constitutive equation and compatibility of the external loads for linear elastic masonry-like materials”, *Meccanica (Milano)* **24**:3 (1989), 150–162.
- [Lishak et al. 2012] V. I. Lishak, V. I. Yagust, and D. Z. Yankelevsky, “2-D orthotropic failure criteria for masonry”, *Eng. Struct.* **36** (2012), 360–371.
- [Lourenço et al. 1998] P. B. Lourenço, J. G. Rots, and J. Blaauwendraad, “Continuum model for masonry: parameter estimation and validation”, *J. Struct. Eng. (ASCE)* **124**:6 (1998), 642–652.
- [Lucchesi et al. 2008] M. Lucchesi, C. Padovani, G. Pasquinelli, and N. Zani, *Masonry constructions: mechanical models and numerical applications*, Lecture Notes Appl. Comput. Mech. **39**, Springer, 2008.
- [Lucchesi et al. 2017] M. Lucchesi, B. Pintucchi, and N. Zani, “Modelling masonry structures through the MADY code”, in *2nd International Conference on Recent Advances in Nonlinear Models — Design and Rehabilitation of Structures (CoRASS 2017)*, edited by H. Barros et al., 2017.
- [Lucchesi et al. 2018a] M. Lucchesi, B. Pintucchi, and N. Zani, “Bounded shear stress in masonry-like bodies”, *Meccanica (Milano)* **53**:7 (2018), 1777–1791.
- [Lucchesi et al. 2018b] M. Lucchesi, B. Pintucchi, and N. Zani, “Masonry-like material with bounded shear stress”, *Eur. J. Mech. A Solids* **72** (2018), 329–340.
- [Mallick 1988] P. K. Mallick, *Fiber-reinforced composites*, Dekker, New York, 1988.
- [Pelà et al. 2011] L. Pelà, M. Cervera, and P. Roca, “Continuum damage model for orthotropic materials: application to masonry”, *Comput. Methods Appl. Mech. Eng.* **200**:9-12 (2011), 917–930.
- [Šilhavý 2014] M. Šilhavý, “Mathematics of the masonry-like model and limit analysis”, pp. 29–69 in *Mechanics of masonry structures*, edited by M. Angelillo, CISM Courses and Lect. **551**, Springer, 2014.
- [Smilovic et al. 2019] M. Smilovic, J. Radnic, N. Grgic, and G. Baloevic, “Effect of anisotropy of the masonry on the behaviour of unreinforced and confined masonry walls under ground motion”, pp. 173–186 in *Engineering design applications*, edited by A. Öchsner and H. Altenbach, Adv. Structured Mater. **92**, Springer, 2019.

Received 19 Jul 2018. Revised 6 Feb 2019. Accepted 2 Mar 2019.

MASSIMILIANO LUCCHESI: massimiliano.lucchesi@unifi.it

Department of Civil and Environmental Engineering (DICEA), University of Florence, Florence, Italy

BARBARA PINTUCCHI: barbara.pintucchi@unifi.it

Department of Civil and Environmental Engineering (DICEA), University of Florence, Florence, Italy

NICOLA ZANI: nicola.zani@unifi.it

Department of Civil and Environmental Engineering (DICEA), University of Florence, Florence, Italy

A NO-TENSION ANALYSIS FOR A BRICK MASONRY VAULT WITH LUNETTE

MICHELA MONACO, IMMACOLATA BERGAMASCO AND MICHELE BETTI

A large class of analysis methods has been developed during the last century for the study of masonry structures. Among them, the so-called unilateral no-tension model plays a fundamental role. Starting from the pioneer papers by Heyman in the second half of sixties, a new definition of the safety factor based on the equilibrium of the masonry structure as a no-tension body has been considered. The safety of the structure is mainly determined by its geometry rather than its material strength. The funicular analysis largely used in the 19th century has been improved in light of Heyman's approach to obtain computational methods based on lower-bound solutions. Heyman's hypotheses are the basis of the rigid no-tension continuous approach presented and applied to a barrel vault with lunette in the San Barbaziano church in Bologna. The masonry vault is modelled as a membrane (thrust surface) subjected to compressive stresses only, contained within extrados and intrados surfaces, and carrying uniform applied loads. The geometry of the unilateral membrane, described as an unknown smooth surface, and the associated admissible stress field are determined via a concave stress function necessary for equilibrium and unilateral constraints fulfillment. Special attention has been devoted to the singular stress field arising in the curves at the intersection of the vaults.

1. Introduction

Appropriate and effective analysis methods for the assessment of masonry buildings are a necessary step in the preservation of what is generally defined as "cultural heritage" [Bergamasco et al. 2018]. A suitable calibration of interventions is in fact possible with reliable tools [Sacco et al. 2018]. They should take into account the specificity of the examined buildings, which, in general, presents peculiar aspects due to the presence of various particular geometries like vaults, arches, and isolated columns. Observation of several collapsed stone-block masonry structures, such as the temples at Selinunte and Agrigento, has shown that the major cause of global failure is loss of equilibrium rather than material failure [Como 1992], since in many cases the collapsed blocks are in perfect condition and restoration can be done by rebuilding [Heyman 1970]. This observation applies to masonry arches, vaults, and any other masonry structure that they may be a part of [Moseley 1833; 1860].

The use of arches can be traced back to 3000 BC and the earliest civilizations, in the marshlands of lower Egypt and Mesopotamia. Roman engineers used arches in aqueducts, theaters, amphitheaters, and temples, but perhaps the best structural use of arches is in bridges: the Pons Fabricius and Pons Cestius in Rome (Italy), the Alcantara and Abelterio bridges in Portugal, and the Pons Flavius in Saint Chamas (France) are only a few examples of the Roman solution to the problem of bridging a gap [Hendry 1995]. The same considerations can be applied to the masterpieces of Roman engineering: the masonry vaults. Several of these masonry structures remain in service, despite having been subjected for centuries to a

Keywords: combined masonry vaults, unilateral materials, membrane behaviour, singular stress fields.

heavy regime of environmental conditions and loadings [Gesualdo and Monaco 2010; Buonocore et al. 2014].

Very few masonry arches and vaults have been built in modern times, and knowledge of the related design methods is no longer part of a civil engineer's training [Huerta 2001]. Despite a growing need for rehabilitation and conservation of these structures, understanding of their behaviour has declined during the last century, and the available professional tools for assessing them are in some cases of questionable reliability [Gesualdo et al. 2010; Bartoli et al. 2017].

The equilibrium approach dates back to a small note of Robert Hooke [1676] under the mask of a cipher:

“The true Mathematical and Mechanical form of all manner of Arches for Building, with the true butment necessary to each of them. A Problem which no Architectonick Writer hath ever yet attempted, much less performed”.

The cipher deciphered gives *“Ut pendet continuum flexile sic stabit contiguum rigidum inversum”*. Ever since Hooke's statement, the equilibrium approach has been used to state that if a catenary shape can be included in the thickness of the arch, then the arch is in equilibrium.

Analytical and graphical methods have been applied since then for the analysis of masonry arch structures, although the methods of graphical statics have been the strongest tools used to solve the equilibrium problems of arches and vaults for centuries (for a thorough discussion on this aspect, see [Huerta 2008]). The seminal papers by Heyman [1966; 1977; 1982] gave a new definition of the equilibrium approach, including the analysis of vaulted structures in the general framework of limit analysis, and in particular in that of the safe theorem [Kurrer 2008]. The observation of the very low stress level in the masonry has induced Heyman's three basic hypotheses: infinite compressive strength, null tensile strength, and no sliding among voussoirs. If the masonry arch fulfills these requirements, and the structure is stable, there exists at least one thrust line contained in its cross section. The safety factor can be recognized as the ratio between the actual thickness of the structure and the minimum thickness necessary to contain a line of thrust.

Heyman's hypotheses are the basis of several classes of methods based on the safe theorem [Lucchesi et al. 2012]. Among them, the thrust network analysis (TNA), a methodology initiated by O'Dwyer [1999] and developed mainly by Block [Block 2009; Block and Lachauer 2014], should be mentioned, and it recently has been extended and applied to particular vaulted structures [Fraternali 2010; Marmo and Rosati 2017]. The equilibrium of vaulted structures is examined with reference to a network of thrusts in equilibrium with the applied loads. The same discrete approach has been developed in [Fraternali 2010; 2011], in which a sort of truss structure represents the continuous masonry vault. The stress field is approximated through a network of lumped stresses defined on the truss structure and the corresponding energy is defined at the truss nodes [Fraternali et al. 2014].

The second class of methods makes reference to the definition of a funicular membrane included in the masonry vault. It starts with the Pucher papers [1934; 1937], developed for reinforced concrete shells, and successively extended to masonry structures considered as rigid no-tension materials by Angelillo et al. [2013]. The modelling of masonry as a unilateral material dates back to Heyman's papers, but only recently, thanks to the development of computing efficiency, has it been successfully applied to complex masonry structures [Lucchesi et al. 2007; 2008; Angelillo et al. 2010]. A further list of references is given in [Angelillo et al. 2016; Iannuzzo et al. 2018]. Successive applications have been proposed to

model helical stairs [Angelillo 2015; Gesualdo et al. 2017; Marmo et al. 2018] and combined masonry vaults [Bergamasco et al. 2017].

This paper presents a continuum equilibrium approach for a system of combined vaults. The aim is to determine a compressive thrust surface contained between extrados and intrados of the vault. The constitutive behaviour of the material is assumed as rigid no-tension. A statically admissible stress field (in equilibrium with the applied selfweight, i.e., the only load applied on the vault system) is determined. As a case study the barrel vault with lunette in the San Barbaziano church in Bologna is considered. Particular attention is given to the singular stress field in the form of line Dirac deltas along the intersection curves.

2. Statement of the problem

A masonry vault is a complex structure that can be analytically represented by a spatial domain whose boundaries are the intrados's and extrados's surfaces. The model here schematically illustrated (more details can be found in [Angelillo et al. 2013]) considers the vault as a membrane structure S contained in the domain whose thickness t coincides with the vault's. The problem takes into account two unknowns: the membrane shape S and the stress function F ; the latter is determined by solving an Airy stress problem, as shown in the following. The geometry of the membrane S is given in the Monge form $x_3 = f(x_1, x_2)$. The function $f(x_1, x_2)$ is continuous on the two-dimensional connected definition domain Ω . The material point \mathbf{x} on the membrane S has coordinates defined in the Cartesian reference system coherent with base $\mathbf{B} = \{\mathbf{e}_1, \mathbf{e}_2, \mathbf{e}_3\}$ as

$$\mathbf{x} = \{x_1, x_2, f(x_1, x_2)\}, \quad \{x_1, x_2\} \in \Omega,$$

where Ω is the definition domain whose boundary $\partial\Omega$ is composed of a finite number of closed curves, with unit outer normal \mathbf{n} ; $\{x_1, x_2\}$ are the coordinate components on the projection plane Ω of S ; and $f(x_1, x_2) = x_3$ is the rise of the membrane with $f \in C^0(\Omega)$.

Figure 1 shows the surface with a detailed description of a differential element of the membrane. The loading system is represented by the external forces pressure $\mathbf{q} = \{q_1, q_2, q_3\}$.

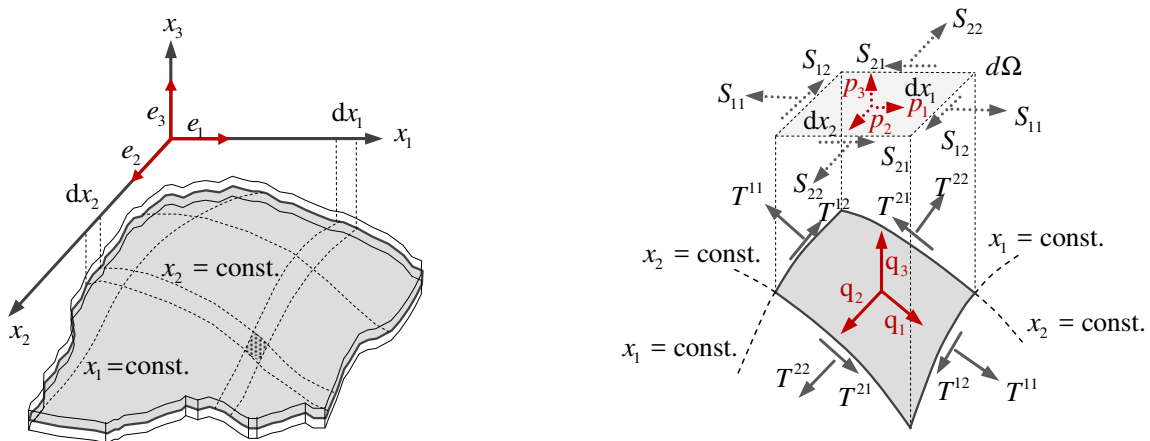


Figure 1. Left: membrane structure. Right: membrane stresses $T^{\alpha\beta}$ and Pucher stresses S_{ij} .

The membrane stress tensor $\mathbf{T} = \{T^{11}, T^{22}, T^{12}\}$ is defined in the covariant vector basis \mathbf{A} tangent to S . Both the covariant \mathbf{A} and the contravariant \mathbf{A}^1 vector bases [Pucher 1934] are reported below:

$$\mathbf{A} = \{\mathbf{a}_1, \mathbf{a}_2, \mathbf{a}_3\} = \begin{bmatrix} 1 & 0 & -f_{,1} \\ 0 & 1 & -f_{,2} \\ f_{,1}/J & f_{,2}/J & -1/J \end{bmatrix}, \quad \mathbf{A}^1 = \{\mathbf{a}^1, \mathbf{a}^2, \mathbf{a}^3\} = \frac{1}{J^2} \begin{bmatrix} 1+f_{,2}^2 & -f_{,1}f_{,2} & -f_{,1} \\ -f_{,1}f_{,2} & 1+f_{,1}^2 & -f_{,2} \\ Jf_{,1} & Jf_{,2} & -J \end{bmatrix}. \quad (1)$$

Here the comma in the subscripts indicates partial differentiation with respect to the variable x_i and $J = \sqrt{1 + f_{,1}^2 + f_{,2}^2}$ is the Jacobian determinant, i.e., the ratio between the differential surface area on S and its projection on the plane $f(x_1, x_2) = 0$.

A surface stress tensor \mathbf{T} is determined for the generalised membrane stress on S and it is defined per unit length of horizontal line element in the covariant base \mathbf{A} as

$$\mathbf{T} = T^{\alpha\beta} \mathbf{a}_\alpha \otimes \mathbf{a}_\beta,$$

where $T^{\alpha\beta}$ are the contravariant components of \mathbf{T} with Einstein summation convention. The problem of equilibrium per unit area gives

$$\frac{\partial}{\partial x_\gamma} (T^{\alpha\beta} \mathbf{a}_\alpha \otimes \mathbf{a}_\beta) \mathbf{a}^\gamma + \mathbf{q} = \mathbf{0}. \quad (2)$$

Introducing the projected stress components $S_{\alpha\beta} = JT^{\alpha\beta}$ (Pucher stresses), after some manipulation, the system of equations (2) in the reference system $\{\mathbf{e}_1, \mathbf{e}_2, \mathbf{m} = \mathbf{a}_3\}$ becomes [Pucher 1934; 1937]

$$S_{11,1} + S_{12,2} + p_1 = 0, \quad S_{21,1} + S_{22,2} + p_2 = 0, \quad S_{\alpha\beta} f_{,\alpha\beta} - p_\gamma f_{,\gamma} + p_3 = 0, \quad (3)$$

where $\mathbf{p} = J\mathbf{q}$ is the pressure on the projected area. The plane stress problem can be recognized in the first two equations of the system (3), so that the solution can be obtained in terms of a single unknown function, i.e., an Airy stress function $F(x_1, x_2)$ so that

$$S_{11} = F_{,22}, \quad S_{22} = F_{,11}, \quad S_{12} = S_{21} = -F_{,12}. \quad (4)$$

The transverse equilibrium in terms of $F(x_1, x_2)$ is expressed by

$$L(F) = F_{,22} f_{,11} + F_{,11} f_{,22} - 2F_{,12} f_{,12} = p, \quad (5)$$

where the vertical force defined per unit horizontal area $\mathbf{p} = \{0, 0, -p\}$ and $L(F)$ has been called the Pucher operator [Flügge and Geyling 1957]. Stress restrictions due to the assumption of masonry material as a rigid no-tension one in the Heyman sense [1966] are assumed. In other words, the generalised stress \mathbf{T} is negative semidefinite and does null work for the corresponding positive semidefinite strain \mathbf{E} :

$$\mathbf{T} \in \text{Sym}^-, \quad \mathbf{E} \in \text{Sym}^+, \quad \mathbf{T} \cdot \mathbf{E} = 0. \quad (6)$$

In terms of the stress function F , the unilateral constraints reduce to the relations

$$F_{,11} + F_{,22} \leq 0, \quad F_{,11} F_{,22} - F_{,12}^2 \geq 0. \quad (7)$$

These correspond to the condition on $F(x_1, x_2)$ to be concave. The only requirement of continuity for F gives as a result the possibility of a folded surface, with discontinuous Pucher stresses defined as a Dirac delta line whose definition domain is the projection Γ of the fold. The Hessian \mathbf{H} of F has a uniaxial



Figure 2. The San Barbaziano church: external view (left) and ground level plan (right).

singular part parallel to the unit vector \mathbf{h} normal to Γ , i.e., it is singular transversely to Γ . Hence the directional derivative of the Airy stress function along \mathbf{h} , namely F_h , has a discontinuity and

$$\mathbf{H}_s = \delta(\Gamma) F_h \mathbf{h} \otimes \mathbf{h}, \quad \mathbf{S}_s = \delta(\Gamma) F_h \mathbf{k} \otimes \mathbf{k}, \quad (8)$$

where \mathbf{H}_s is the singular part of \mathbf{H} , \mathbf{S}_s is that of the Pucher stress, \mathbf{k} is the unit vector tangent to Γ , and $\delta(\Gamma)$ is the unit line Dirac delta on Γ . The fold is concave due to the concavity of F_h . A detailed analysis of the model, together with a thorough discussion on the singular stress functions, is presented in [Angelillo et al. 2013].

3. The case study

The case study is the barrel vault with lunette covering the transept of the San Barbaziano, a brick masonry building at the corner of Via Barberia and Via Cesare Battisti in Bologna. It was built between 1608 and 1612 by Pietro Fiorini and designed to include the remains of a late Middle Age monastery church which did not conform to the canons of the Trent council.

The church is formed by a late Mannerist single nave with eight side chapels belonging to the original church, separated by masonry piers and incorporated in the new building at the ground level.

The higher part of the church consists only of the central nave (45 m in length, 11.60 m in width), with external masonry buttresses corresponding to the separation walls of the lower chapels (Figure 2).

The walls are very slender, considering that the façade, apsis walls, and lateral walls of the ground level chapels are 85 cm thick. The longitudinal walls are 40 cm thick at both levels. The three-bay nave is longitudinally counterpointed by two barrel vaults with lunettes and a central bay with a cross vault (Figure 3). A second cross vault covers the apsis [Colla and Pascale 2015]. Attention has been focussed on the thin brick masonry barrel vaults with lunettes (Figure 4).

The membrane behaviour models with good accuracy the thin masonry vaults (thickness 12.5 cm), whose intrados and extrados are approximated by the graphs of the functions derived by the general

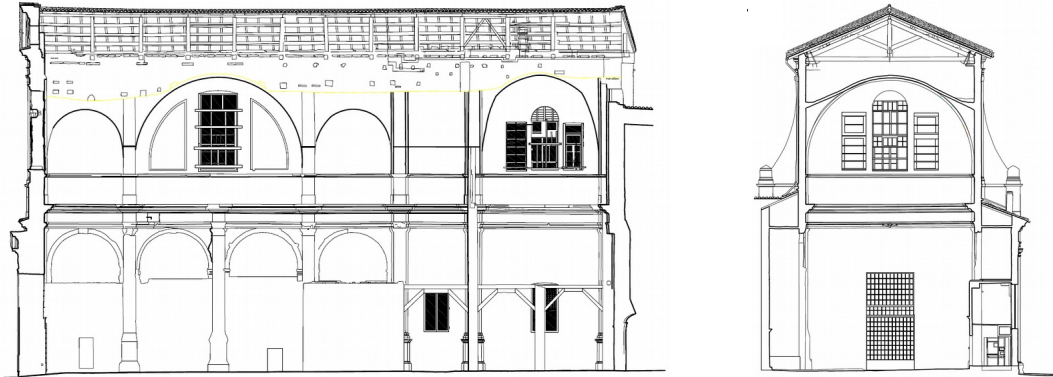


Figure 3. Longitudinal (left) and transversal section (right) of the San Barbaziano church.



Figure 4. Intrados of the barrel vault with lunette in the San Barbaziano church.

surface	coefficients			
main vault intrados	$a = -0.18$	$m = 5.60$		
main vault extrados	$a = -0.14$	$m = 5.73$		
main vault membrane	$a = 1.22 \cdot 10^{-4}$	$d = 3.82 \cdot 10^{-3}$	$g = -0.15$	$m = 5.66$
lunette intrados	$d = -0.35$	$m = 2.80$		
lunette extrados	$d = -0.26$	$m = 2.92$		
lunette membrane	$a = 5.04 \cdot 10^{-4}$	$d = 0.29$	$g = 3.95 \cdot 10^{-3}$	$m = 2.92$

Table 1. Non-null coefficients of the relation (9) for the surfaces' representation.

expression

$$f_i(x_1, x_2) = a_i x_1^2 x_2^2 + b_i x_1^2 x_2 + c_i x_1 x_2^2 + d_i x_1^2 + e_i x_1 x_2 + g_i x_2^2 + h_i x_1 + l_i x_2 + m_i. \quad (9)$$

The choice of the complete biquadratic function has been made in order to implement in the developed numerical procedure a general Monge form of a quadric surface. The numerical coefficients (Table 1) have been chosen in order to represent the surfaces of the main vault and of the lunette membrane, respectively highlighted in brown and cyan in Figure 5 (left), together with the cylindrical extrados and intrados surfaces.

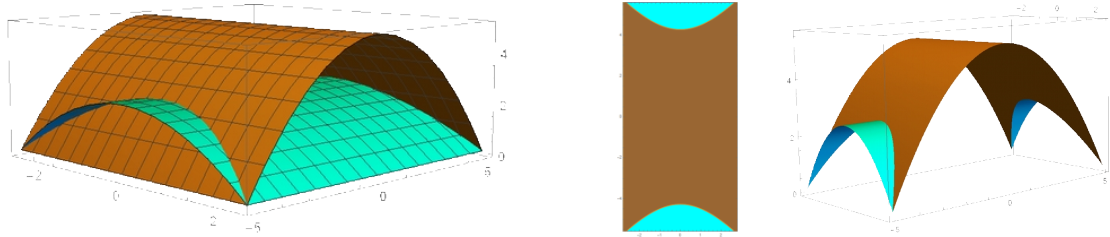


Figure 5. Main vault (brown) and lunette (cyan): surfaces (left), region domains (middle), and combined membrane (right).

The concave stress function $F(x_1, x_2)$ for the uniform vertical pressure $p = 1800 \text{ N} \cdot \text{m}^{-2}$ is given by the solution of the equilibrium equation (5). For the main vault (F^M) and lunette (F^L) vault membrane they are, respectively,

$$\begin{aligned}
 F^M(x_1, x_2) = & -1.84 \cdot 10^6 \log(35.49 - x_1) + 5.19 \cdot 10^4 x_1 \log(35.49 - x_1) - 1.84 \cdot 10^6 \log(35.49 + x_1) \\
 & - 5.19 \cdot 10^4 x_1 \log(35.49 + x_1) - 1.84 \cdot 10^6 \log(5.6 - x_2) + 3.29 \cdot 10^5 x_2 \log(5.6 - x_2) \\
 & - 1.84 \cdot 10^6 \log(5.6 + x_2) - 3.29 \cdot 10^5 x_2 \log(5.6 + x_2),
 \end{aligned} \tag{10}$$

and

$$\begin{aligned}
 F^L(x_1, x_2) = & -4.46 \cdot 10^5 \log(2.80 - x) + 1.59 \cdot 10^5 x \log(2.80 - x) - 4.46 \cdot 10^5 \log(2.80 + x) \\
 & - 1.59 \cdot 10^5 x \log(2.80 + x) - 4.46 \cdot 10^5 \log(24.25 - y) + 1.84 \cdot 10^4 y \log(24.25 - y) \\
 & - 4.46 \cdot 10^5 \log(24.25 + y) - 1.84 \cdot 10^4 y \log(24.25 + y).
 \end{aligned} \tag{11}$$

The two Airy stress functions are definite respectively on the two region domains reported in Figure 5 (middle) whose boundaries on the planform are given by the expressions

$$x_2(x_1) = \pm \frac{29.63 \sqrt{-9569 + 1025x_1^2}}{\sqrt{460208 + 1175x_1^2}}. \tag{12}$$

Considering the rectangular planform, the vertical equilibrium for the combined vaults (9) gives the Pucher stresses obtained by the relation (4). The minimum and maximum Pucher stress maps are reported in Figure 6, while the minimum and maximum physical stresses are reported in Figure 7.

As can be noted, the stress intensity derived from the presented equilibrium solution is very low compared to the possible strength of the masonry, which can be considered ranging between four to six times the calculated values [Faella et al. 2012]. In Figure 7, right, the stress intensity is near the null value, and so the variable distribution is actually due to the numerical approximation of the routine.

A comparison of the obtained equilibrated and admissible stress field with a finite element solution is also reported in order to highlight the effectiveness of the method in describing the vault's behaviour. Analyses based on two-dimensional and three-dimensional finite elements with the linear elastic constitutive model have been performed. The resulting stress maps, with reference to the middle plane of the vault, are reported in Figure 8.

The linear analysis has been considered sufficient to show the reliability of the proposed approach. Note that in order to obtain an equilibrated strain and stress field, the finite element solution needs to

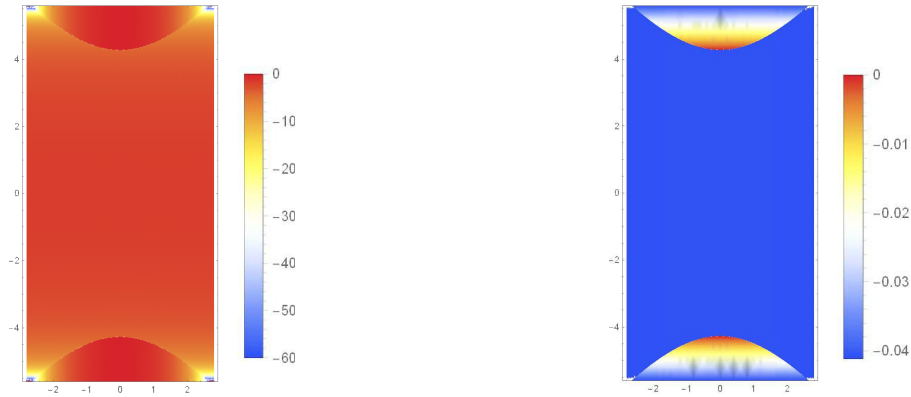


Figure 6. Minimum (left) and maximum (right) Pucher stress maps (values are in $\text{N} \cdot \text{cm}^{-2}$).

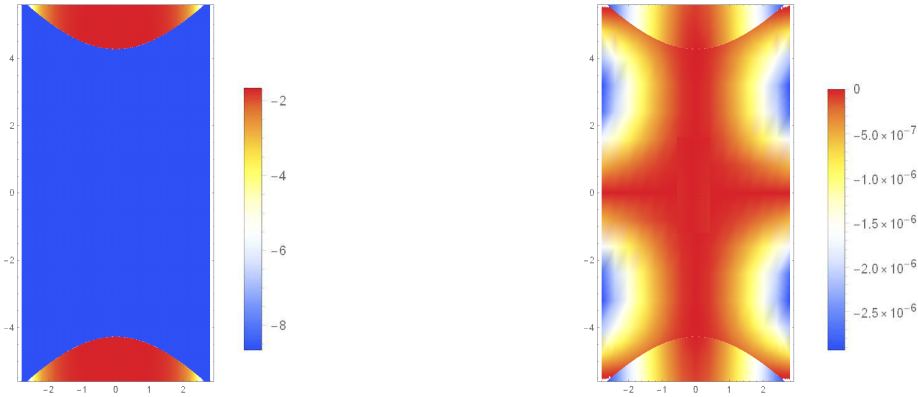


Figure 7. Minimum (left) and maximum (right) physical stress maps (values are in $\text{N} \cdot \text{cm}^{-2}$).

account for the bending stiffness of both the main vault and lunette. Despite the general coherence between the finite element and continuous equilibrium solutions, this is an indirect demonstration of the efficiency and robustness of the proposed method, which is based on the safe theorem of limit analysis.

A very low stress level can be detected in the barrels while the maximum stress concentration has been found at the springing of the vaults and at the intersection of the two vaults (Figure 9).

4. Singular stress fields

The main aspect to be considered in the analysis of combined vaults concerns the singular stress fields arising at the intersection Γ of the two vaults (Figure 10, left), i.e., a line Dirac delta with support on the above defined region boundaries (Figure 10, middle).

In particular, the stress tensor has a singular part along the mentioned intersection of the vaults, whose locally normal vector \mathbf{h} and tangent vector \mathbf{k} are represented in Figure 10 (right), where the domain of the intersection curve on the planfold (dashed red line) is reported together with the intersection curve (continuous line).

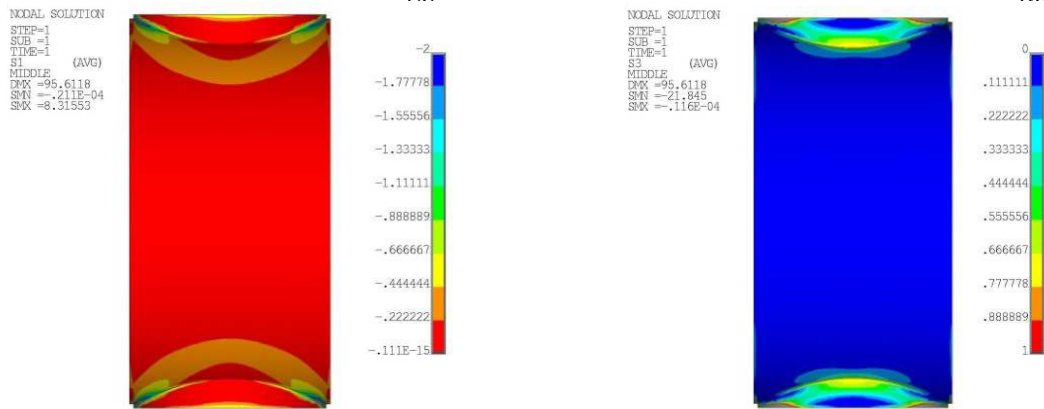


Figure 8. Finite element analysis: minimum (left) and maximum (right) stress maps (values are in $N \cdot mm^{-2}$).

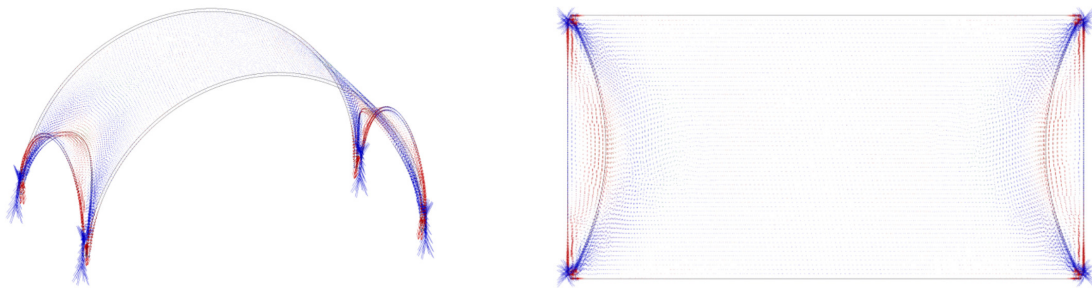


Figure 9. Stress vector maps of the finite element analysis.

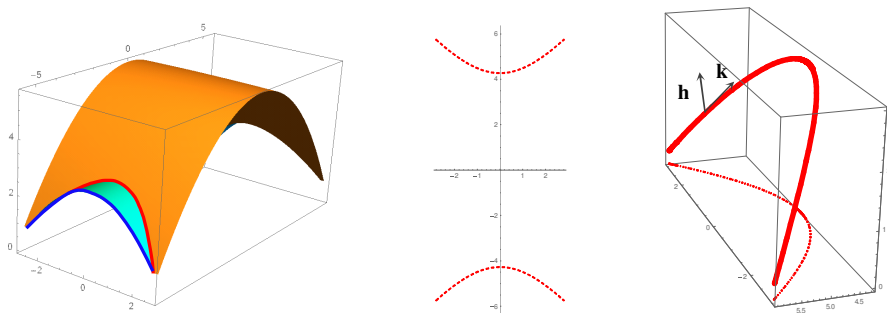


Figure 10. Position of the line Dirac delta at the vaults intersection (left), line plane domain (middle), and plot of the line Γ (right).

As a result, there is an increase in the normal stress along the intersection curve (in red in Figure 10, left and right), compared to the same loading condition in an arch with unitary depth and the same geometry of the lunette, i.e., the directrix curve of the cylindrical vault (in blue in Figure 10).

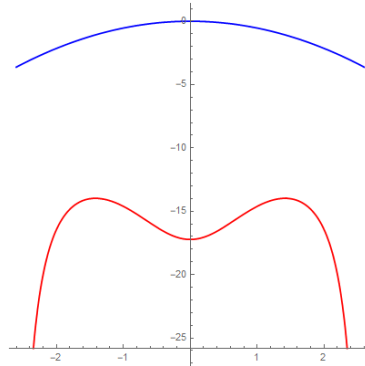


Figure 11. Compressive stress in the intersection curve (red) compared to that in a similar barrel vault (blue).

The compressive stresses in the two cases are shown in Figure 11. Although the ancient builders of combined vaults lacked the appropriate scientific tools to determine this increase, they realized technological details such as the carved stone ribs that counterbalance the stresses maintain the appeal of their constructions.

5. Conclusion

An application of the safe theorem of limit analysis has been presented to model the behaviour of a combined vault system, considered as a continuous material with rigid no-tension constitutive behaviour. The model, based on the definition of a membrane shape function contained in the vault's volume and a stress function formulation, allows the representation of the stress maps relative to an equilibrium solution compatible with the unilateral material assumption. The case study of the barrel vault with lunette in the San Barbaziano church has been examined to show a possible application of the proposed modelling. Special attention has been devoted to the singular stress field arising in the intersection curves for the equilibrium fulfillment. The solutions provided by the proposed method are compared with those obtained by a finite element analysis to assess the efficiency and robustness of the formulation and the ductility of the application in the case of combined vaults, where singular stresses are involved. The proposed procedure allows not only the evaluation of the areas susceptible to damage due to fracture but also the curves where singular stresses are localized, to address the crack pattern of real combined vaulted structures.

Acknowledgements

The contribution of University of Campania “Luigi Vanvitelli” is gratefully acknowledged.

References

- [Angelillo 2015] M. Angelillo, “Static analysis of a Guastavino helical stair as a layered masonry shell”, *Compos. Struct.* **119** (2015), 298–304.
- [Angelillo et al. 2010] M. Angelillo, L. Cardamone, and A. Fortunato, “A numerical model for masonry-like structures”, *J. Mech. Mater. Struct.* **5:4** (2010), 583–615.

- [Angelillo et al. 2013] M. Angelillo, E. Babilio, and A. Fortunato, “Singular stress fields for masonry-like vaults”, *Contin. Mech. Therm.* **25**:2-4 (2013), 423–441.
- [Angelillo et al. 2016] M. Angelillo, E. Babilio, A. Fortunato, M. Lippiello, and A. Montanino, “Analytic solutions for the stress field in static sandpiles”, *Mech. Mater.* **95** (2016), 192–203.
- [Bartoli et al. 2017] G. Bartoli, M. Betti, P. Biagini, A. Borghini, A. Ciavattone, M. Girardi, G. Lancioni, A. M. Marra, B. Ortolani, and B. Pintucchi, “Epistemic uncertainties in structural modelling: a blind benchmark for seismic assessment of slender masonry towers”, *J. Perform. Constr. Fac.* **31**:5 (2017), 04017067.
- [Bergamasco et al. 2017] I. Bergamasco, A. Fortunato, A. Gesualdo, A. Iannuzzo, and M. Monaco, “A no-tension model for the analysis of combined masonry vaults”, pp. 1387–1395 in *AIMETA 2017—XXIII Conference of the Italian Association of Theoretical and Applied Mechanics*, vol. 4, 2017.
- [Bergamasco et al. 2018] I. Bergamasco, A. Gesualdo, A. Iannuzzo, and M. Monaco, “An integrated approach to the conservation of the roofing structures in the Pompeian *Domus*”, *J. Cult. Herit.* **31** (2018), 141–151.
- [Block 2009] P. Block, *Thrust network analysis*, PhD thesis, Massachusetts Institute of Technology, 2009.
- [Block and Lachauer 2014] P. Block and L. Lachauer, “Three-dimensional (3D) equilibrium analysis of gothic masonry vaults”, *Int. J. Archit. Herit.* **8**:3 (2014), 312–335.
- [Buonocore et al. 2014] G. Buonocore, A. Gesualdo, M. Monaco, and M. T. Savino, “Improvement of seismic performance of unreinforced masonry buildings using steel frames”, in *Proceedings of the Twelfth International Conference on Computational Structures Technology*, vol. 117, edited by B. H. V. Topping and P. Iványi, Civil-Comp Press, Stirlingshire, Scotland, 2014.
- [Colla and Pascale 2015] C. Colla and G. Pascale, “Diagnostics and monitoring of the church of San Barbaziano in Bologna”, *Key Eng. Mater.* **624** (2015), 147–154.
- [Como 1992] M. Como, “Equilibrium and collapse of masonry bodies”, *Meccanica* **27**:3 (1992), 185–194.
- [Faella et al. 2012] G. Faella, G. Frunzio, M. Guadagnuolo, A. Donadio, and L. Ferri, “The church of the nativity in Bethlehem: non-destructive tests for the structural knowledge”, *J. Cult. Herit.* **13**:4 (2012), e27–e41.
- [Flügge and Geyling 1957] W. Flügge and F. T. Geyling, “A general theory of deformations of membrane shells”, *IABSE publ.* **17** (1957), 23–46.
- [Fraternali 2010] F. Fraternali, “A thrust network approach to the equilibrium problem of unreinforced masonry vaults via polyhedral stress functions”, *Mech. Res. Commun.* **37**:2 (2010), 198–204.
- [Fraternali 2011] F. Fraternali, “A mixed lumped stress-displacement approach to the elastic problem of masonry walls”, *Mech. Res. Commun.* **38**:3 (2011), 176–180.
- [Fraternali et al. 2014] F. Fraternali, I. Farina, and G. Carpentieri, “A discrete-to-continuum approach to the curvatures of membrane networks and parametric surfaces”, *Mech. Res. Commun.* **56** (2014), 18–25.
- [Gesualdo and Monaco 2010] A. Gesualdo and M. Monaco, “Seismic vulnerability reduction of existing masonry buildings: modelling of retrofitting techniques”, pp. 853–858 in *Urban Habitat Constructions under Catastrophic Events—Proceedings of the COST C26 Action Final Conference*, edited by F. M. Mazzolani, 2010.
- [Gesualdo et al. 2010] A. Gesualdo, M. Monaco, and M. T. Savino, “Seismic retrofitting techniques for masonry arch bridges”, pp. 859–864 in *Urban Habitat Constructions under Catastrophic Events—Proceedings of the COST C26 Action Final Conference*, edited by F. M. Mazzolani, 2010.
- [Gesualdo et al. 2017] A. Gesualdo, C. Cennamo, A. Fortunato, G. Frunzio, M. Monaco, and M. Angelillo, “Equilibrium formulation of masonry helical stairs”, *Meccanica* **52**:8 (2017), 1963–1974.
- [Hendry 1995] A. W. Hendry, “Masonry arch design at the end of the 19th century”, pp. 140–144 in *Proc. 4th Int. Masonry Symp.*, edited by H. W. H. West, Proceedings of the British Masonry Society **7**, 1995.
- [Heyman 1966] J. Heyman, “The stone skeleton”, *Int. J. Solids Struct.* **2**:2 (1966), 249–256.
- [Heyman 1970] J. Heyman, “The collapse of stone vaulting”, *WIT Trans. Built Environ.* **4** (1970), 12 pp.
- [Heyman 1977] J. Heyman, *Equilibrium of shell structures*, Clarendon Press, Oxford, 1977.
- [Heyman 1982] J. Heyman, *The masonry arch*, Ellis Horwood Limited, Chichester, England, 1982.
- [Hooke 1676] R. Hooke, *A description of helioscopes, and some other instruments*, 1676.

- [Huerta 2001] F. S. Huerta, “Mechanics of masonry vaults: the equilibrium approach”, pp. 47–69 in *Proceedings of 3rd International Seminar on Historical Constructions* (Guimarães, 2001), edited by P. B. Lourenço and P. Roca, 2001.
- [Huerta 2008] S. Huerta, “The analysis of masonry architecture: a historical approach”, *Architect. Sci. Rev.* **51**:4 (2008), 297–328.
- [Iannuzzo et al. 2018] A. Iannuzzo, M. Angelillo, E. De Chiara, F. De Guglielmo, F. De Serio, F. Ribera, and A. Gesualdo, “Modelling the cracks produced by settlements in masonry structures”, *Meccanica* **53**:7 (2018), 1857–1873.
- [Kurrer 2008] K.-E. Kurrer, *The history of the theory of structures: from arch analysis to computational mechanics*, Ernst & Sohn, Berlin, 2008.
- [Lucchesi et al. 2007] M. Lucchesi, C. Padovani, G. Pasquinelli, and N. Zani, “Static analysis of masonry vaults, constitutive model and numerical analysis”, *J. Mech. Mater. Struct.* **2**:2 (2007), 221–244.
- [Lucchesi et al. 2008] M. Lucchesi, M. Šilhavý, and N. Zani, “Integration of measures and admissible stress fields for masonry bodies”, *J. Mech. Mater. Struct.* **3**:4 (2008), 675–696.
- [Lucchesi et al. 2012] M. Lucchesi, M. Šilhavý, and N. Zani, “On the choice of functions spaces in the limit analysis for masonry bodies”, *J. Mech. Mater. Struct.* **7**:8-9 (2012), 795–836.
- [Marmo and Rosati 2017] F. Marmo and L. Rosati, “Reformulation and extension of the thrust network analysis”, *Comput. Struct.* **182** (2017), 104–118.
- [Marmo et al. 2018] F. Marmo, D. Masi, and L. Rosati, “Thrust network analysis of masonry helical staircases”, *Int. J. Archit. Herit.* **12**:5 (2018), 828–848.
- [Moseley 1833] H. Moseley, “On the equilibrium of the arch”, *Cambridge Philos. Trans.* **5** (1833), 293–313.
- [Moseley 1860] H. Moseley, *The mechanical principles of engineering and architecture*, Wiley, New York, 1860.
- [O’Dwyer 1999] D. O’Dwyer, “Funicular analysis of masonry vaults”, *Comput. Struct.* **73**:1-5 (1999), 187–197.
- [Pucher 1934] A. Pucher, “Über der Spannungszustand in gekrümmten Flächen”, *Beton u. Eisen* **33** (1934), 298–304.
- [Pucher 1937] A. Pucher, “Die Berechnung von doppelt gekrümmten Schalen mittels Differenzgleichungen”, *Der Bauingenieur* **18**:9-10 (1937), 118–123.
- [Sacco et al. 2018] E. Sacco, D. Addessi, and K. Sab, “New trends in mechanics of masonry”, *Meccanica* **53**:7 (2018), 1565–1569.

Received 12 Nov 2018. Revised 24 Jan 2019. Accepted 2 Mar 2019.

MICHELA MONACO: michela.monaco@unicampania.it

Department of Architecture and Industrial Design (DADI), University of Campania “Luigi Vanvitelli”, Aversa, Italy

IMMACOLATA BERGAMASCO: immacolata.bergamasco@beniculturali.it

Archaeological Park of Pompeii, Ministry for Cultural Heritage and Activities and Tourism, Pompeii, Italy

MICHELE BETTI: michele.betti@unifi.it

Department of Civil and Environmental Engineering, University of Florence, Florence, Italy

SUBMISSION GUIDELINES

ORIGINALITY

Authors may submit manuscripts in PDF format online at the Submissions page. Submission of a manuscript acknowledges that the manuscript is original and has neither previously, nor simultaneously, in whole or in part, been submitted elsewhere. Information regarding the preparation of manuscripts is provided below. Correspondence by email is requested for convenience and speed. For further information, write to contact@msp.org.

LANGUAGE

Manuscripts must be in English. A brief abstract of about 150 words or less must be included. The abstract should be self-contained and not make any reference to the bibliography. Also required are keywords and subject classification for the article, and, for each author, postal address, affiliation (if appropriate), and email address if available. A home-page URL is optional.

FORMAT

Authors can use their preferred manuscript-preparation software, including for example Microsoft Word or any variant of $\text{T}_{\text{E}}\text{X}$. The journal itself is produced in $\text{L}^{\text{A}}\text{T}_{\text{E}}\text{X}$, so accepted articles prepared using other software will be converted to $\text{L}^{\text{A}}\text{T}_{\text{E}}\text{X}$ at production time. Authors wishing to prepare their document in $\text{L}^{\text{A}}\text{T}_{\text{E}}\text{X}$ can follow the example file at www.jomms.net (but the use of other class files is acceptable). At submission time only a PDF file is required. After acceptance, authors must submit all source material (see especially Figures below).

REFERENCES

Bibliographical references should be complete, including article titles and page ranges. All references in the bibliography should be cited in the text. The use of $\text{BibT}_{\text{E}}\text{X}$ is preferred but not required. Tags will be converted to the house format (see a current issue for examples); however, for submission you may use the format of your choice. Links will be provided to all literature with known web locations; authors can supply their own links in addition to those provided by the editorial process.

FIGURES

Figures must be of publication quality. After acceptance, you will need to submit the original source files in vector format for all diagrams and graphs in your manuscript: vector EPS or vector PDF files are the most useful. (EPS stands for Encapsulated PostScript.)

Most drawing and graphing packages—Mathematica, Adobe Illustrator, Corel Draw, MATLAB, etc.—allow the user to save files in one of these formats. Make sure that what you're saving is vector graphics and not a bitmap. If you need help, please write to graphics@msp.org with as many details as you can about how your graphics were generated.

Please also include the original data for any plots. This is particularly important if you are unable to save Excel-generated plots in vector format. Saving them as bitmaps is not useful; please send the Excel (.xls) spreadsheets instead. Bundle your figure files into a single archive (using zip, tar, rar or other format of your choice) and upload on the link you been given at acceptance time.

Each figure should be captioned and numbered so that it can float. Small figures occupying no more than three lines of vertical space can be kept in the text (“the curve looks like this:”). It is acceptable to submit a manuscript with all figures at the end, if their placement is specified in the text by means of comments such as “Place Figure 1 here”. The same considerations apply to tables.

WHITE SPACE

Forced line breaks or page breaks should not be inserted in the document. There is no point in your trying to optimize line and page breaks in the original manuscript. The manuscript will be reformatted to use the journal's preferred fonts and layout.

PROOFS

Page proofs will be made available to authors (or to the designated corresponding author) at a Web site in PDF format. Failure to acknowledge the receipt of proofs or to return corrections within the requested deadline may cause publication to be postponed.

**Special issue on
Structural Analysis
of Real Historic Buildings (part 1)**

Preface	MAURIZIO ANGELILLO and SANTIAGO HUERTA FERNÁNDEZ	607
The structural engineer's view of ancient buildings	JACQUES HEYMAN	609
Mechanics of flying buttresses: the case of the cathedral of Mallorca	PAULA FUENTES	617
Analysis of 3D no-tension masonry-like walls	DEBORAH BRICCOLA, MATTEO BRUGGI and ALBERTO TALIERCIO	631
Cracking of masonry arches with great deformations: a new equilibrium approach	JOSÉ IGNACIO HERNANDO GARCÍA, FERNANDO MAGDALENA LAYOS and ANTONIO AZNAR LÓPEZ	647
Resistance of flat vaults taking their stereotomy into account	MATHIAS FANTIN, THIERRY CIBLAC and MAURIZIO BROCATO	657
Seismic vulnerability of domes: a case study	CONCETTA CUSANO, CLAUDIA CENNAMO and MAURIZIO ANGELILLO	679
Orthotropic plane bodies with bounded tensile and compressive strength	MASSIMILIANO LUCCHESI, BARBARA PINTUCCHI and NICOLA ZANI	691
A no-tension analysis for a brick masonry vault with lunette	MICHELA MONACO, IMMACOLATA BERGAMASCO and MICHELE BETTI	703

